AC Measurements of Graphene-Superconductor Devices

by

Trevyn Larson

Department of Physics
Duke University

Date: ____________________

Approved:

____
Gleb Finkelstein, Supervisor

____
Harold Baranger

____
Shailesh Chandrasekharan

____
Sarah Haravifard

____
Stephen Teitsworth

Dissertation submitted in partial fulfillment of the requirements for the degree of
Doctor of Philosophy in the Department of Physics
in the Graduate School of Duke University
2022

Abstract

AC Measurements of Graphene-Superconductor Devices

by

Trevyn Larson

Department of Physics
Duke University

Date: ____________________

Approved:

____
Gleb Finkelstein, Supervisor

____
Harold Baranger

____
Shailesh Chandrasekharan

____
Sarah Haravifard

____
Stephen Teitsworth

An abstract of a dissertation submitted in partial fulfillment of the requirements for
the degree of Doctor of Philosophy in the Department of Physics
in the Graduate School of Duke University
2022

Abstract

The field of quantum transport studies electron motion at low temperatures in nanostructures. Exciting electron phenomenon can be engineered by combining device designs like quantum dots, Josephson junctions, and interferometers with materials which host physics such as various quantum Hall effects and superconductivity. Combinations of these ingredients can be mixed to design a device which is then cooled down and has its $I-V$ curves measured while tuning key physical parameters, such as magnetic field, temperature, and gate electrode voltages.

These time independent (DC) measurements can provide a wealth of information, but ultimately they can only access highly averaged physical properties. Fortunately, this is not a fundamental constraint. By measuring the emission of and response to higher frequency signals, we are able to access additional properties of our devices.

This dissertation explores two projects related to time oscillating (AC) measurements of graphene devices with superconducting contacts. The first project is related to the measurement of "Shapiro steps" in graphene based Josephson junctions. By applying a gigahertz drive to the junction, it becomes possible to probe the dynamics of the phase difference of the junction. The work presented here explores the effects of the RF environment on the Shapiro step pattern, and on a bistability observed in this system.

The second project addresses the noise measured downstream of a superconducting contact for a device in the quantum Hall regime. Recent work has observed the coupling of superconductivity to a quantum Hall edge, a promising test-bed for mixing superconductivity with topological physics. However, the signal in real devices remains fairly small compared to the ideal limit. Noise measurements should allow us to probe the microscopics in these devices, but we find indications that signals seemingly related to contact heating obscure the desired signal. Additional devices which should show a tunable signal amplitude show only very small signal variation, opening questions about what physical phenomena may be suppressing this noise.

For Denise and Elizabeth

Contents

List of Figures

List of Abbreviations and Symbols

Abbreviations

BdG – Bogoliubov-de-Gennes

SIS – Superconductor Insulator Superconductor

SNS – Superconductor Normal Superconductor

BCS – Bardeen-Cooper-Schrieffer

ABS – Andreev Bound State

IV – Current Voltage

CPR – Current Phase Relationship

RCSJ – Resistively and Capacitively Shunted Junction

DC – Direct Current

AC – Alternating Current

RF – Radio Frequency

MoRe – Molybdenum Rhenium

SiO2 – Silicon Oxide

hBN – hexagonal Boron Nitride

MQT – Macroscopic Quantum Tunneling

2DEG – 2 Dimensional Electron Gas

HEMT – High Electron Mobility Transistor

BJT – Bipolar Junction Transistor

FFT – Fast Fourier Transform

CAES – Chiral Andreev Edge State

SC – Superconducting

QPC – Quantum Point Contact

Acknowledgements

I am extremely grateful to the many people who helped me throughout this PhD.

My advisor Gleb Finkelstein made the work presented here possible. Gleb is consistently insightful and open minded about a wide range of scientific projects, and has an incredible ability to mix physics insights with detail oriented, well designed experiments.

A number of other people at Duke were also instrumental in my journey. Yuriy Bomze has consistently listened to me describe experimental frustrations and provided insightful, clear cut suggestions. Stephen Teitsworth has an infectious range of scientific interests and was a wonderful mentor both early in my career, and when Shapiro steps brought me back to non-linear dynamics. Harold Baranger has an exceptional gift for distilling sophisticated mesosopic theory into a form fit for experimentalists.

When I first joined Gleb's group, I benefited immensely from Chung-Ting Ke's mentorship, and was awed by watching one student capable of doing every experimental task that got in his way. After Ting graduated, I got to learn a great deal about coding for instrumentation and cryogenic hardware from Anne Draelos and Ming-Tso Wei.

Getting to join Gleb's group at the same time as Ethan Arnault and Lingfei Zhao was very fortunate. Ethan has consistently provided cryogenic expertise and physics discussions over the course of our friendship. Lingfei has forced me to discard many

of my erroneous ideas of physics over the years, and also has provided exceptional device fabrication insight. Andrew Seredinski's pedagogical skills, writing prowess and love of the google doodle ghost game were all equally instrumental. For the last year of my PhD, I have really enjoyed Zubair Iftikhar's love of all things noise and microwaves, and his focused approach to science.

Outside of the lab, Ryan Kozlowski, Dripto Debroy, George Schwartz, Kamali Jones, Devin Wiley and Emma Arnault have been a wonderful group of friends, both through normal graduate school times and through the pandemic Zoom game night period.

Laslty, I am very thankful to my mother, Denise, my stepbrother, Richard, and the rest of my family, as well as Elizabeth and her family, for providing the critical support throughout my PhD.

1

Introduction

The last two decades have seen remarkable advancements in condensed matter physics. Theorists have proposed many new, exciting systems, particularly in terms of topological behavior [1]. Experimentally, many of these systems have been realized, showing results consistent with theory [2, 3], while other systems are showing promising preliminary results [4].

A large number of these studies are performed via electrical transport measurements. In such studies, a sample has electrical contacts deposited so that one can measure I-V curves as a function of various parameters such as gate voltages, applied magnetic fields and sample temperature. This is a versatile and powerful technique but ultimately only provides access to averaged properties. Interpreting such measurements is often also very challenging, given that condensed matter systems do not allow one to know their Hamiltonian exactly.

Studying these materials with higher frequency techniques allows for direct observation of properties that are otherwise challenging to study or unobservable. Examples include thermal conductivity [5], the charge of emergent quasiparticles [6, 7], and fractional statistics [8]. There are a number of engineering challenges associated with radio and higher frequency measurement techniques in a cryogenic environment. Typical transport measurements utilize lossy microcoaxes which effectively filter the lines from high frequency noise, while also being resistive and therefore having low heat conductivity according to the Wiedemann-Franz law. In contrast, high frequency lines must be very conductive and RF matched, but carefully designed to not be too thermally conductive so as to not couple cryostat stages of different temperatures. Lines used for absorption spectroscopy must be carefully attenuated so as to prevent high frequency noise from outside of the dilution refrigerator from coupling to the system while still allowing the desired signal to reach the sample. Emission lines must be carefully designed to avoid back action on the sample and typically include a large heat load cryogenic amplifier which must be thermally decoupled from the sample. Despite these challenges, high frequency techniques are beginning to show exceptional probing and manipluation of condensed matter systems [9].

This PhD is primarily focused on probing graphene superconducting devices with non-DC techniques. The first portion addresses RF driven graphene Josephson junctions. Such RF drive can give rise to "phase locking" and quantized DC voltage steps in the IV curve of a junction. This technique also allows one to probe the current phase relationship of a device and thus the material properties of the weak link. While graphene should generally have a relatively standard CPR, work described in Chapter 3 shows that the electromagnetic environment can effect the observed pattern of quantized voltage steps in significant ways, which can obscure the ability to measure the desired physics. We also find that the system forms a very tunable bistable system, with rich switching behavior that is not described by standard activation effects. Experiments utilizing this bistability are addressed in Chapter 4.

The second part of this text addresses measurements of the intrinsic noise of a quantum Hall superconducting contact. Measurements of the voltage fluctuations in a mesoscopic sample can tell us a great deal of information about the way in which heat and charge are flowing. However, given the significant impedance of the conductance quantum, few channel samples typically have their fluctuations filtered before they can be measured outside of the cryostat. To escape this issue, we follow a common path and use a homemade cryogenic HEMT amplifier with a tank circuit resonator to measure this noise. The construction and calibration of this setup are detailed in Chapter 6.

Finally, we address the noise that is measured downstream of a superconducting contact in the quantum Hall regime in Chapter 7. Recent work from our group has shown that this system can exhibit chiral Andreev edge states, where by Andreev reflections cause an incoming electron to be converted to hybridized electron-hole states [10]. Building on this result, another group has found that there is a significant noise signal can be measured at a superconductor - quantum Hall interface which was attributed to shot noise[11]. However, we find that similar noise can be observed downstream of a normal metal contact, indicating that for short contacts to a graphene device at low field it is possible that the edge state is not totally thermalized. Further, when we measure the noise as a function of gate voltage on a given plateau, we observe minimal variation of the noise signal, which is in stark contrast to the non-local resistance which is significantly oscillating. This seems to indicate that there must be certain equilibration processes at play leading to the suppression of the shot noise.

2

Theory I: Superconductivity and Josephson Effects

2.1 Superconductivity

Shortly after liquifying helium, Kamerlingh Onnes first discovered superconductivity in mercury, observing a sudden drop in resistance as a function of temperature. This was followed by similar observations in tin and lead, as well as observations of perfect diamagnetism.

It would ultimately take more than 40 years to develop an understanding of the microscopics of the most basic superconducting materials. During this time, several phenomenological models were developed, such as the London equations and Ginzberg-Landau theory. The details of the failed microscopic models proposed during the time are quite interesting[12]. Both Bloch and Landau proposed theories in which the ground state was a finite momentum state[13, 14], although Bloch later developed a theorem showing that ground states in electronic systems are by necessity zero net momentum states[15] (although finite momentum superconductivity has recently reemerged in more nuanced contexts, for example [16]). Kronig developed a theory where coulomb repulsion of an electron gas is very large compared to the kinetic energy, and current was then carried by the sliding of the electron solid. This theory predated Wigner's work on electron crystallization by two years[17].

Ultimately, Bardeen, Cooper and Shrieffer developed the BCS theory of superconductivity. This work began with what is now known as the Cooper problem[11], where it was shown that electron phonon interaction could lead the formation of a bound state between two electrons.In BCS theory, it was shown that below a critical temperature, electrons within a certain range of the Fermi surface readily form such pairs, giving rise to a superconducting gap in the density of states Δ within which there are no single particle states.

While many of these properties can be lengthy to derive, we note several properties of superconductivity that are worth understanding phenomenologically [18]

- Superconducting materials are predicted to be truly dissipationless. While many precise measurements have placed a minimal upper bound on the actual resistance of a superconductor, there can be complications in real systems, such as finite dissipation above H_{C1} in a type II superconductor (see below).

- In additional to a critical temperature, superconductors also have a critical current density and critical magnetic field, above which they transition back to a normal state.

- Superconductors are categorized based off of the ratio of two length scales. The first is the London penetration depth λ_L which is the distance over which the superconductor screens magnetic fields. The second is the Ginzberg-Landau coherence length ξ. In Ginzberg-Landau theory, a macroscopic superconductor can be described locally by a complex order parameter field. The correlation function of this complex order parameter at two different points depends exponentially on the distance between the points, with length ξ being the characteristic length. The ratio of these two values $\kappa = \frac{\lambda_L}{\xi}$ is known as the Ginzberg-Landau parameter.

We can naturally consider two limits of behavior here. The first is if λ_L is the relatively small length (or more strictly $\kappa < \frac{1}{\sqrt{2}}$). In this situation, if we take such a superconductor and begin applying magnetic field, it is energetically favorable for the superconductor to expel the field and keep the order parameter smooth, up to thermodynamic considerations potentially leading to macroscopic normal regions [18]. Ignoring such details, the superconductor will expel magnetic field until the field exceeds H_C, at which point the entire superconductor transitions to the normal state. Superconductors of this type are known as type-I, and it includes most simple elemental superconductors.

In the opposite limit, it can be energetically favorable for the superconductor to form miscroscopic normal regions and have the order parameter wind around such regions. More concretely, above a certain magnetic field H_{C1} the superconductor will allow tubes of magnetic field to flow through it. These tube regions are known as vorticies[19], and play an important role in the experiment in Chapter 7. Superconductors of this type are known as type-II. Eventually, the magnetic field will exceed a value H_{C2} such that the entire superconductor transitions to the normal state.

2.2 Bogoliubov-de-Gennes

While Ginzberg-Landau theory is typically sufficient to understand a great deal about Josephson junctions and superconducting device physics, in work on mesoscopic physics we often need more significant theoretical tools. In particular, we would like to understand the excitation spectrum, and we would like to be able to understand the effects of an external potential in our system.

We begin by writing our electron systems in terms of real space electron creation and annihilation operators, which are related to the standard second quantized operators by

$$\begin{aligned}\Psi(r,\alpha) &= \sum_k e^{ik\cdot r} a_{k\alpha} \\ \Psi^\dagger(r,\alpha) &= \sum_k e^{-ik\cdot r} a^\dagger_{k\alpha}\end{aligned} \tag{2.1}$$

with α denoting a spin index

We can easily write a generic Hamiltonian in terms of these parameters, with just a kinetic energy and a pointlike interaction of electrons (we know that the BCS interaction can be written in this form because the BCS interaction is of constant strength, so upon Fourier transforming it becomes a δ function)

$$\mathcal{H}_{kin} = \sum_\alpha \int d^3r \Psi^\dagger(\mathbf{r},\alpha)\hat{H}_e\Psi(\mathbf{r},\alpha) \tag{2.2}$$

$$\mathcal{H}_{\text{int}} = -\frac{V}{2}\sum_{\alpha,\beta}\int d^3r \Psi^\dagger(\mathbf{r},\alpha)\Psi^\dagger(\mathbf{r},\beta)\Psi(\mathbf{r},\beta)\Psi(\mathbf{r},\alpha) \tag{2.3}$$

As usual, terms which are fourth order in electron operators are quite complicated. The most straightforward thing we can do is to perform a mean field approximation and rediagonalize our new effective Hamiltonian. Applying Wick's theorem to our fourth order term and considering that our BCS attractive interaction pairs opposite spins we find[20][21]

$$\begin{aligned}\mathcal{H}_{eff} = &\int d^3r \sum_\alpha \left[\Psi^\dagger(\mathbf{r},\alpha)\hat{H}_e\Psi(\mathbf{r},\alpha) + U(\mathbf{r})\Psi^\dagger(\mathbf{r},\alpha)\Psi(\mathbf{r},\alpha)\right] \\ &+ \int d^3r \left[\Delta(\mathbf{r})\Psi^\dagger(\mathbf{r},\uparrow)\Psi^\dagger(\mathbf{r},\downarrow) + \Delta^*(\mathbf{r})\Psi(\mathbf{r},\downarrow)\Psi(\mathbf{r},\uparrow) + H_0(\mathbf{r})\right]\end{aligned} \tag{2.4}$$

which when diagonalized takes the form

$$\mathcal{H}_{eff} = E_g + \sum_{n,\alpha} \epsilon_n \gamma^\dagger_{n,\alpha} \gamma_{n,\alpha}, \tag{2.5}$$

It is worth noting that different specifics of the superconductor and the attractive interaction may modify H_{eff}, but the general procedure presented will be valid (for example, see [22]).

Following diagonalization, our new operators γ and our electron operators are related by a unitary transformation

$$\begin{aligned} \Psi^\dagger(\mathbf{r} \uparrow) &= \sum_n \left[\gamma^\dagger_{n\uparrow} u^*_n(\mathbf{r}) - \gamma_{n\downarrow} v_n(\mathbf{r})\right] \\ \Psi^\dagger(\mathbf{r} \downarrow) &= \sum_n \left[\gamma^\dagger_{n\downarrow} u^*_n(\mathbf{r}) + \gamma_{n\uparrow} v_n(\mathbf{r})\right] \end{aligned} \tag{2.6}$$

where the opposite spin pairing in the unitary transformation follows from the opposite spin pairing in the effective Hamiltonian. The corresponding annihilation operators can be easily identified by taking the Hermitian conjugate. We would like to solve for u_n, v_n in order to understand the quasiparticles in our system. We can do this by considering the commutators of H_{eff} with the two sets of operators

$$\begin{aligned} [\mathcal{H}_{eff}, \Psi(\mathbf{r},\uparrow)]_- &= -\left[\hat{H}_e + U(\mathbf{r})\right] \Psi(\mathbf{r},\uparrow) - \Delta(\mathbf{r})\Psi^\dagger(\mathbf{r},\downarrow) \\ [\mathcal{H}_{eff}, \Psi(\mathbf{r},\downarrow)]_- &= -\left[\hat{H}_e + U(\mathbf{r})\right] \Psi(\mathbf{r},\downarrow) + \Delta(\mathbf{r})\Psi^\dagger(\mathbf{r},\uparrow) \end{aligned} \tag{2.7}$$

$$\begin{aligned} [\mathcal{H}_{eff}, \gamma_{n,\alpha}]_- &= -\epsilon_n \gamma_{n,\alpha} \\ \left[\mathcal{H}_{eff}, \gamma^\dagger_{n,\alpha}\right]_- &= \epsilon_n \gamma^\dagger_{n,\alpha} \end{aligned} \tag{2.8}$$

Expressing our electron position operators in terms of the diagonal operators we find

$$\begin{aligned} \left[\hat{H}_e + U(\mathbf{r})\right] u(\mathbf{r}) + \Delta(\mathbf{r}) v(\mathbf{r}) &= \epsilon u(\mathbf{r}) \\ -\left[\hat{H}_e^* + U(\mathbf{r})\right] v(\mathbf{r}) + \Delta^*(\mathbf{r}) u(\mathbf{r}) &= \epsilon v(\mathbf{r}) \end{aligned} \tag{2.9}$$

which can naturally be expressed as a matrix equation in an electron hole basis

$$\begin{bmatrix} \hat{H}_e + U & \Delta \\ \Delta^* & -\left[\hat{H}_e^* + U\right] \end{bmatrix} \begin{bmatrix} u_n \\ v_n \end{bmatrix} = \epsilon_n \begin{bmatrix} u_n \\ v_n \end{bmatrix} \tag{2.10}$$

This now allows us to solve for the elementary excitations in the presence of arbitrary U. It is also a very helpful formulation for considering proximity coupling, which is addressed in the next section. Lastly, we note that this formulation is particle hole symmetric – for $\begin{bmatrix} u_n \\ v_n \end{bmatrix}$ with energy ϵ_n, $\begin{bmatrix} v_n^* \\ u_n^* \end{bmatrix}$ is a valid solution with energy -ϵ_n. This symmetry is a key ingredient which is often utilized in proposals for Majorana fermions[23], although there exists interesting work on the ways in which the subtlties of BDG may effect these results[24].

2.3 From SIS to SNS

Shortly after the development of BCS theory and the understanding of the microscopic mechanisms at play in superconductors, Brian Josephson realized that if two separate superconductors are connected by an insulating layer (as is shown in Figure 2.1) remarkable effects can be observed. A fairly informal derivation can be considered as follows[21][25]: we begin with a superconducting lead which we associate with a single complex order parameter ψ. This is a consequence of Ginzberg-Landau theory with a long coherence length, and this "macroscopic quantum coherence" is the fundamental element of our circuit.

By itself the lead obeys $i\hbar\frac{d\psi}{dt} = E\psi$. Now we consider two such leads, with a very thin insulator in between. While initially the leads are decoupled, the thin insulator

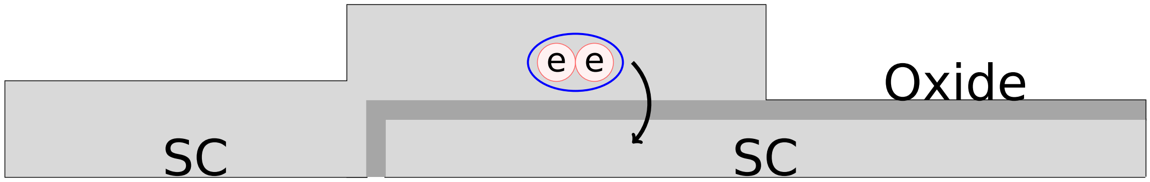

FIGURE 2.1: A side profile of a standard SIS junction. A very thin (≈5 nm) oxide layer allows for Cooper pairs to tunnel directly across the junction.

allows some tunneling of Cooper pairs between the two leads. We can suppose that this coupling is simply proportional to the order parameter in the other lead. To be slightly more specific, we can refer to the coupling parameter between the two leads as K. This is connected to the properties of the tunnel barrier. We will take the energy of the lead to be $\pm qV$ for some voltage difference 2V. This leads to the matrix equation

$$\begin{bmatrix} qV & K \\ K & -qV \end{bmatrix} \begin{bmatrix} \psi_1 \\ \psi_2 \end{bmatrix} = i\hbar \begin{bmatrix} \frac{d\psi_1}{dt} \\ \frac{d\psi_2}{dt} \end{bmatrix} \tag{2.11}$$

We can now rewrite ψ as $\psi = \sqrt{N}e^{i\chi}$ which gives the differential equations

$$\begin{aligned} h\frac{dN_1}{dt} &= -2K\sqrt{N_1N_2}\sin\left(\chi_2 - \chi_1\right) \\ h\frac{dN_2}{dt} &= 2K\sqrt{N_1N_2}\sin\left(\chi_2 - \chi_1\right) \end{aligned} \tag{2.12}$$

and

$$\begin{aligned} \hbar N_2\frac{d\chi_2}{dt} &= eVN_2 + K\sqrt{N_1N_2}\cos\left(\chi_2 - \chi_1\right) \\ \hbar N_1\frac{d\chi_1}{dt} &= -eVN_1 + K\sqrt{N_1N_2}\cos\left(\chi_2 - \chi_1\right) \end{aligned} \tag{2.13}$$

The first two equations give us the DC Josephson relation

$$I = I_c \sin\phi \tag{2.14}$$

as the current which can flow through the junction in the absence of a voltage. Here ϕ is the relative phase difference between the leads and I_C is a constant parameter of the device. The second set of equations give the AC Josephson effect

$$\hbar \frac{\partial \phi}{\partial t} = 2eV \tag{2.15}$$

which relates the instantaneous voltage across the junction to the derivative of the phase difference with respect to time.

Josephson junctions have become a remarkable tool in technology, from the voltage standard[26], to sensing[27], to circuit quantum electrodynamics and quantum computing[28]. Microscopically, these Josephson junctions with an insulating link are believed to still follow the above reasonably simple picture. However, it is also possible to engineer Josephson junctions with other types of weak links. One such weak link considered throughout this dissertation is the semiconducting or normal metal weak link. These junctions are typically referred to as SNS for superconducting-normal metal - superconducting, in contrast to the SIS superconducting-insulating-superconductor junctions. These devices host much richer microscopic physics. To emphasize how different these two devices are, note that standard laboratory SIS junctions can only mediate a supercurrent through an insulating layer of 5 nm. At longer length scales the tunneling probability simply becomes too low. However, SNS junctions can easily mediate a supercurrent over distances of microns. This is a strong indication that the supercurrent is not mediated by the tunneling of Cooper pairs, so how does it arise?

To answer this question, we must first take a step back and answer an even simpler question regarding what physically happens at a superconductor normal metal interface. Naturally the metal or semiconductor transports charge by electrons or holes, while the superconductor does so by Cooper pairs, but it is not immediately clear how these carriers are microscopically converted into one another.

We will consider a simple superconductor normal metal interface illustrated schematically in Figure 2.2. We begin with the BDG equations, and make a semiclassical

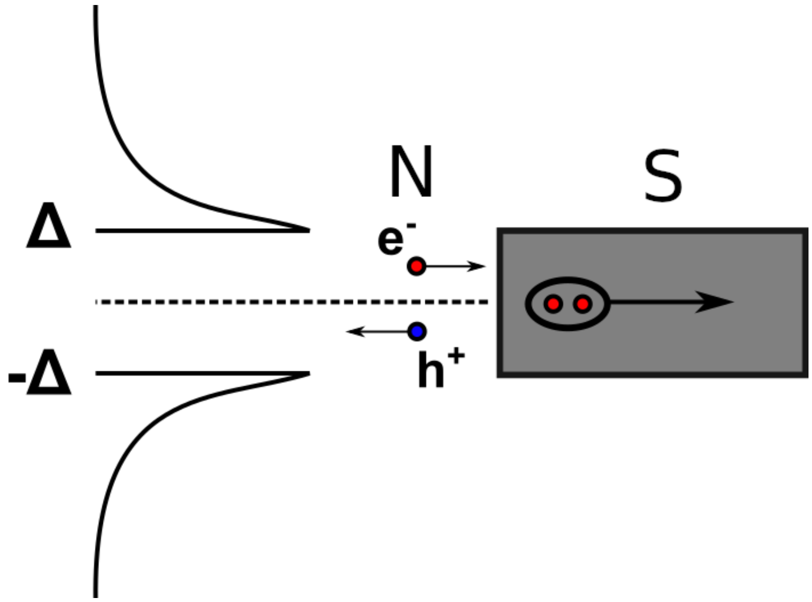

FIGURE 2.2: A schematic of Andreev reflection. On the left we see the density of states of the superconductor. When an electron with an energy within the gap is incident on the superconducting interface, it is completely transmitted and a hole is formed so that a Cooper pair can be formed within the superconductor.

approximation

$$\begin{pmatrix} u \\ v \end{pmatrix} = e^{i\mathbf{k}\cdot\mathbf{r}} \begin{pmatrix} U(x) \\ V(x) \end{pmatrix} \tag{2.16}$$

where $|\mathbf{k}| = k_F$. $U(x)$ and $V(x)$ are smoothly varying functions on the length scale $1/|\mathbf{k}|$ (note that these are unrelated to the potential energy $U(x)$ discussed earlier). This can be plugged into the BDG equations. We can assume second order derivatives of $U(x), V(x)$ are small and neglect them. If we also assume a system without magnetic field than we find

$$\begin{array}{l} -i\hbar v_x \frac{dU}{dx} + \Delta V = \epsilon U \\ i\hbar v_x \frac{dV}{dx} + \Delta^* U = \epsilon V \end{array} \tag{2.17}$$

where v_x is the component of velocity in the x direction for a given Fermi surface wave vector. Generically inside the superconductor our solution will be of the form

$$\begin{pmatrix} U(x) \\ V(x) \end{pmatrix}_R = ce^{i\lambda_S x} \begin{pmatrix} U_0 \\ V_0 \end{pmatrix} \tag{2.18}$$

with $\lambda_S = \frac{\sqrt{\epsilon^2 - |\Delta|^2}}{\hbar v_x}$. Inside the normal region we can solve these same equations while setting $\Delta = 0$. We are particularly interested in what happens when an electron is incident on the superconducting region, but it is immediately clear that the only way to match the wavefunctions at the interface and match currents is to have a retroreflected hole.

The fact that an electron gets retroreflected as a hole and a Cooper pair is formed in the superconducting lead is the primary result we are looking for. This process is known as Andreev reflection and it was only explored several years after the formulation of BCS theory[29]. While we can already appreciate this point, we can proceed formally and confirm that the above intuition works. The solution in the normal state to $U(x), V(x)$ must be

$$\begin{pmatrix} U(x) \\ V(x) \end{pmatrix}_L = e^{i\lambda_N x} \begin{pmatrix} 1 \\ 0 \end{pmatrix} + ae^{-i\lambda_N x} \begin{pmatrix} 0 \\ 1 \end{pmatrix} \tag{2.19}$$

with $\lambda_N = \frac{\epsilon}{\hbar v_x}$ Generically, we must match these two equations and solve for a and c, the reflection and transmission coeffecients. For incident electrons with energy $\epsilon > \Delta$ it is possible to get somewhat more complicated results. However, we are most interested in electrons with energy $\epsilon < \Delta$ and here the results are rather straightforward. In this case, λ_s is imaginary, so $U(x), V(x)$ are exponentially suppressed as their are no electron or hole states within the gap. Full solution does indeed confirm that $|a|^2 = 1$

Now that we have studied a single SN interface we can examine an SNS structure (Figure 2.3). This is essentially equivalent to doing the above problem twice, noting that the phase of the electrons and holes in the normal region will evolve by $\pm\lambda_n d$

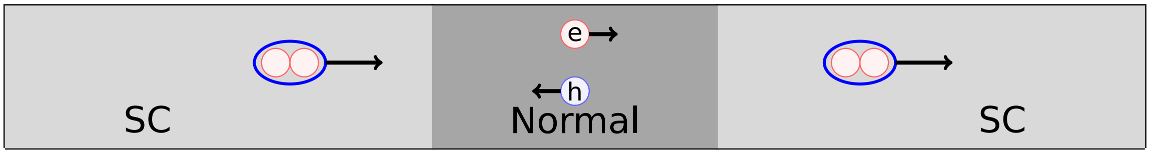

FIGURE 2.3: An SNS device. Cooper pair transport is mediated by successive Andreev reflections.

in the normal region, where d is the distance traveled by the particle from one superconducting contact to the other.

More formally, we initially consider the right superconducting contact. Lets suppose the junction has a phase difference ϕ. Without loss of generality, we will say the phase on the right contact is $\phi/2$ and the left contact is $-\phi/2$. If we are initially considering an electron such that the momentum projection on the x axis is positive, $k_x > 0$, the wave function in the right superconductor $x > d/2$ is

$$\begin{pmatrix} U(x) \\ V(x) \end{pmatrix}_R = d_1 e^{-\tilde{\lambda}_S x} \begin{pmatrix} \tilde{U} e^{i\phi/4} \\ \tilde{V} e^{-i\phi/4} \end{pmatrix} \tag{2.20}$$

for some constant d_1. This is fairly similar to before, with the additional phase factor which we have split between the electron and hole components. In the left contact, we have to note that the coherence factors $\tilde{U}, \tilde{V}$ are swapped because the problem should be identical if we take $x \to -x$ and apply a time reversal operator so that the direction of current also flips

$$\begin{pmatrix} U(x) \\ V(x) \end{pmatrix}_L = d_1' e^{\lambda_S x} \begin{pmatrix} \tilde{V} e^{-i\phi/4} \\ \tilde{U} e^{i\phi/4} \end{pmatrix} \tag{2.21}$$

Matching with the same normal state function as before at both boundaries we find

$$a e^{-i\lambda_N d} = \frac{\tilde{V}}{\tilde{U}} e^{-i\phi/2} \tag{2.22}$$

and

$$ae^{i\lambda_N d} = \frac{\tilde{U}}{\tilde{V}}e^{i\phi/2} \tag{2.23}$$

Dividing these two equations we thus arrive at

$$e^{2i(\lambda_N d - \phi/2)} = \frac{\tilde{U}^2}{a\tilde{V}^2} = \frac{\tilde{U}}{\tilde{V}} = \frac{\epsilon + i\sqrt{|\Delta|^2 - \epsilon^2}}{\epsilon - i\sqrt{|\Delta|^2 - \epsilon^2}} \tag{2.24}$$

where we have made use of $a = \frac{\tilde{U}}{\tilde{V}}$ for a subgap state. Further simplification ultimately yields

$$\epsilon = \pm\hbar\,|\omega_x|\left[\frac{\phi}{2} \mp \arcsin\frac{\epsilon}{|\Delta|} + \pi\left(l \pm \frac{1}{2}\right)\right] \tag{2.25}$$

with $\omega_x = v_x/d$ and l being an integer. The opposite sign solution comes from reversing the direction of the particles in the normal region. This formula is initially unsightly but gives way to two simple limits. If the junction is short, by which we mean that $d << \hbar v_x/\Delta$ then $\hbar\omega_x >> \Delta \geqslant \epsilon$ and we can simply find that $\epsilon = \pm|\Delta|\cos(\phi/2)$ The opposite limit, a long junction, can be found by simply neglecting the arcsin term. Here, there may be a significant number of different solutions for different l, as long as ϵ for a given l is less than Δ.

This $\epsilon(\phi)$ is the Andreev bound state spectrum which is depicted in Figure 2.4[29]. We see that a short junction has an oscillatory dependence on ϕ while the long junction is saw tooth. While it is possible to design a 0D or 1D weak link with few modes, typically a 2D weak link like those studied in this dissertation will have many such modes. We can very straightforwardly connect these modes to the macroscopics of the junction. The total energy of this junction can be arrived at by summing over the occupied Andreev bound states at a given ϕ. On the other hand, we can also get the change in energy of the junction between two phases by integrating IV from from time t_1 when the junction is at phase ϕ_1 to time t_2 when the junction is at phase

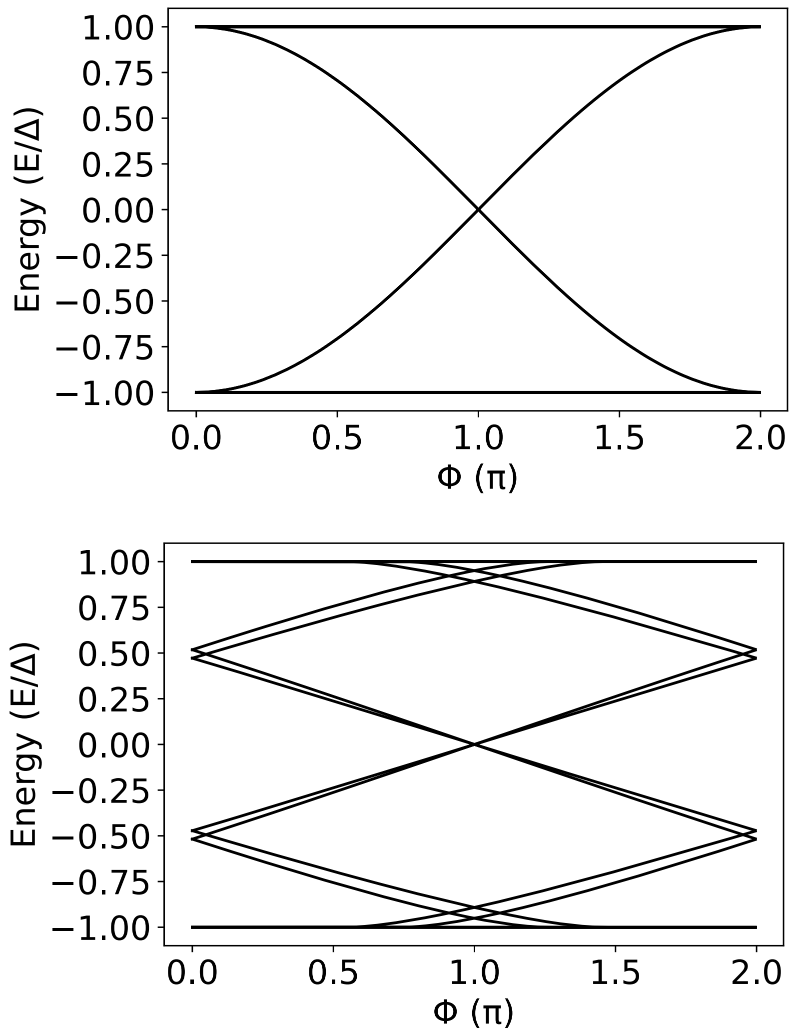

FIGURE 2.4: Top: the ABS spectrum for a single mode short device. The spectrum is sinusoidal, with a phase shift depending on the direction of the current. Bottom: the bound state spectrum for a longer device with two modes.

ϕ_2. In this situation, $V dt = d\Phi$ owing to the AC Josephson relation. This procedure ultimately yields

$$I_C(\phi) = \sum_i -\frac{2e}{h}\frac{\partial E_i}{\partial \phi} \tag{2.26}$$

(we can also arrive at this result by noting that for superfluid systems, phase and particle number are canonically conjugate). This is known as a current phase rela-

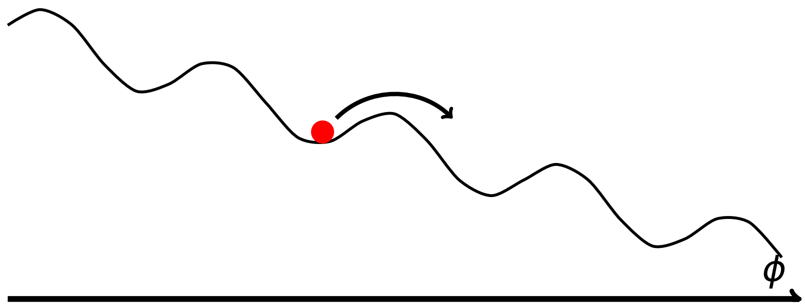

FIGURE 2.5: Tilted washboard potential. The phase particle oscilates in a single minima, until tilting and noise, be it quantum or thermal, allows the phase particle to overcome the barrier.

tionship. While SIS junctions typically show a sinusoidal current phase relationship, here we have seen that SNS devices can show more complicated relationships. While this can arise from junction length, it may also arise from materials properties, as a rigorous calculation requires analyzing the properties of the weak link. For example, graphene weak link devices are predicted to give rise to a skewed CPR because of the materials linear dispersion [30]. Devices with Majorana fermions are predicted to host a 4π periodic current phase component[31].

While the picture presented above is useful, it neglects many important facts related to Andreev bound states in real devices. Beyond the physics of the weak link, it is also important to consider junction temperature, which effects ABS occupation, contact transparency, which typically opens a gap in the subgap states, and scattering within the weak link[32].

2.4 RCSJ and Shapiro Steps

In order to go from the Josephson relations and the CPR to the IV curve of a junction, we need to incorporate a few additional elements into our circuit. Actually, it is almost surprising how few elements it takes to capture the basic behavior of a junction. Typically, we consider a capacitor (which will naturally arise in junction geometry due to coupling between the leads) and a resistor (to model any dissipative processes) in parallel with the junction. This is called the resistively and capacitively shunted junction (RCSJ) or Stewart-McCumber model. By incorporating the two Josephson relations and solving for the circuit we can completely solve for the dynamics of the phase variable. If this circuit is current biased, than the bias current must be equal to the sum of the current through each element. This gives

$$I = \frac{\hbar C}{2e}\frac{d^2\phi}{dt^2} + \frac{\hbar}{2eR}\frac{d\phi}{dt} + I_C \sin(\phi) \tag{2.27}$$

There are a few different ways in which we can intuit this equation

- It is the equation for a damped pendulum. The mass here is proportional to C, the damping is proportional to $\frac{1}{R}$ and the gravitational force is associated with the critical current.

- We can think about this equation as a parallel RLC circuit with a nonlinear inductor (inductance proportional to $\sin(\phi)$). This picture can be useful for internalizing how the junction will respond to changing our device parameters.

- Lastly, and also perhaps most usefully, we can consider the "tilted washboard" picture (Figure 2.5). We associate the phase with a particle sitting in a sinusoidal well. This particle is initially localized to one well and has an intrinsic small amplitude oscillation ($\omega_p = \sqrt{\frac{2eI_C}{\hbar C}}$ in analogy with the pendulum), and also some noise fluctuations. As we apply a DC current to the device, we begin to tilt the well. At some point, we tilt the well enough that the particle can escape its initial minima. What happens afterwards will depend on the system parameters. In a simple picture, the device will either have huge inertia and continue rolling down the well, or huge dissipation and just become localized in the next well.

This last picture is extremely helpful for explaining what is actually happening in the IV curve of a Josephson junction. A sample IV curve is printed below (Figure 2.6).

As was eluded to in the discussion of the tilted washboard potential, if a junction is underdamped (with $Q = \omega_p RC >> 1$, in perfect agreement with a parallel RLC circuit) then the system has significant inertia and small damping. This leads to two significant effects. First, the transition from superconducting to normal is very sharp, because once the particle escapes the first well it is freely rolling down the well, corresponding to the normal state. Secondly, there tends to be significant hysteresis in the IV curve, as the large inertia of the phase particle can cause the particle to remain rolling even if the DC current is lowered once the particle starts running.

The other limit of overdamped junctions leads to a smoother transition between the two states, as the low inertial particle can enter a sort of diffusive regime prior to entering the true normal state. In our equations, this should also prohibit hysteresis, but nanoscale SNS junctions can exhibit hysteresis even if they are overdamped. There is some debate as to whether this arises from heating or from capacitance of the Andreev bound states[33, 34].

We would like to know what happens if we apply an AC current to a Josephson junction. Unfortunately this problem is not particularly analytically tractable, so we instead consider an AC and DC voltage bias $V = V_0 + V_1 \cos(\omega_1 t)$. By the AC Josephson effect, this leads to a phase as a function of time

$$\phi(t) = \phi_0 + \frac{2eV_0}{\hbar} t + \frac{2eV_1}{\hbar\omega_1} \sin(\omega_1 t) \tag{2.28}$$

We can plug this relation into the DC Josephson effect in order to get I_t. Before doing so, we note that this will involve a term involving $\sin(\sin(x))$ which can be expanded in terms of Bessel functions using the identity $e^{ia\sin x} = \sum_{k=-\infty}^{+\infty} J_k(a) e^{ikx}$ we find that

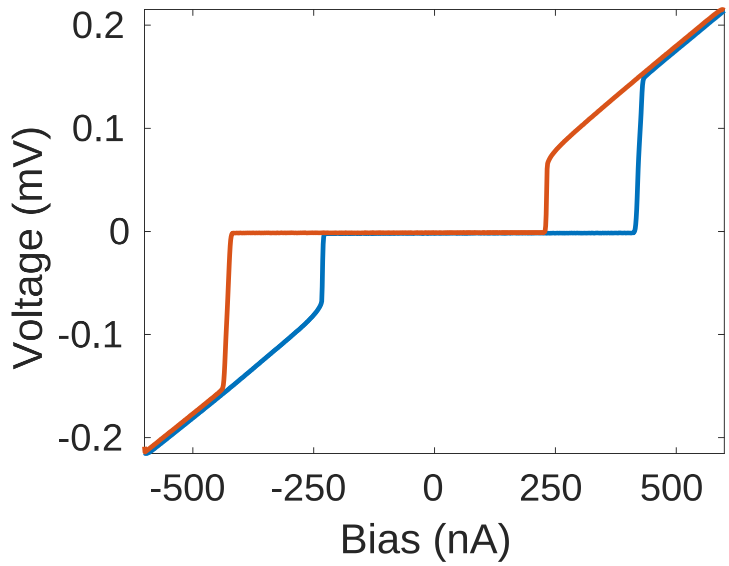

FIGURE 2.6: The VI curve for a standard graphene Josephson junction. Blue corresponds to the forward sweep direction, while orange corresponds to the backwards sweep, showing significantly different switching and retrapping currents.

$$I = I_s + \frac{V_0}{R} = I_c \sum_{k=-\infty}^{\infty} (-1)^k J_k \left(\frac{2eV_1}{\hbar\omega}\right) \sin\left(\phi_0 + \frac{2e}{\hbar}V_0 t - k\omega_1 t\right) + \frac{V_0}{R} \tag{2.29}$$

Generically, the sin factor causes the I_s portion to oscillate and average to zero. However, for $V_0 = k\hbar\omega_1/2e$ the two time dependent factors within the sin cancel out for a given values of k, resutling in a term with a DC average. While this might initially seem like an effect that only matters for a measure zero set of bias voltage values, if the junction has this voltage, than by changing ϕ_0 we see that we can carry a wide range of supercurrent. Specifcally the halfwidth of step k is $I_C J_k(2ev_1/\hbar\omega_1)$.

When current biasing, we find that the device shows steps at well quantized voltages (Figure 2.7). These steps are referred to as Shapiro steps. Essentially, the Josephson junction is a near perfect frequency to voltage converter. This is actually the basis of the modern voltage standards. This effect plays a central role in chapters 3 and 4. Chapter 3 presents a more intuitive picture of how these voltage steps arise.

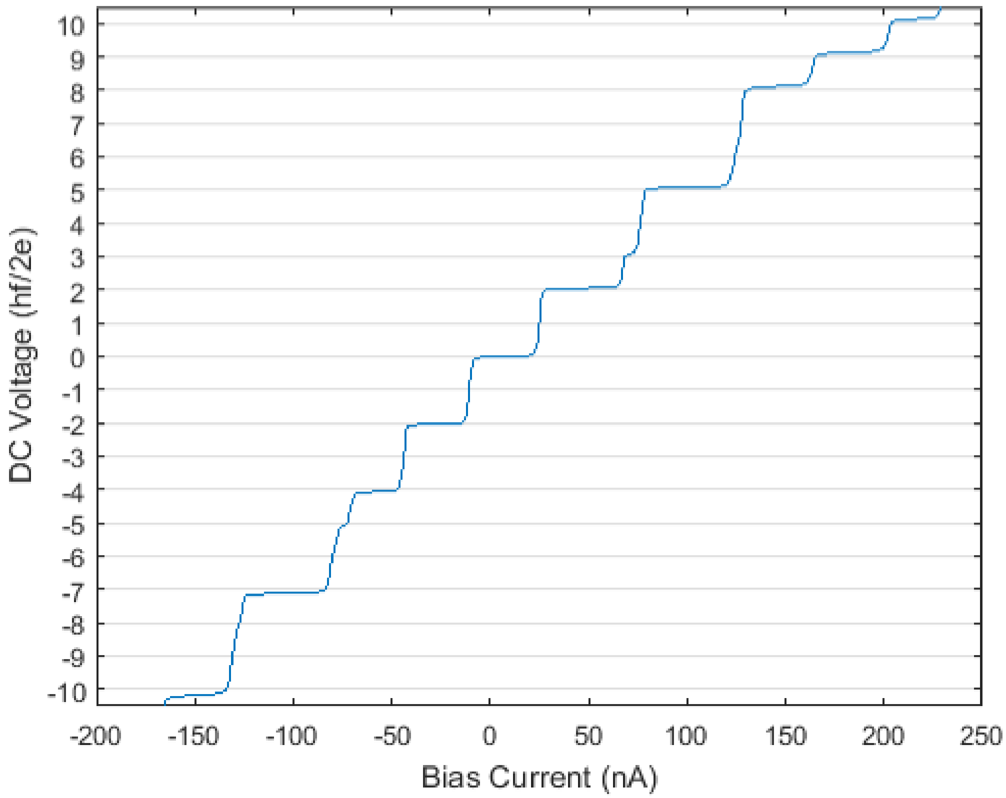

FIGURE 2.7: Voltage as a function of current for an RF driven graphene Josephson junction. This measurement was taken at relatively high RF power applied, as can be seen from the large number of observable steps.

3

Shapiro Steps in Encapsulated Graphene Josephson Junctions

3.1 Introduction

As discussed in Chapter 2, Josephson junctions subject to an external RF radiation demonstrate the inverse AC Josephson effect: the phase difference across the junction locks to the external frequency [35]. As a result, the phase steadily ramps with time, and the $I-V$ curves form "Shapiro steps" of quantized voltage $V = n\hbar\omega/2e$, where n counts the number of periods by which the phase progressed over one period of excitation [36]. The exact mechanisms of the phase locking and its stability were investigated in detail in the 1980s [37]. The extremely precise voltage quantization of the steps is presently utilized in primary voltage standards [38].

Recently, interest in topological Josephson junctions have reinvigorated the use of the AC Josephson effect as a tool to probe a junction's current-phase relation [39, 40]. Missing steps and residual supercurrent associated with the anomalous CPR are some of the signatures which have been explored [41, 42, 43, 44, 45]. Many of these studies are performed at relatively low power and frequency; in this regime the measured maps may be significantly different from the textbook “Bessel function” patterns even in topologically trivial junctions [37].

We studied the inverse Josephson effect in graphene-based superconductor-normal-superconductor junctions. Shapiro steps in this topologically trivial material have been previously explored [46, 47, 48, 49] and used as a reference in the study of topological junctions [42]. We show that a variety of patterns can be obtained within the same junction by tuning the gate voltage and magnetic field. Both the Bessel function regime and the strongly hysteretic regime with “zero crossing steps” are observed. We directly simulate the observed patterns using an extension [50] of the RCSJ model to explain the observed trends, showing some notable differences from predictions based on the conventional model.

One of the unique properties of our junctions is that the superconducting leads are made by sputtering molybdenum-rhenium alloy [51], which has a relatively large gap of 1.3 meV. The sample is measured in a dilution refrigerator with the sample holder temperature of approximately 100 mK, which depends weakly on the applied RF signal. The actual sample temperature under the RF drive could be higher [52]. The GHz drive is coupled by an antenna placed approximately 1 mm away from the sample. The exact value of the RF power reaching the sample is difficult to quantify because of the frequency-dependent coupling between the antenna and the sample, which are not impedance matched. Therefore, we only list the nominal RF power emitted by the generator at room temperature, which is a common practice in similar experiments. To measure the DC voltage across the sample, we perform multiple DC current bias sweeps while keeping the rest of the parameters fixed. The resulting $I-V$ curves are then averaged and numerically differentiated to obtain the differential resistance $R = dV/dI$. 200 I-V curves are averaged for each linecut of the AC Bias - DC Bias figures in this chapter.

This chapter is adapted from Ref[53].

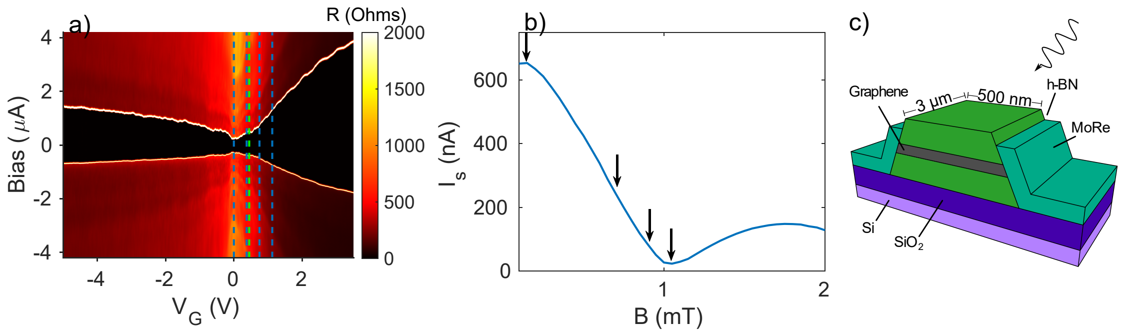

FIGURE 3.1: a) Measured differential resistance of the junction as a function of gate voltage and bias. The central black region corresponds to supercurrent. The current is swept from negative to positive, resulting in the large difference between I_S and I_R. The green dashed line marks the primary gate voltage used throughout the paper (Figures 3.2-3.4); blue dashed lines correspond to gate voltages used in Figure 3.5. b) Switching current as a function of small perpendicular magnetic field, for $V_G = 0.45$ V. This magnetic interference effect is used to tune the critical current of the junction, while holding other parameters constant. Arrows indicate field values used in Figure 3.2. c) Schematic of an encapsualted graphene Josephson junction, subjected to RF irradiation.

3.2 Shapiro Maps

A schematic of the sample and standard characterization measurements performed without RF excitation are presented in Figure 3.1. Figure 3.1a shows the differential conductance measured as a function of bias and gate voltage. The dark region of the map corresponds to supercurrent. As commonly observed in SNS junctions, there is a large difference between the switching current from the superconducting state to the normal state (I_S) and the retrapping current from the normal state to the superconducting state (I_R) [54, 55]. (The value of I_S is slightly lower than the true value of the critical current of the junction, I_C.) Figure 3.1b shows the dependence of I_S on a small magnetic field applied perpendicular to graphene – the "Fraunhofer pattern" [19]. The sensitivity of I_S to magnetic field allows us to conveniently tune the critical current while holding other parameters constant.

In Figure 3.2, we compare patterns of Shapiro steps measured at frequencies of 3

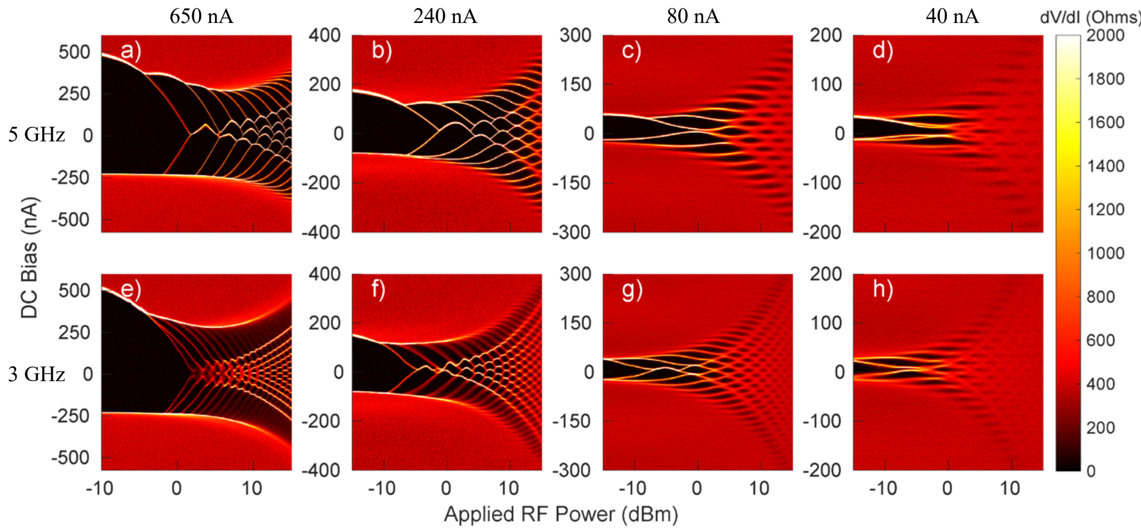

FIGURE 3.2: The maps of differential resistance showing Shapiro steps as a function of the DC bias current, I, and RF power, P_{RF}. The gate voltage for this figure through Figure 4 is set at $V_G = +0.45$ V as measured from the Dirac peak ($V_D = -10$ mV is negligible in this sample). The maps are measured at two frequencies (top row: 5 GHz, bottom row: 3 GHz) and different switching currents (left to right: I_S = 650, 240, 80 and 35 nA), as tuned by perpendicular magnetic field). An important dimensionless parameter controlling the overall behavior is $\Omega = \omega/\omega_P \propto \omega/\sqrt{I_S}$. The pairs of panels (a and f), (b and g), (c and h) correspond to roughy equal values of Ω and therefore appear similar. We observe the expected trends, according to which at high Ω (right panels) the plateaus are centered at fixed voltages and their vertical extent is described by the Bessel functions. In the opposite limit of low Ω (left panels), many features of the maps become hysteretic, and the $n \neq 0$ plateaus cross zero bias.

and 5 GHz and several values of magnetic field which are marked in Figure 3.1. The maps in Figure 3.2 present the differential resistance R; the dark regions correspond to the Shapiro steps of constant voltage, for which $R = 0$, and the narrow bright lines correspond to the transitions between these steps. As in Figure 3.1a, the current bias is swept from negative to positive, resulting in pronounced hysteresis in many of the transitions between the Shapiro steps. Some of the negative steps are found to cross zero and extend to positive currents, an effect referred to as "zero crossing steps" [37].

Following Ref. [37], we introduce convenient dimensionless parameters, Ω =

ω/ω_P, and $\sigma = 1/Q$, which are crucial in determining the pattern of Shapiro steps. (Here, ω is the RF drive frequency, $\omega_P = \sqrt{2eI_C/\hbar C}$ is the bare plasma frequency, and Q is the quality factor of the junction.) Ω grows left to right and bottom to top in Figure 3.2; σ grows right to left. Shapiro patterns measured at different ω and I_S but comparable Ω, (see the three pairs (a and f), (b and g), and (c and h) in Figure 3.2) demonstrate qualitative similarity, particularly in the region of zero crossing steps. We further discuss how Ω and σ influence the shape of the plateaus in the supplementary.

For the smallest I_S (highest Ω, Figures 3.2c, d, and h), the pattern of Shapiro steps follows the Bessel function dependence [19]. In this regime, the extent of the steps in the bias direction is roughly equal to $I_C J_n(\frac{2eV_{AC}}{\hbar\omega})$ where J_n are the Bessel functions. [56]. The steps are centered at $I = V_n/R_j$, where R_j is the effective DC shunt resistance of the junction. Experimentally, we can extract the effective value of the shunt resistance, $R_j \approx 300$ Ohms, independent of I_S through Figure 3.2. Note that this value is comparable, but slightly smaller than the normal resistance of the junction $R_N \approx 450$ Ohms [19].

As the critical current increases on the left panels of Figure 3.2, the patterns change due to the coexistence of multiple stable steps for a given bias value [49]. While some of the boundaries still resemble the Bessel functions, the plateaus start to overlap, because the width of plateaus $\sim I_C$ becomes larger than the distance between the centers of the plateaus, V_n/R_j. Eventually, the plateaus are no longer centered around a fixed current bias of V_n/R_j, but instead emerge sequentially from the normal state boundary and diagonally descend toward zero bias. At high RF power multiple step boundaries intersect, resulting in an intricate net of transitions (Figures 3.2a, b, f and g). Finally, for the lowest Ω (Figure 3.2e), the ± 1 steps no longer reach zero upon the first approach, and the $I-V$ curves show a pronounced region of non-quantized voltage close to zero bias (P_{RF} between 0 and 3 dBm).

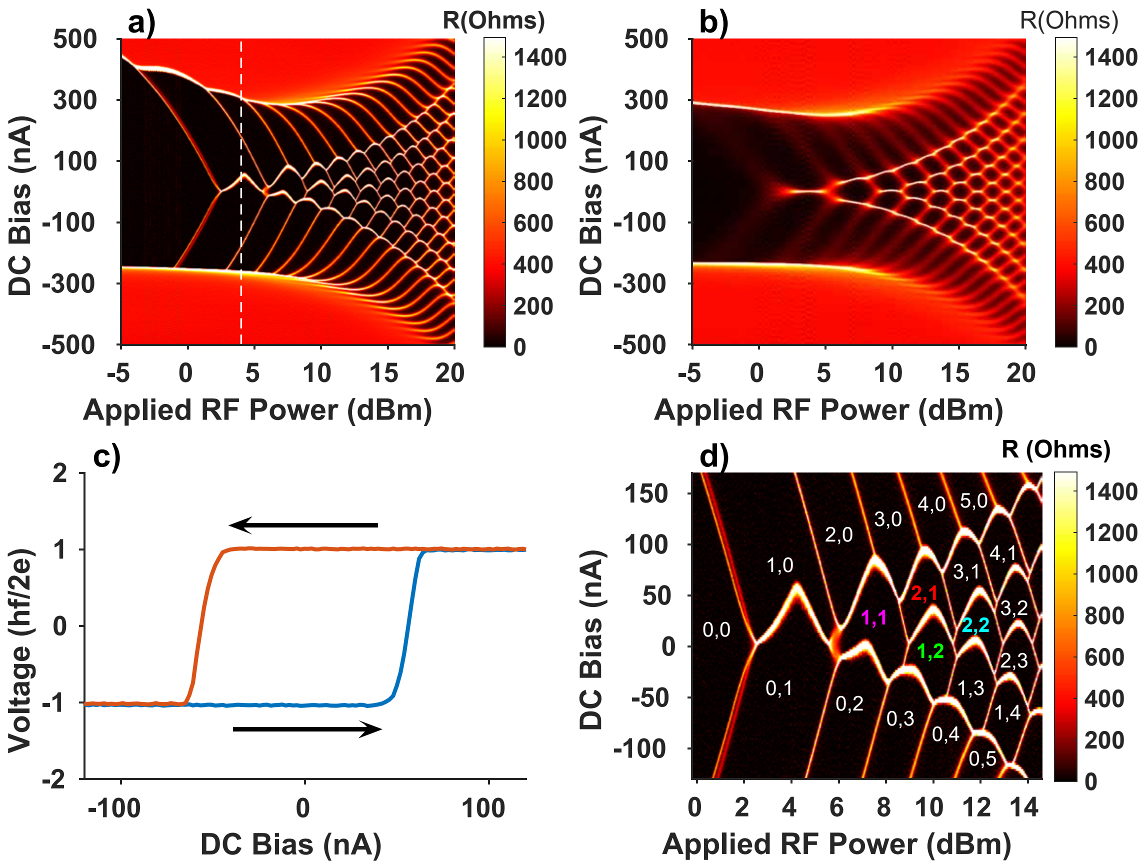

FIGURE 3.3: a) Differential resistance as a function of I and P_{RF} reproducing Figure 1a (f = 5 GHz, I_S = 650 nA, sample holder temperature T = 100 mK). b) A map identical to (a) but measured at T = 1.5 K, at which point the hysteresis is largely suppressed. c) A cut through the map (a) taken at P_{RF} = 4 dBm (at the dashed line), which shows the hysteretic switching between the n = 1 and n = −1 steps depending on the sweep direction. d) A zoom of map (a), with the different plateaus labeled by (p, q) as described in the text.

We now concentrate on the parameters of Figure 3.2a which is reproduced in Figure 3.3a. Figure 3.3c shows a line cut extracted from Figure 3.3a (blue), as well as a similar line measured for the opposite sweep direction (red). This confirms that the asymmetric features seen in Figure 3.2 are indeed due to hysteresis, and that for many parameter values multiple solutions are simultaneously stable. Figure 3b is taken under the same conditions, but at a higher temperature (T=1.5 K). At this temperature, the hysteresis of the Shapiro features is nearly gone, and a regular pattern emerges, resembling a distorted honeycomb.

Ultimately, there is little reason to think that the effects observed here are attributable to anything particularly special about the graphene, because Shapiro steps should only be sensitive to I_C and the CPR. However, attempts to model these results numerically with the standard RCSJ simulations are ultimately fruitless – these simulations show chaotic beavior with irregular transitions between voltage steps, leading to maps that bear little resemblance to the experimentally observed pattern of steps. The ingredients which are needed to correctly simulate these results are the subject of the next section.

3.3 Simulations and Phase Space Trajectories

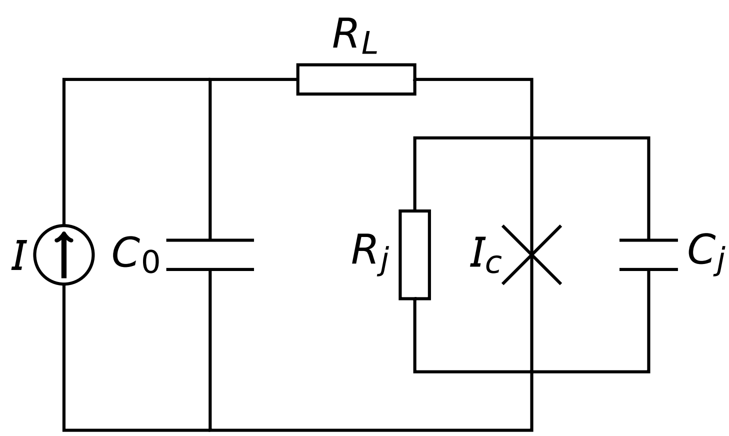

FIGURE 3.4: Diagram of the circuit used to simulate the dynamics of the Josephson junction. In practice, C_j is negligible and is omitted from further consideration.

To simulate the behavior of the junction, we use a modified RCSJ model as illustrated in Fig. 3.4 [57]. We start with a junction with critical current I_C, which is shunted by a resistor R_j and a capacitor C_j, where R_j represents the dissipation in the Josephson junction and C_j is the capacitance between the two superconducting leads. In the experiment, the Josephson junction is further connected to four 150 μm $\times$ 100 μm bonding pads by Cr/Au leads. The capacitance of the bonding pads, C_0, and the resistance of the leads, R_L, must be taken into account to properly simulate the junction dynamics. The four bonding pads are arranged such that the effective capacitance is equal to that of one bonding pad to the back gate, which would yield 1.8 pF for 280 nm thick SiO_2. At room temperature, the capacitance between two bonding pads and bonding wires connected to the chip carrier by bonding wire was measured to be slightly higher, around 2.5pF, which was the value used in the simulations. In practice, similar maps have been simulated using a range of C_0 values.

The resistance of the evaporated Cr (5 nm)/Au (45 nm) film was measured to be 0.5 Ohm/□, from which we estimate that R_L is a few tens of Ohms for our typical devices. We use a reasonable value of R_L = 50 Ohms for our simulations The estimated inductance of the leads for the sample is on the order of 30 pH, and thus has a negligible effect at the relevant plasma and drive frequencies. Considering this inductance may be important in other circumstances but also notably increases simulation time. Finally, R_j = 300 Ohms is determined from the current corresponding to the center of the Shapiro plateaus in the Bessel function regime, $I_n = n\hbar\omega/R_j$. In accordance with the experiment, we assume that R_j does not depend on magnetic field. The same value of R_j = 300 Ohms is used to simulate all panels in Figure 3.5.

The microwave injection from the antenna can be modeled by an AC current, $I_{AC} = I_{RF} \sin \omega t$ where I_{RF} is the current amplitude and ω is the microwave frequency. To achieve qualitative agreement with the experiment, we found it necessary to add a noise source, which facilitates switching between the plateaus. We lump the thermal noise of the resistors and any other possible noise in the system into a broadband Gaussian noise I_N. The magnitude of the noise used in our simulations is listed in the table and discussed at the end of this text. Overall, the current source I contains three components, the bias current, I_{bias}, the microwave radiation current, I_{AC} and the thermal noise, I_N.

$$
\begin{aligned}
I &= I_{bias} + I_{RF}\sin\omega t + I_N(t) \\
&= C_0\frac{dV}{dt} + I_C\sin\phi + \frac{\hbar}{2eR_j}\frac{d\phi}{dt} + \frac{\hbar C_j}{2e}\frac{d^2\phi}{dt^2} \\
V &= \frac{\hbar}{2e}\frac{d\phi}{dt} + R_L\left(I_C\sin\phi + \frac{\hbar}{2eR_j}\frac{d\phi}{dt} + \frac{\hbar C_j}{2e}\frac{d^2\phi}{dt^2}\right)
\end{aligned}
\tag{3.1}
$$

The dynamics of the circuit in Fig. 3.4 is described by Eq. (4.2), where ϕ is the superconducting phase difference across the junction, V is the voltage across the capacitor C_0. Solving this third order differential equation numerically gives $\phi(t)$, from which we can derive the DC voltage across the junction, $V_j = \left\langle \frac{\hbar}{2e}\frac{d\phi}{dt} \right\rangle$. Note that C_j is about 4 orders of magnitude smaller than C_0 for the device studied here. We numerically confirmed that C_j can be neglected under this condition, simplifying the above to a second order differential equation. The experimental curves strongly depend on the bias sweeping direction. To emulate the bias sweep, we use the steady solution of $\phi(t)$ at a given I_{bias} as the initial condition for solving the differential equation at the next value of bias, $I_{bias} + \delta I$, where δI is the incremental bias step.

Figures 3.5a,b show numerical simulations which reproduce most of the features in Figures 3.3a,b. These simulations allow us to trace the time evolution of the phase within each cell of the Shapiro map. The examples of the $\phi(t)$ are shown in Figure 3.4c for several neighboring cells. By analyzing these traces, a rather simple qualitative picture emerges, represented schematically in Figure 3.4d: For each cycle of RF excitation, the phase progresses over p minima of the washboard potential and then retraces q of them backward. The overall change of phase is $2\pi(p-q)$, and the index of the resulting Shapiro step is $n = p - q$. This behavior has been previously identified in the Bessel function regime [37, 58]. In Figure 3.3d, we zoom in on the data of Figure 3.3a and label select cells by their (p, q) indexes. Note that in the resulting regular pattern, each cell in the central part of the map has six

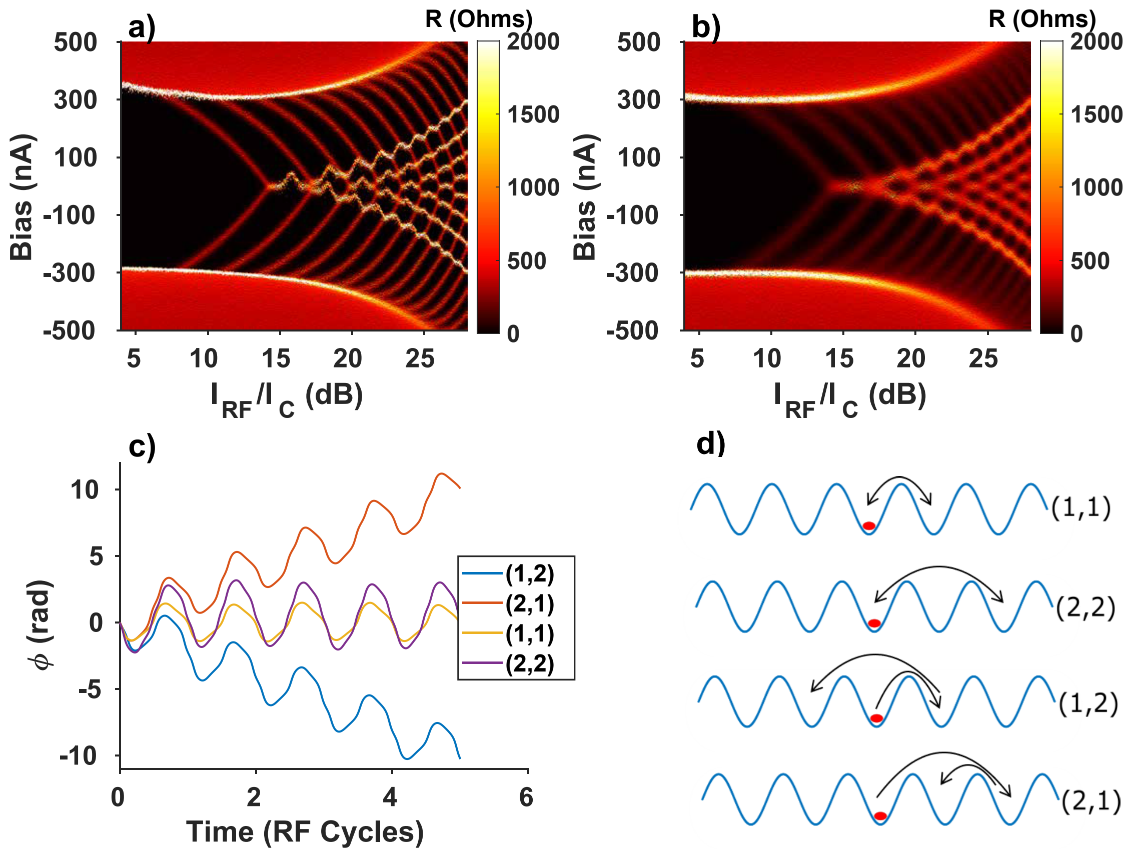

FIGURE 3.5: a,b) Simulation of dV/dI for different noise levels, to be compared to R_L = 50 Ohms, R_j = 300 Ohms, I_C = 540 nA, C_0 = 2.5 pF and f = 5 GHz. To reproduce the experiment, the simulation starts at the lowest DC bias, averages over 500 RF cycles, and then uses the final values of ϕ and $\frac{d\phi}{dt}$ as the initial conditions for the next value of bias. Ten bias sweeps are produced in this manner and then averaged to reduce noise. c) Numerical traces of $\phi(t)$ on various plateaus labeled by the pairs of (p, q) (see text). d) Schematic of the washboard potential and the four types of phase evolution corresponding to (c). The top two schematics represent different forms of $n = 0$, while the bottom two both show $n = \pm 1$.

neighbors. The two neighbors in the vertical direction have the same total number $p + q$ while n differs by two. The four neighbors on the left/right have either p or q decreased/increased by one.

Figure 3.6 shows simulated Shapiro maps at several values of the critical current, intended to be compared with the 5 GHz data of Figure 3.2. Remarkably, we are able to reproduce the four experimental maps in Figure 3.2a-d by changing only I_C,

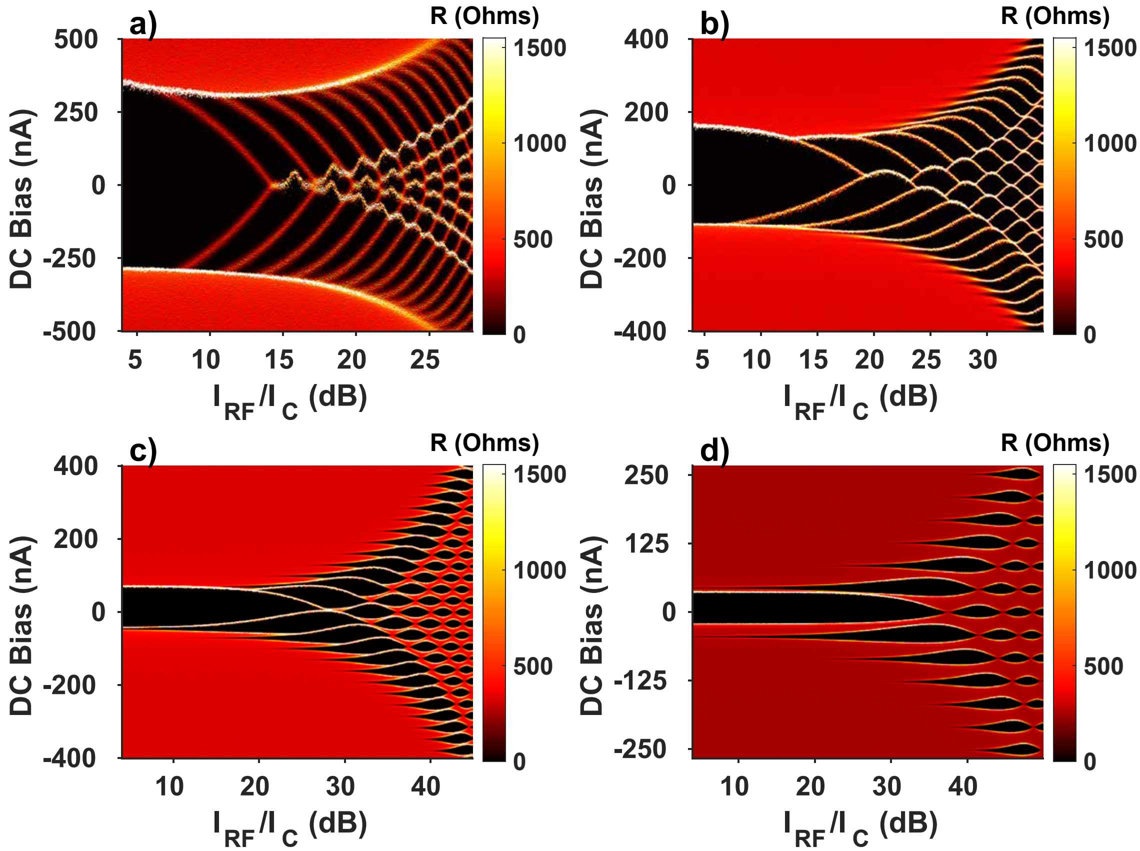

FIGURE 3.6: Simulations of the differential resistance maps at 5 GHz for comparison to Figure 2a-d. The values of I_C used are, from left to right, 540, 200, 80 and 40 nA. Other parameters are kept the same as in Figure 3 of the main text: $C_0 = 2.5$ pF, $R_L = 50$ Ohms and $R_j = 300$ Ohms.

which is the only parameter we expect to be influenced by magnetic field. The values of $C_0 = 2.5$ pF, $R_L = 50$ Ohms, and $R_j = 300$ Ohms are kept the same in all panels.

It is instructive to qualitatively consider the circuit in Figure 3.4 after C_j has been neglected and compare it to the conventional RCSJ model. A key distinction between our work and the conventional RCSJ model can be seen by considering the $\Omega - \sigma$ map (see e.g. Ref. [37]). Here, $\Omega = \omega/\omega_P$ is the reduced drive frequency, and $\sigma = 1/Q$ characterizes the strength of dissipation. Most importantly, the resistor R_L in our case is connected in series with the capacitor and the non-linear inductance of the junction. As a result, the definition of the quality factor is inverted compared to the RCSJ, e.g. higher R_L corresponds to stronger dissipation.

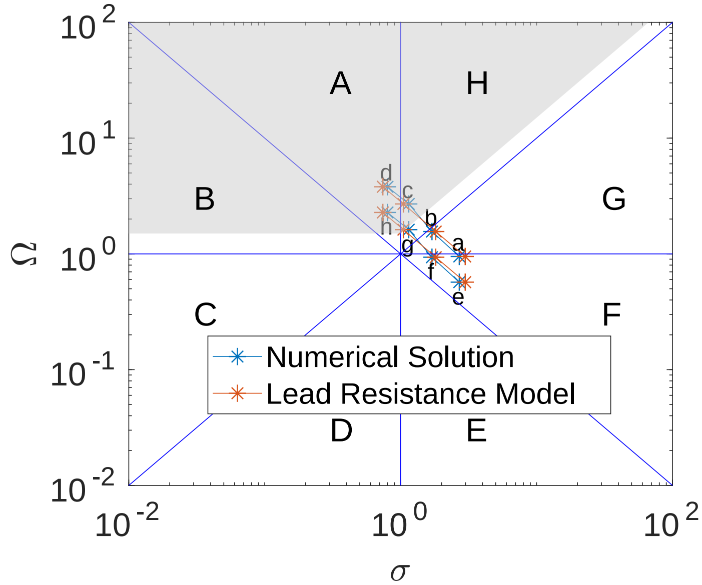

FIGURE 3.7: Extracted parameters for the data of Figure 2, plotted as a function of dimensionless parameters Ω and $\sigma = 1/Q$, defined in the text. In the grayed out region Bessel function behavior is expected.

We extract ω_P and σ by plugging the full model into a circuit simulator, with the junction replaced by an inductor of the corresponding Josephson inductance, to extract both the resonant frequency and the -3 dB frequencies. We also calculate the anticipated values of ω_P and σ by using a simple three element model involving the just C_0, R_L and Josephson inductance. We find that it matches the full simulations quite well – the relatively large junction resistance R_j is found to have negligible effect on ω_P and σ.

The width of the Shapiro steps in the I-V curve is often expected to follow the Bessel function dependence on the applied RF power, as discussed in Chapter 2. A small Josephson inductance (high critical current) can lead to the junction being current-biased by other circuit elements rather than voltage-biased. Since the Josephson junction is a non-linear element, the mostly sinusoidal current would then produce a highly distorted and non-sinusoidal voltage across the junction, violating the assumptions leading to the Bessel functions.

In the conventional current biased RCSJ model, Bessel function behavior is expected in octets A, B, F, G and H of the map [37]. Based on our analysis, in our case the Bessel function behavior is expected only in regions A, B and H. Correspondingly, segments of Bessel functions are visible as plateau boundaries in panels b-d, g and h of Figure 3.2. Further, in the RCSJ model, zero crossing steps are exclusive to one of the Bessel function octets, B[37, 59, 60]. In our case, we find zero crossings in maps a, b, g, and f, which are instead localized in octets F, G and H.

We argue that zero crossings cannot be predicted in our model solely based on parameters Ω and σ of Figure 3.7. In fact, the existence of the Shapiro steps is controlled by the so far neglected junction resistance, R_j. Although R_j is too large to significantly influence the junction dynamics, it sets the position of the Shapiro steps at $I_n = n\hbar\omega/eR_j$. Considering for clarity the Bessel function regime, the width of the plateaus is $I_C J_n(2eV_{AC}/\hbar\omega) < I_C$. We expect to observe zero crossing if the width of the plateaus exceeds I_n, which corresponds to $eR_jI_C \gg n\hbar\omega$. We conclude that larger $I_C R_j$ product is beneficial for observation of zero crossing steps. Finally, suppressing Ic by magnetic field keeps the centers of the plateaus fixed at $n\hbar\omega/eR_j$ while reducing their width. As a result, the steps no longer cross zero in maps c,d and h of Figure 3.2.

Note that the above discussion of dynamics was simplified by the assumption that R_j is large relative to the other elements in the system. In the limit of low R_j, we would go back to the conventional RCSJ model.

3.4 Gate Voltage Dependence

Finally, we look at the gate voltage dependence of the maps in Figure 3.8. While gate voltage influences many parameters, the most significant effect is on I_S and R_j, the latter decreasing by about a factor of roughly 4 between Figures 3.8a and 3.8d. We find that near the Dirac peak the hysteresis is very large (Figure 3.8a), while further away from the Dirac peak the hysteresis of the transitions between the plateaus is significantly suppressed (Figure 3.8d). This suppression is partially explained by increased damping, rather than the purely thermal smearing as observed in Figure 3.5b. However, in order to reproduce the data measured at larger gate voltage, we find that it is also necessary to increase the simulated noise level. We list the noise level used in all simulations in the supplementary. In general, the noise in our simulation could represent a number of possible sources, but we do not attempt to

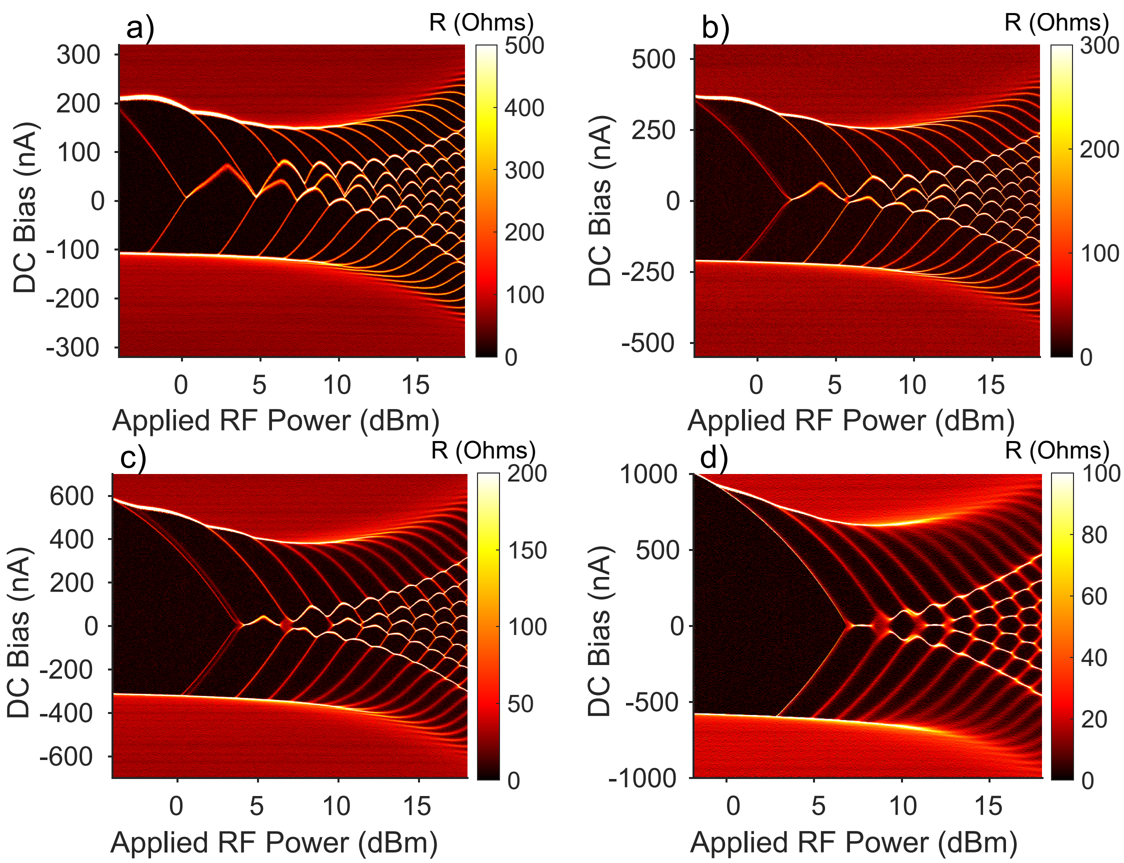

FIGURE 3.8: a-d) Shapiro maps for gate voltages of 0, 0.375, 0.75 and 1.125 V, respectively. Near the Dirac peak, the hysteresis is the most pronounced, with a gradual decline in hysteresis at higher gate voltages. The higher doping both lowers the junction resistance R_j (resulting in higher dissipation) and increases the critical current.

relate the simulated noise to its physical origins. Noise processes in ballistic SNS junctions require further study both in the equilibrium case and under RF drive.

Next, we reproduce the gate voltage dependence measured in Figure 3.8 via simulations. Between the four maps of Figure 3.9, we adjusted the values of I_C and R_j, where the former can be obtained from the value of the switching current at zero RF power, and the latter could be roughly extracted from the positions of the Shapiro steps, $I_n = n\hbar\omega/R_J$.

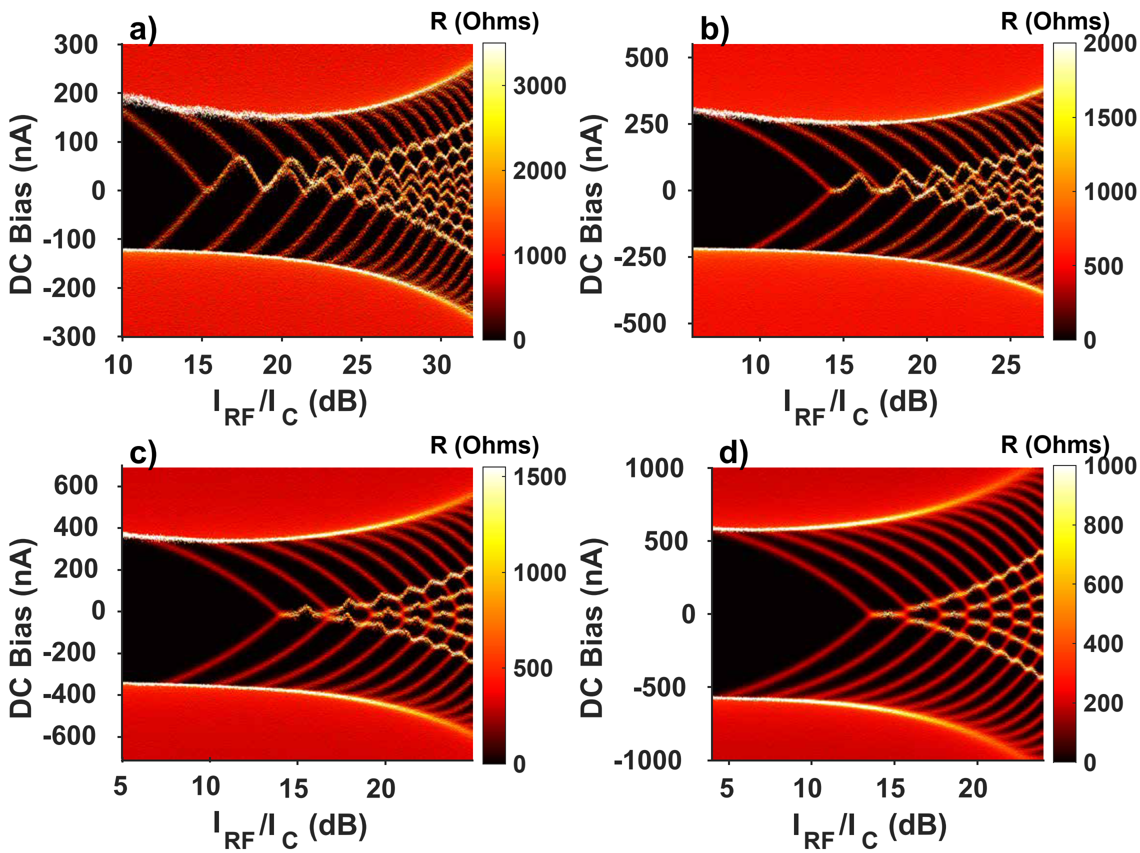

FIGURE 3.9: Simulations of differential resistance maps corresponding to Figure 5 of the main text, measured at different gate voltages. We use the values of $R_j = 850, 500, 300, 180$ Ohms and $I_C = 350, 500, 600, 800$ nA in panels (a) to (d).

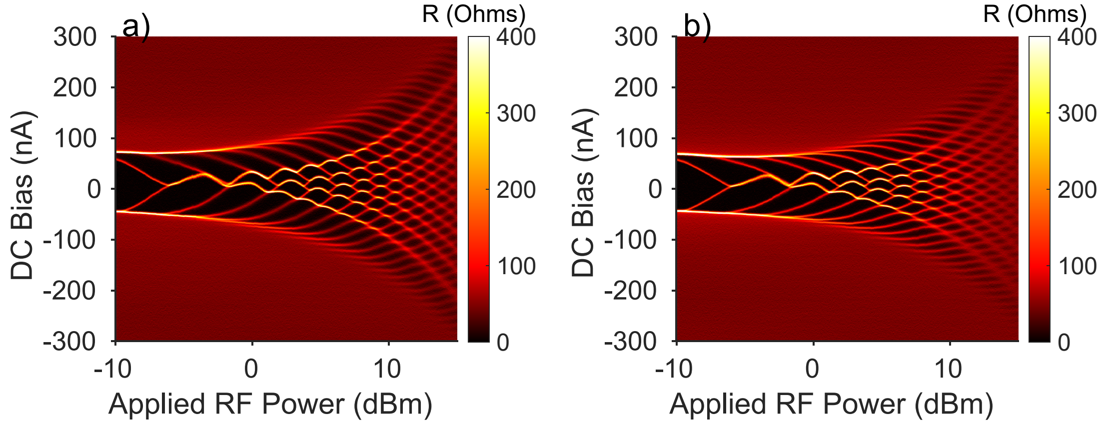

FIGURE 3.10: Two maps of Shapiro steps measured at a) the central lobe and b) the first lobe of the Fraunhofer pattern in Figure 1b. Magnetic field is tuned so that the values of critical current are very similar. We conclude that magnetic field primarily affects the dynamics of the junction through the value of I_C, without influencing other parameters.

3.5 Additional Considerations: Andreev Bound States, CPR Dependence and Heating

In this section, we consider a few more details and how they effect the observed Shapiro step patterns. Throughout this chapter, we have assumed that the effect of magnetic field is limited to changing the value of I_C without influencing other parameters of the system. To verify this assumption, in Figure 3.10 we present two maps measured at very similar values of the critical current, but with magnetic field fixed respectively at the central and the first lobe of the Fraunhofer pattern of Figure 3.1b. While the spatial distribution of supercurrent should be very different in the two maps (necessitating a change in the Andreev bound states), we find minimal differences between the plots. We conclude that it is reasonable to model the system dynamics assuming that magnetic field only tunes I_C while keeping the other parameters fixed.

Figure 3.2d shows strong fractional Shapiro steps [61], although there are no signs of fractional steps in the measurements with higher I_C. Our simulations are in an

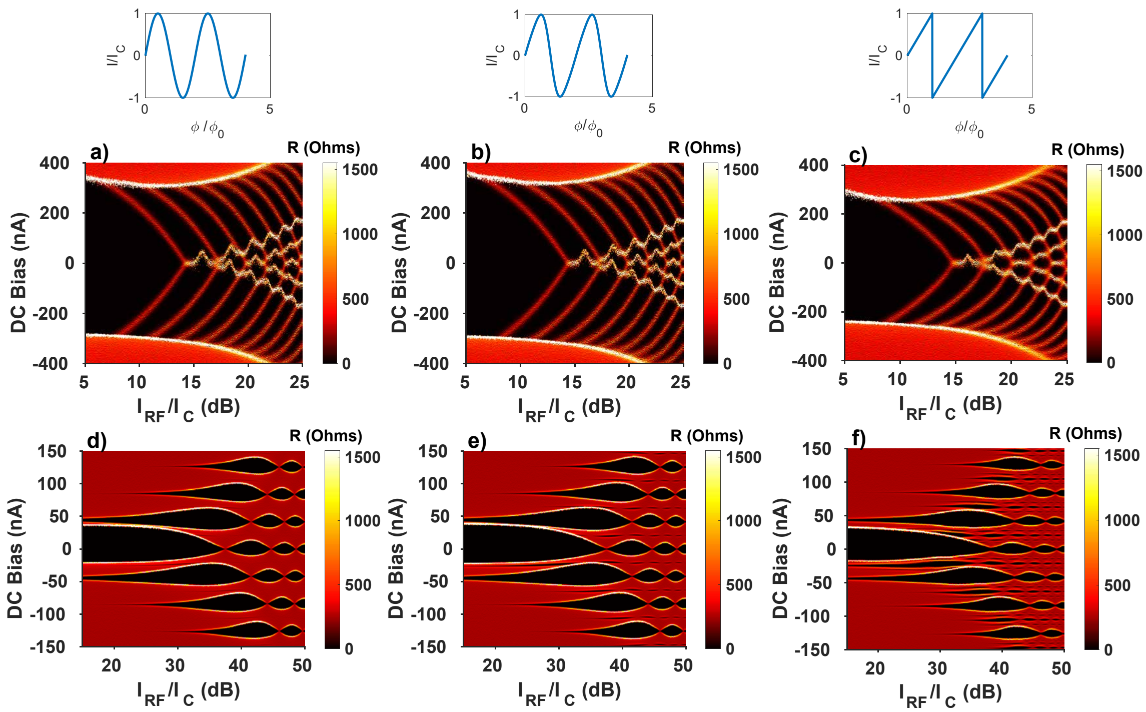

FIGURE 3.11: Middle row: Simulations corresponding to Figures 2a and S3a with the skewness of the CPR increasing from left to right (the CPRs are shown in the insets). Even severe skewness does not give rise to fractional steps, although it does slightly alter the map in ways akin to changing parameters such as I_C and R_j. Bottom row: Simulations corresponding to Figures 1d and S2d with the same range of CPR skewness. In this regime, the CPR gives rise to enhanced fractional steps. Top row: CPRs corresponding to the figures below.

agreement with the experimental results, showing that a skewed CPR has minimal effect on a sample in the strongly hysteretic regime. Intuitively, we understand the hysteresis of the high I_C maps as arising from regions of overlapping stability of integer steps. Thus it may be expected that for such parameters the fractional steps are less stable compared to overlapping integer steps.

For comparison to the experiment, we took our simulation for Figures 3.2a and 3.2d and employed CPRs with varying degrees of skewness [62, 63]. In the top row, $I_C = 540$ nA, corresponding to Figures 3.2a and 3.6a; in the bottom row, $I_C = 40$ nA, corresponding to Figures 3.2d and 3.6d. The three columns correspond to: sinusoidal CPR (left), a slightly skewed CPR, $I(\phi) = I_C[\sin(\phi) - 0.2\sin(2\phi) + 0.04\sin(3\phi)]$

(middle); and a maximally skewed sawtooth CPR (right). The insets in the top panels demonstrate the corresponding CPRs. For large I_C simulations, increasing the skewness of the CPR only slightly distorted the map, but did not give rise to any additional plateaus. For small I_C, increasing the skewness resulted in increasing fractional plateaus. Surprisingly, for small I_C even a perfectly sinusoidal CPR shows some half-quantized steps (Figure 3.11d). We attribute this behavior to the high frequency environment, which gives rise to some effective skewness. Comparing these simulations to the measured data, we find that the slightly skewed CPR appears to most accurately reproduce the strength of the fractional steps, as expected.

Recent work has shown that the effect of RF heating on a nanoscale SNS junction can be quite significant, reaching a few Kelvin for high RF power plateaus [52]. In our case, heating is likely substantial too, but the temperature rise appears to be smaller. Namely, by comparing Figures 3.5a (base temperature) and 3.5b (T=1.5 K): the patterns are different even at the highest RF power, therefore the sample temperature in 3.3a is likely to be less than 1.5 K.

We can directly estimate the temperature of the junction from the power dissipated in the resistor R_j. The heating of R_L can be neglected, as R_L represents the large metallic leads, which should cool more efficiently than the small volume of the junction. For the first Shapiro step, the power could be estimated as $(\frac{\hbar\omega}{2e})^2/R_j \approx 0.4$ pW. Here we assume that the AC component of the voltage is smaller compared to the DC component $\frac{\hbar\omega}{2e}$. At high RF power, the AC voltage across R_j could be large, even if the DC voltage and current are zero, as could be judged from the simulations of $\phi(t)$ in Figure 3.5d. As an example, we estimate the AC voltage for zero bias on the (5,5) plateau (see the notation in Figure 3.3). In this case, during each cycle, the phase moves by 5x2π and then returns back. The resulting voltage is ≈ 10 times larger than in the previous estimate, resulting in ≈ 40 pW of dissipated power.

The superconducting gap blocks cooling through the leads, which would be the leading cooling mechanism for samples with normal contacts. Therefore, the electrons of the junction must cool through the electron-phonon coupling. Unfortunately, the question of electron-phonon coupling in encapsulated graphene is complicated. There are good reasons to believe that most of the cooling occurs near the edges of graphene, resulting in $P \propto T^3$ behavior instead of $\propto T^4$ expected in the clean case [64]. Taking the value $P = 30$ pW/K$^3T^3$ from prior work on encapsulated graphene devices [65], and scaling it by circumference of the sample, results in $P \approx 15$ pW/K$^3T^3$. This yields temperatures in the 0.3-1.4 K range for 0.4-40 pW of heating.

The simulations do not incorporate any heating effects which limits our ability to simultaneously match the high power and low power results. Similarly, there is no attempt to incorporate the mechanism that gives rise to the large difference between I_S and I_R in SNS junctions, although this seems to have minimal impact on matching the simulation to the experimental data outside of the low power regime.

3.6 Data from a Second Device

To confirm reproducibility of our results, we have measured an additional junction. The second device studied featured a smaller length (200 nm) while the contact width was identical (3 μm) to the primary junction studied. Figure 3.12 mirrors Figure 3.2a-3.2d, with I_C being controlled by magnetic field. Figure 3.13 studies the gate voltage dependence at the same frequency and zero magnetic field, showing suppression of the zero crossing hysteresis at higher doping. High quality graphene Josephson junctions tuned near the Dirac peak thus appear to be a reliable recipe for observing zero crossing steps.

3.7 Conclusion

In conclusion, we have studied the AC Josephson effect in a non-topological graphene junction, which allows one to directly tune many of the relevant parameters. Our

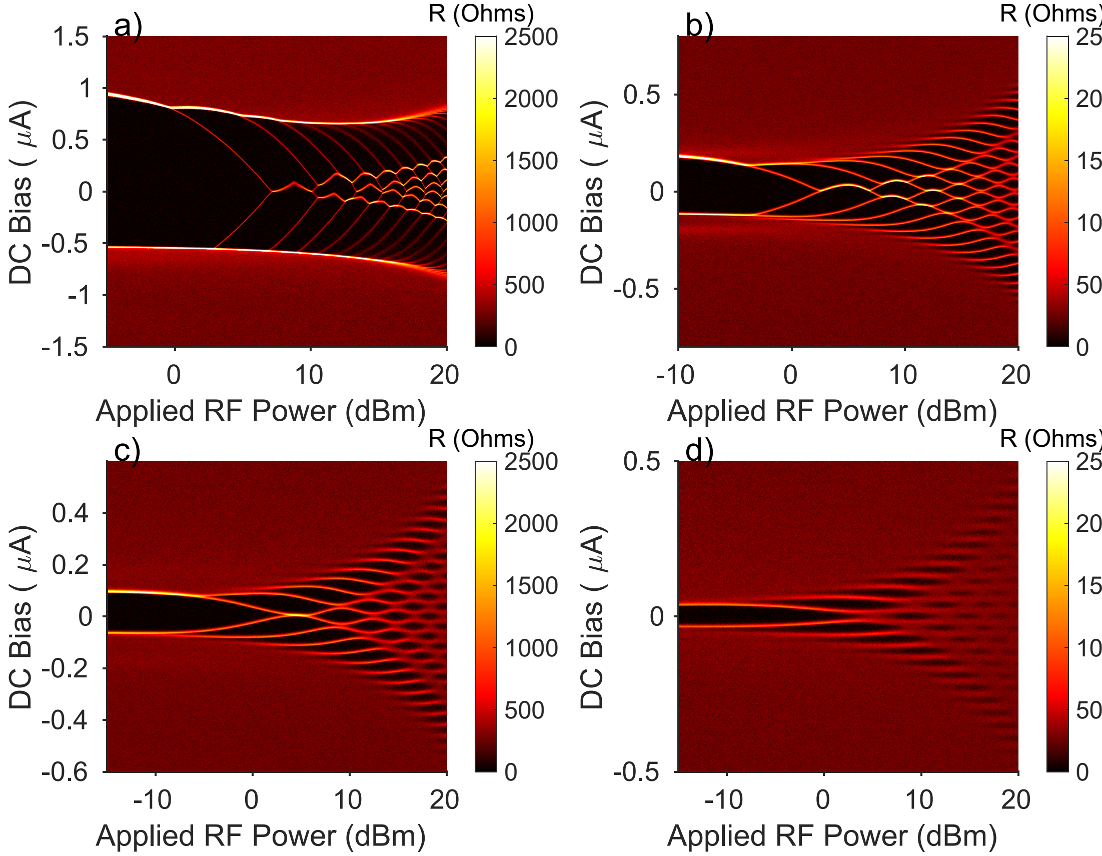

FIGURE 3.12: Differential resistance measured as a function of I_{DC} and P_{RF} at 5 GHz in the second sample. Once again, small magnetic field is used within the first Fraunhofer lobe to modify the critical current. We observe zero crossing steps for the two larger critical currents and Bessel function behavior for the smallest I_C.

results demonstrate the important role played by the local electromagnetic environment in determining the shape of Shapiro steps in nanoscale junctions. The type of samples studied here provides a highly tunable platform to probe the unexplored aspects of driven-dissipative dynamics of a quantum system. Understanding the variety of Shapiro patterns obtained in a prototypical graphene SNS junction will help to identify the non-trivial features in junctions made of topological materials [41, 42, 44, 43]. It also opens interesting perspectives for studying multi-terminal junctions [66, 65, 67], which could reveal topological bands when subject to RF drive [68, 69]. Finally, since the Hamiltonian of the RF-driven junction is periodic

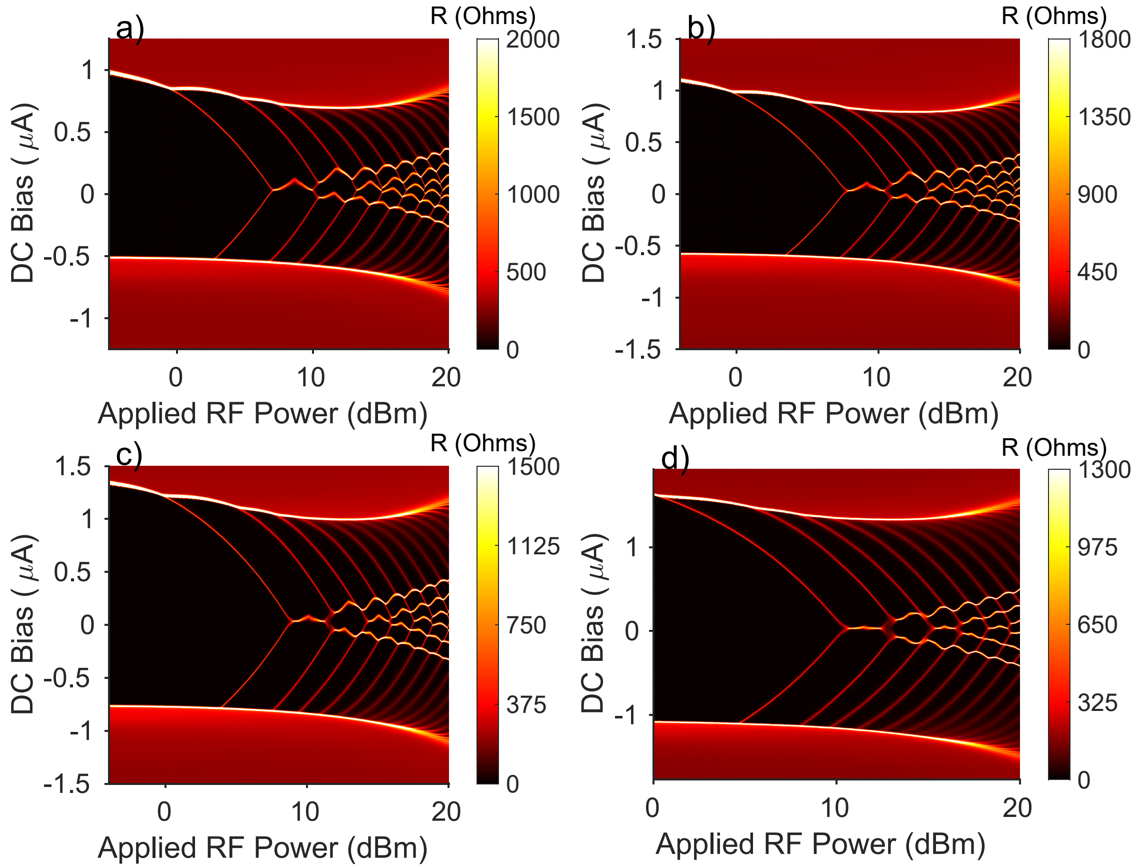

FIGURE 3.13: Bias-power maps of the second device at several gate voltages, from left to right: 0.5 V, 1 V, 1.25 V and 1.5 V. The Dirac peak in this sample is around 0.5 V. Similar to the main sample, the hysteresis of the boundaries between the Shapiro steps is reduced at higher doping.

in the phase difference and time, it could be considered in the context of Floquet physics, potentially resulting in topologically non-trivial bands (see e.g. Ref. [70]).

4

Bistability in RF Driven Graphene Josephson Junctions

4.1 Introduction

Electronic nanoscale systems have recently arisen as a platform for studies of stochastic effects and quantum thermodynamics [71, 72]. Such systems are often gate tunable, provide high quality data across a wide range of bandwidths and allow for the study of both classical and quantum fluctuations. Several recent works have utilized quantum dots and single electron transistors tuned between charge states in order to achieve the bistability necessary to perform these experiments [73, 74].

As has been discussed in the previous two chapters, Josephson junctions subject to an RF radiation demonstrate an inverse AC Josephson effect: the phase difference across a junction locks to the external frequency [35]. As a result, the phase steadily ramps with time, changing by n periods per RF cycle. The $I-V$ curves of the junction show "Shapiro steps" of quantized voltage, $V = \frac{n\hbar\omega}{2e}$ [36]. The exact mechanisms and stability of the phase locking were investigated in detail in the 80's, with an emphasis on chaotic dynamics [37]. The extremely precise voltage quantization of the steps is presently utilized in primary voltage standards [75].

In this chapter, we study stochastic switching between these phase locked dynamical states in a gate-tunable graphene Josephson junction. Stochastic switching between Shapiro steps has recently been observed in this system, with switching times exceeding the time scale of the dynamics by many orders of magnitude [49]. A slight change of the RF amplitude changes the switching time over an exponential range, from milliseconds to hours. The tunability and degree of control enabled by the Josephson junctions make them particularly appealing to study the switching dynamics in a driven-dissipative system.

4.2 Bistability of the Zero Crossing Step

The previous chapter focused on a pattern of Shapiro steps which are rather different from the conventional Bessel function behavior [19]. Notably, at some intermediate RF power both $n = +1$ and $n = -1$ are stable solutions at zero current, while $n = 0$ is not, resulting in "zero-crossing steps" in the $I - V$ curves [37, 49, 53]. In the tilted washboard picture commonly used to describe Josephson junctions, zero current corresponds to zero average tilt of the the washboard. The $n = \pm 1$ states correspond to the "phase particle" ratcheting one period per RF cycle either forward or backward along the washboard, therefore representing a peculiar example of broken time-reversal symmetry in a driven-dissipative system. Over the course of many drive cycles, rare fluctuations knock the phase particle so that it switches the direction of motion. We find that the temperature dependence of this switching lifetime shows a striking non-monotonicity and a reduction of the quantized voltage, which necessitates non-trivial phase space dynamics at long time scales.

In this chapter, we study the same junctions formed from graphene encapsulated in hBN. The superconducting contacts are made from MoRe alloy ($T_C \approx 10K$). Such junctions are gate tunable and mediate supercurrent via Andreev bound states [19].

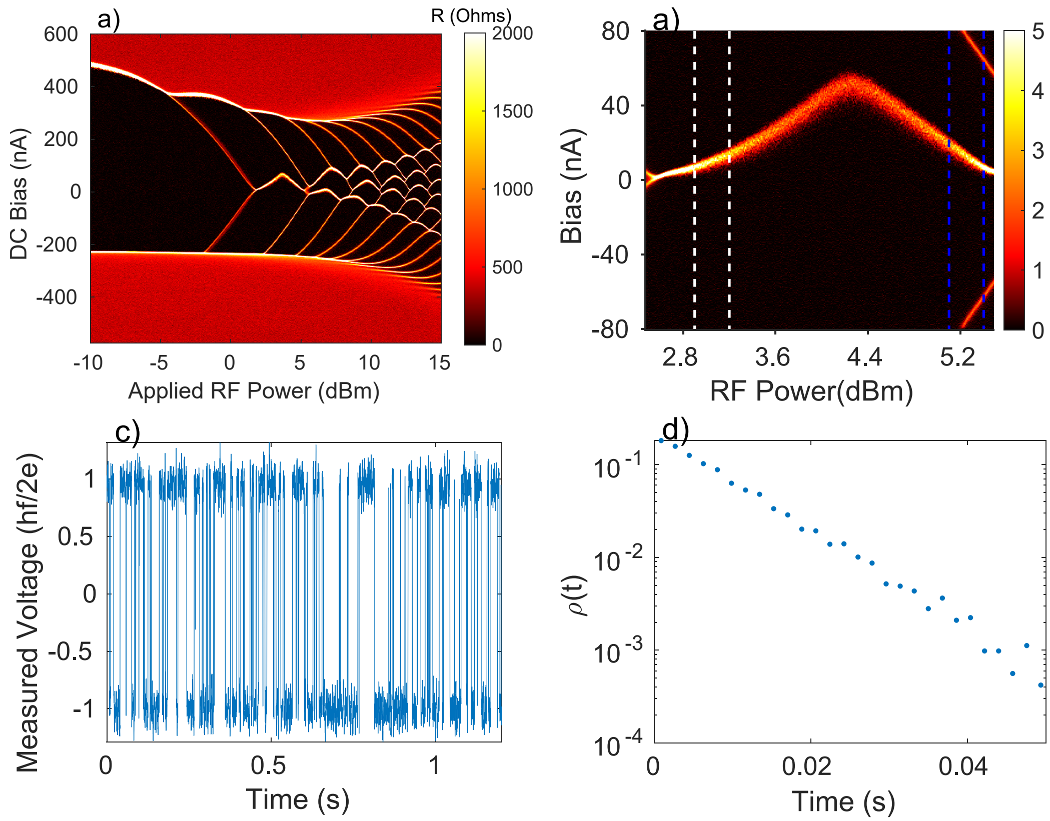

FIGURE 4.1: a) A standard RF power vs DC Bias current map of the differential resistance for these devices. Bridge regions highlight the transitions between Shapiro steps. b) The transition between the +1 and -1 Shapiro steps of the device studied, extracted by numerically differentiating several averaged DC sweeps. At 0 DC bias, within the region between the dashed white lines, stochastic switching between the two voltages was observed. c) A sample of the output voltage measured over a small interval of time. The average time between switching events was extracted from these and similar traces, and care was taken to operate in the regime where the distribution of measured voltages remained bimodal. d) The probability distribution of switching times, taken from the full two minute trace corresponding to (a)

However we believe the physics presented in this work does not depend on the microscopic properties of the sample and could be realized in other types of Josephson junctions. The sample is measured in a dilution refrigerator with a microwave antenna placed close to the sample for AC biasing. For all Figures except for Figure 4.4, a 5 GHz microwave signal is applied to the sample.

In Figure 4.1a, we reproduce the map of differential resistance vs bias and microwave power[53]. The dark regions correspond to Shapiro steps, where dV/dI vanishes. The map is measured by sweeping bias I_{DC} from negative to positive. The hysteresis in switching between the plateaus results in the pronounced top-bottom asymmetry of the map, noticeable as arching of the transition boundaries. Sweeping the current bias in the opposite direction would flip this map and that of Figure 1b about the horizontal axis.

Figure 4.1b shows a zoom-in map of the region in which the system switches between the $n = -1$ and $+1$ steps. To obtain this map, multiple $I - V$ curves are measured by sweeping the bias I_{DC}; these curves are then averaged and numerically differentiated. Therefore, the bright band of high dV/dI in the middle of the map corresponds to the average value of the switching current. Furthermore, the cross-section of the band represents the histogram of the switching currents.

For applied RF powers in the middle of Figure 4.1b, the $n = \pm 1$ states at $I_{DC} = 0$ could persist for hours. The lifetimes are much shorter at the edges of the region, allowing us to observe multiple transitions between the quantized steps while holding all control parameters constant. The primary region studied in this paper is just above the first bifurcation point, $P_{RF} \approx 2.6$ dBm, at which the $n = 0$ state first becomes unstable and $n = \pm 1$ states are observed. The studied range is marked by the dashed white lines in Figure 4.1b.

In Figure 4.1c, we plot a portion of a typical time trace measured at zero bias and $P_{RF} = 2.9$ dB. The voltage stochastically switches between the two plateaus with an average time of $\tau_0 \equiv \langle \tau \rangle \approx 10$ ms. The probability for a step to last a given time $\rho(\tau)$, as observed over the full time trace, is plotted in Figure 1d, demonstrating a clear exponential dependence with a slope of $\log(\rho) = 1/\langle \tau \rangle$ as expected for uncorrelated random processes.

Despite the fact that the two states of the system are dynamical in nature, it remains possible to consider this as a double well problem in an effective "quasipotential" [37, 76, 77]. This double well potential can be tuned with DC bias which can be observed in Figure 4.2a. At zero bias, the quasipotential double well is very close to symmetric, with the lifetime of each state lasting an equal length of time. By applying a small bias, on the order of 1 nA, it is possible to break the symmetry, shifting the imbalance in favor of one of the two states. Both times follow a clear exponential dependence $\log(\tau_\pm/\tau_0) = \pm\alpha I$, consistent with bias linearly increasing the activation gap. As a result, the product $\tau_+ \times \tau_-$ remains nearly constant as a function of bias.

4.3 Nonmonotonic Temperature Dependence of the Switching Rate

While all the features are so far consistent with a standard double well potential problem, the temperature dependence of τ is surprisingly not. This is shown in Figure 4.2b for temperatures form 100 mK to 400 mK and for a range of powers identified in Figure 4.1b. Considering first the power range $P_{RF} > 3.1$ dBm, τ_0 behaves as might be expected: it increases upon decreasing T and moving away from the bifurcation point, qualitatively consistent with thermal activation. However, for lower powers, $P_{RF} < 3.1$ dBm, τ_0 develops a peculiar non-monotonic behavior, where it *increases* at higher temperatures.

We have excluded possible trivial explanations for the observed effect. First, we measured voltages traces remain distinctly bimodal with two well-defined voltage states throughout the full temperature range. Second, Figure 4.3 shows data measured just before the second bifurcation point (located at $P = 5.1$ dBm). The $\tau_0(T)$ curves (supplemental material) show a qualitatively similar behavior to Figure 4.2a. Namely the non-monotonicity moves to lower temperatures the closer we move to the bifurcation point, which here corresponds to *higher applied RF powers.* We believe this excludes the possibility that non-monotonicity of $\tau_0(T)$ arises from a change of the system parameters with temperature. For example, a gradual reduction of

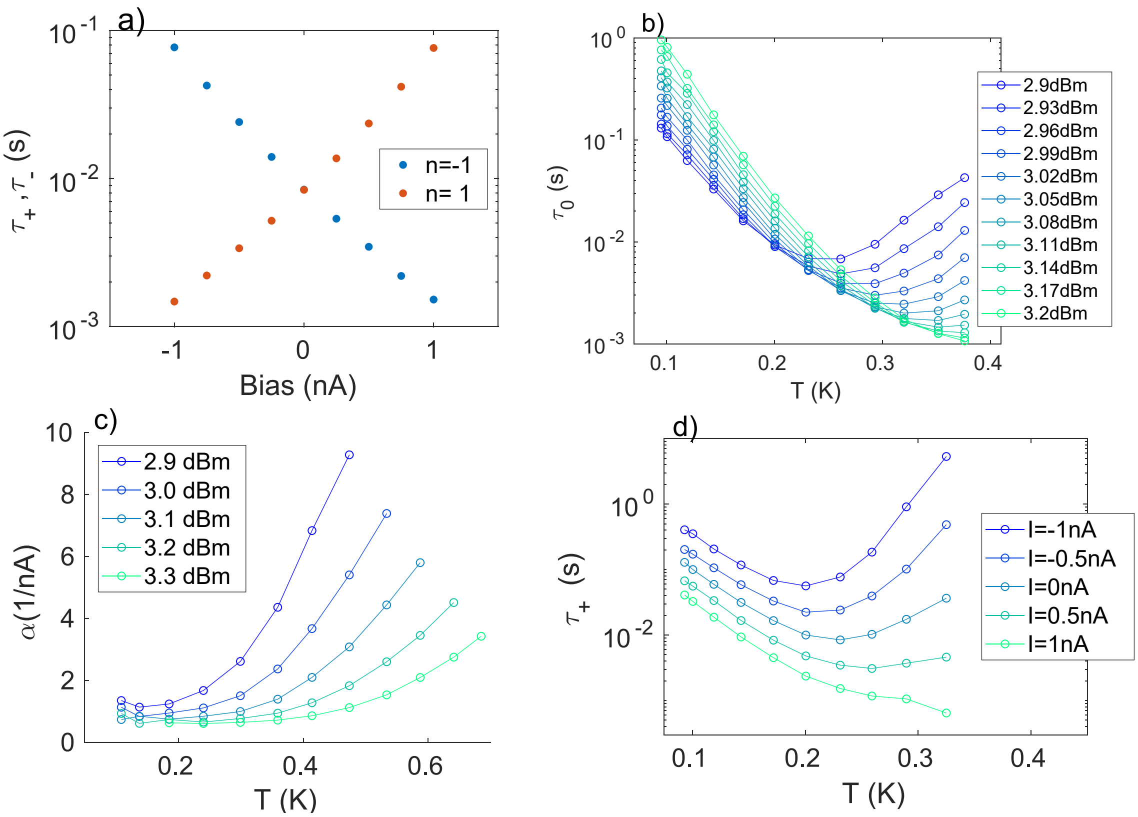

FIGURE 4.2: a) Switching times from $n = -1$ to $n = +1$ (τ_+)and in the reverse direction(τ_-). The balance between the two states is tunable by application of a small current bias. b) Dependence of τ_0 on temperature at several fixed P_{RF}. While the higher power show the expected steady decrease of lifetime with temperature, $\tau_0(T)$ is non-monotonic for lower temperatures. It is important that the raw voltage traces show two well defined voltage states for all temperatures and powers shown. c) α, the slope of $\log(\tau_\pm/\tau_0)$ vs. I (see Figure 1d) plotted as a function of temperature for several applied powers. While at low temperatures the values of α are similar, elevated temperatures show a rapid increase of α, particularly at lower powers. d) Temperature dependence of τ_- at several values of bias I. Note that in the low temperature regime, where τ_0 decreases with temperature, the $\tau_-(T)$ curves are parallel indicating a roughly constant α. The curves start to diverge at higher temperatures, where τ_0 increases with temperature and α is no longer a constant.

I_C would cause the non-monotonicity to arise at lower powers for both bifurcation points. We return back to the surprisingly non-monotonic $\tau_0(T)$ curves later in the chapter.

We next explore the combined effect of bias current and temperature on τ_0. In Figure 4.2c, we plot the dependence of the slope $\alpha = \frac{d \ln \tau_+}{dI}$ on temperature at several values of P_{RF}. While at low temperatures α saturates at roughly the same level for different P_{RF}, at higher temperatures α rapidly increases. This result is similarly unexpected, as the picture of a particle in a bistable potential tilted by current would predicts an activation behavior of α. We note that for a given microwave power, α eventually begins to *increase*, which happens at temperatures just below the onset of non-monotonic behavior of τ_0.

The interplay between $\tau(T)$ and $\alpha(T)$ is best seen in Figure 4.2d, which plots τ_+ vs. T at $P_{RF} = 2.9$ dBm for five values of bias. The middle curve corresponds to zero bias, at which $\tau_+ = \tau_0$. At low T, where τ_0 decreases with T, all curves are roughly parallel to each other (on a log scale), indicating a constant α. However, at high temperatures they start to diverge, which indicates that α is no longer saturated; this occurs just before τ_0 starts to grow with T.

It has been shown through both analytical studies and numerical simulations[37], that the transition rate between the two distinct steady state solutions in the traditional RCSJ model is expected to follow an activation temperature dependence. This effective model can essentially be reverse engineered, as the two dynamical states will be connected by a single most probable path, which can then be mapped to a saddle point of energy E_A in the classic double well potential picture. Clearly, the non-monotonic $\tau_0(T)$ dependence cannot be explained by such activation.

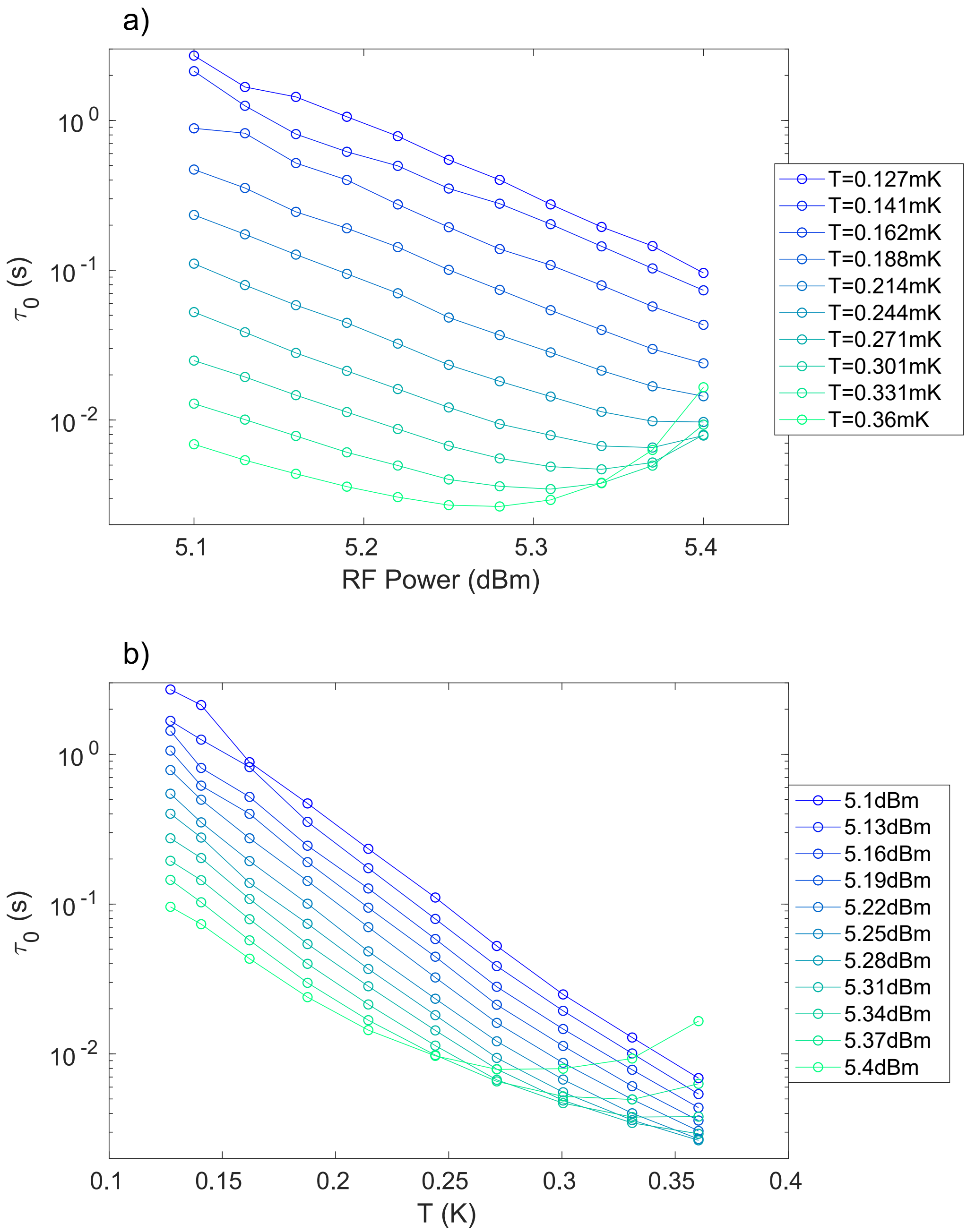

FIGURE 4.3: The second bifurcation point measured around 5.1 to 5.4 dBm. 4.3b is analogous to 4.2b, but shows that nonmonotonicity first sets in for higher powers, rather than lower powers, which allows us to exclude effects related to shifting parameters. 4.3a plots the same data set with the axes reversed.

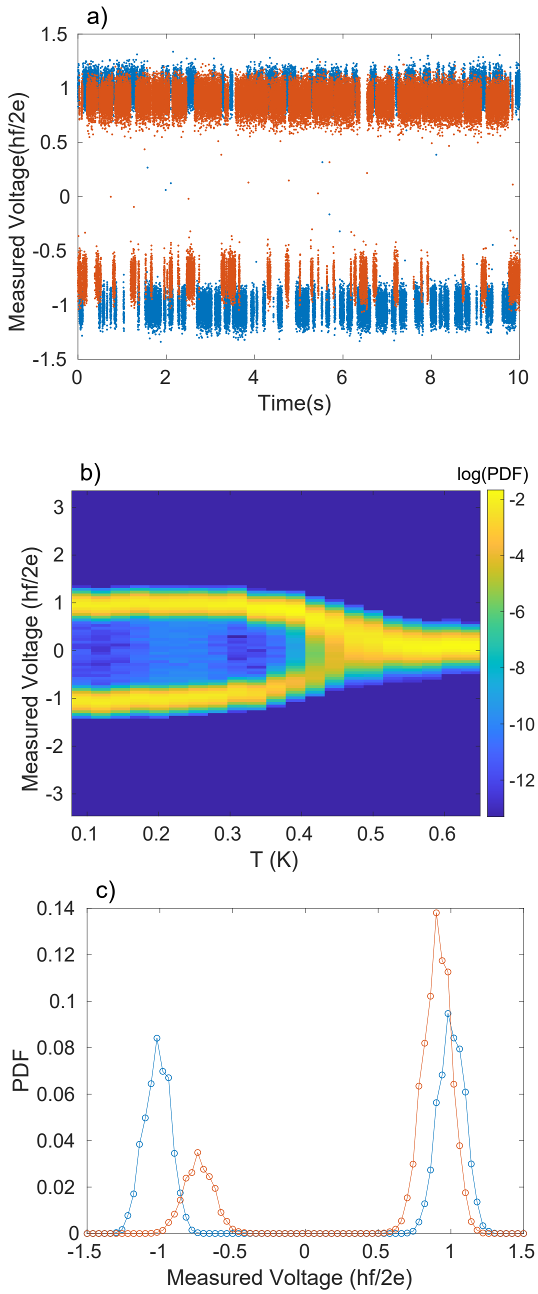

FIGURE 4.4: a) Time traces measured at $P_{RF} = 2.9$ dBm and temperatures of 90 mK (blue) and 380 mK (orange). The 380 mK trace clearly shows the loss of voltage discretization. b) The probability distribution of measured voltages as a function of temperature. High probability shown in yellow can be seen smoothly merging from two peaks at $\pm\frac{hf}{2e}$ into one peak at $V = 0$. c) Two individual histograms from 100 mK (blue) and 380 mK (orange).

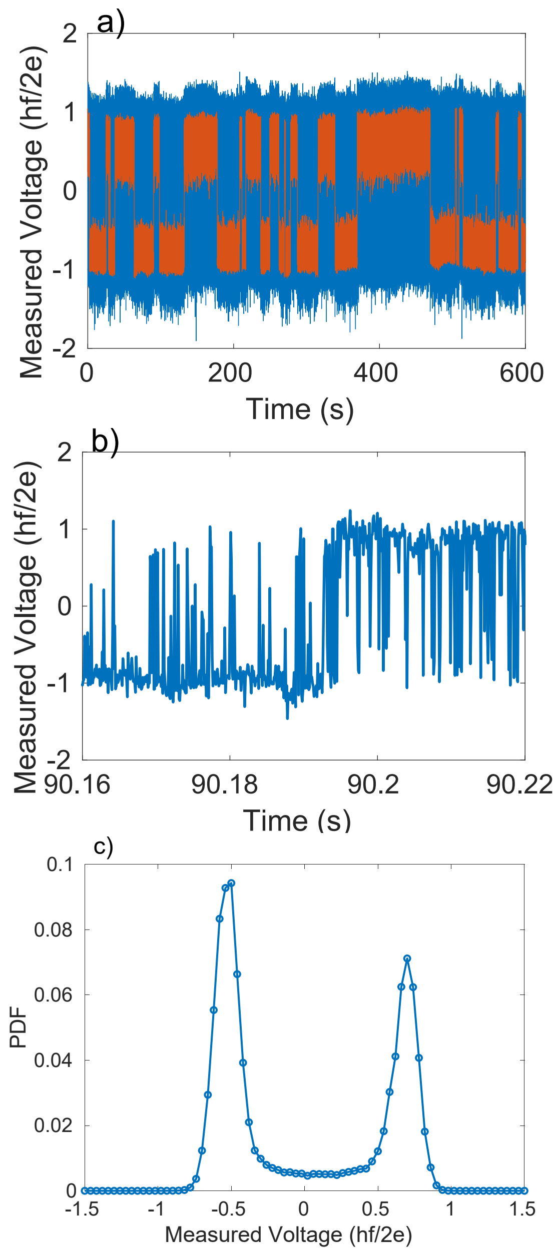

FIGURE 4.5: a) Traces of the measured voltage as a function of time. Blue shows the raw signal, which seems to not show bistable behavior. Orange shows the same trace with higher frequencies filtered out, indicating clear bistability. b) A small cut of the same traces, showing that while orange remains discretized, the raw signal shows many very short jump between the two steps. c) histogram of the measured voltage over the course of 10 minutes. While the data is clearly bimodal, there is also significant data in the region between the peaks.

4.4 Non-Markovian Switching

Inspection of the measured voltage traces in the non-monotonic regime reveals that while the voltage still switches between positive and negative steps, their values have become significantly reduced from $\pm\frac{\hbar\omega}{2e}$. One such trace, as well as a low temperature trace, are presented in Figure 4.3a for comparison. Here, the temperatures are selected such that the average switching times are comparable. Figure 4.3b shows the corresponding histogram of the measured voltages, which clearly demonstrates that at high temperature the average voltage corresponding the $n = \pm 1$ states is reduced.

The map in Figure 4.4c is made of the voltage histograms similar to panel (b) taken at different temperatures. The resulting "pitchfork" feature is non-trivial. As the thermal noise is increased, the system should switch faster. Eventually, when the switching rate exceeds the measurement bandwidth, an averaged voltage should be observed [78]. In our case this would correspond to the appearance of a broad peak centered at zero, which would grow while the peaks at $n = \pm 1$ shrink. Instead, we observe that the two peaks are shifting towards each other, before eventually merging. We argue below that the $n = \pm 1$ states still survive, but the system rapidly spikes from e.g. -1 to $+1$, before returning back to -1. If these spikes are too fast to be experimentally resolved, or if there are similar spikes attributed to wandering trajectories in the phase space [79, 80], the average voltage of both states would appear to be reduced.

To illustrate this behavior, in Figure 4.5a we show a 600 second time trace (blue) measured on a second device under a 5.2 GHz RF drive. The data demonstrates very rapid switching at a rate of at least $1/\tau \geqslant 200$ Hz. Surprisingly, by numerically smoothing the signal to remove the high frequency component, we recover bistable behavior with a very slow switching between two well-defined but non-discretized states (red curve). Figure 4.5b plots a 30 ms segment of the raw trace right around one of the points at which the averaged signal switches between the $n = -1$ and $+1$ states. It is clear that there are two regions with different averaged behavior: on the left, the system mostly stays around -1, while on the right if mostly stays close to $+1$. In both cases, there are many spikes reaching to the opposite state, which rapidly return back. This indicates that while the smoothed data in 4.5a may be Markovian, the originally rapidly switching data is certainly not. Instead, the system has memory: the switching probability depends on how long the system spent in a prior state.

We believe this memory effect arises because of additional poles in the Bode plot of our measurement circuit. Physically, the capacitance of the cryogenic RC filter is charged by the DC voltage produced via the inverse AC Josephson effect. When the system attempts to switch between dynamical states, e.g. from -1 to $+1$, the charged capacitor discharges through the junction, biasing it back to the original -1 state. At low temperature, when the dynamics are slow, this current will typically decay before the system switches back to the original state. But at higher temperatures, the system has a higher probability to return from $+1$ back to -1 while the capacitor has not yet discharged. The additional RC stage therefore stabilizes both ± 1 states, leading to the highly correlated switching (spikes) observed in Figure 4.5b. This effect may be viewed as a form of noise enhanced metasability [81], although the specific model, and the enhancement in a dynamical bistability are both novel.

4.5 Toy Models and Numerical Simulations

To quantitatively verify this picture, we have performed simple simulation with qualitatively reproduces the observed behaviors, including the correlated spikes of Figure 4.5 and the original non-monotonic temperature dependence of Figure 4.2.

For a toy model, we consider a triple well potential, with minimas corresponding

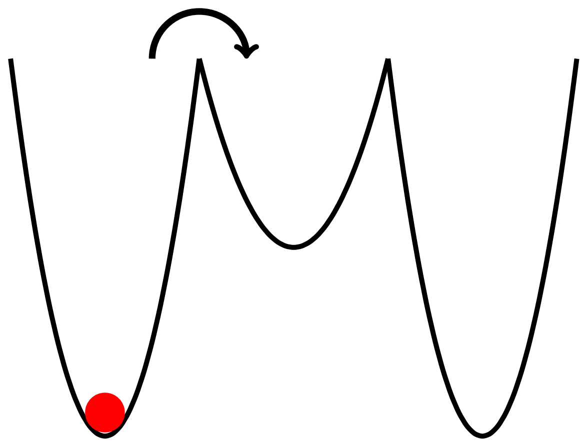

FIGURE 4.6: Generic symmetric triple well potential forming the basis of our toy model

to the quasipotential of $n = -1, 0, +1$. We assume that the particle begins in the $n = -1$ minima and that we want to find first passage time to the $n = +1$ minima. Purely activational behavior will simply result in multiplying the two escape rates. This effect is then monotonic with time. A generic schematic of this potential is shown in Figure 4.6. It is worth noting that even if the potential is asymmetric, the activational behavior remains.

To incorporate the effect of the external circuitry, we consider the simplest possible time dependence of the escape rates. For escape rates from the $n = 0$ minima to $n = -1$ ($n = +1$) we assign the name Γ_- (Γ_+). Initially we assume $\Gamma_- >> \Gamma_+$. However, after some time t_0, we assume all capacitances have fully discharged. In the absence of a DC bias, this implies $\Gamma_- = \Gamma_+$, so after t_0 this leads to an equal probability to go to either other well. To simplify matters, we assume that after returning to $n = -1$ the process starts over. This neglects certain correlated switching events, but it is a reasonable approximation if $\Gamma_{-1->0} << 1/t_0$. This assumption leads to a geometric series, giving the total first passage time

$$\langle \tau_{-1\to+1} \rangle = \tau_A \frac{\Gamma_+ + \Gamma_-}{\Gamma_+ + (\Gamma_- - \Gamma_+)e^{-t_0(\Gamma_+ + \Gamma_-)}/2} \tag{4.1}$$

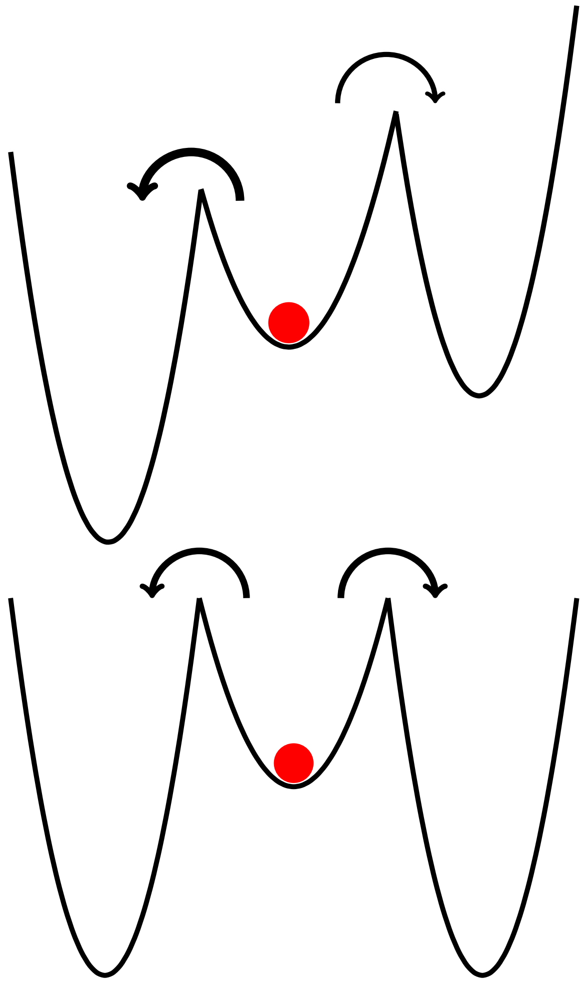

FIGURE 4.7: Two states of the hysteretic toy model. After jumping from the left well to the middle well, the system resembles the top figure, where it is much more likely to return to the previous state than to the opposite time. After some characteristic time t_0, external capacitors discharge, and the system returns to a symmetric figure as shown in the bottom diagram.

where τ_A is the mean escape time from $n = -1$ to $n = 0$ and all rates correspond to the constant values before discharge. While this toy model does have a substantial number of free parameters, it can easily be numerically solved. Such curves are shown in Figure 4.8, but it is perhaps more helpful to consider Figure 4.7 and attempt to develop some intuition.

At very low temperatures both Γ_{-1}, Γ_{+1} are much smaller than $1/t_0$, so our model is just equivalent to the standard activational model. However, as temperature in-

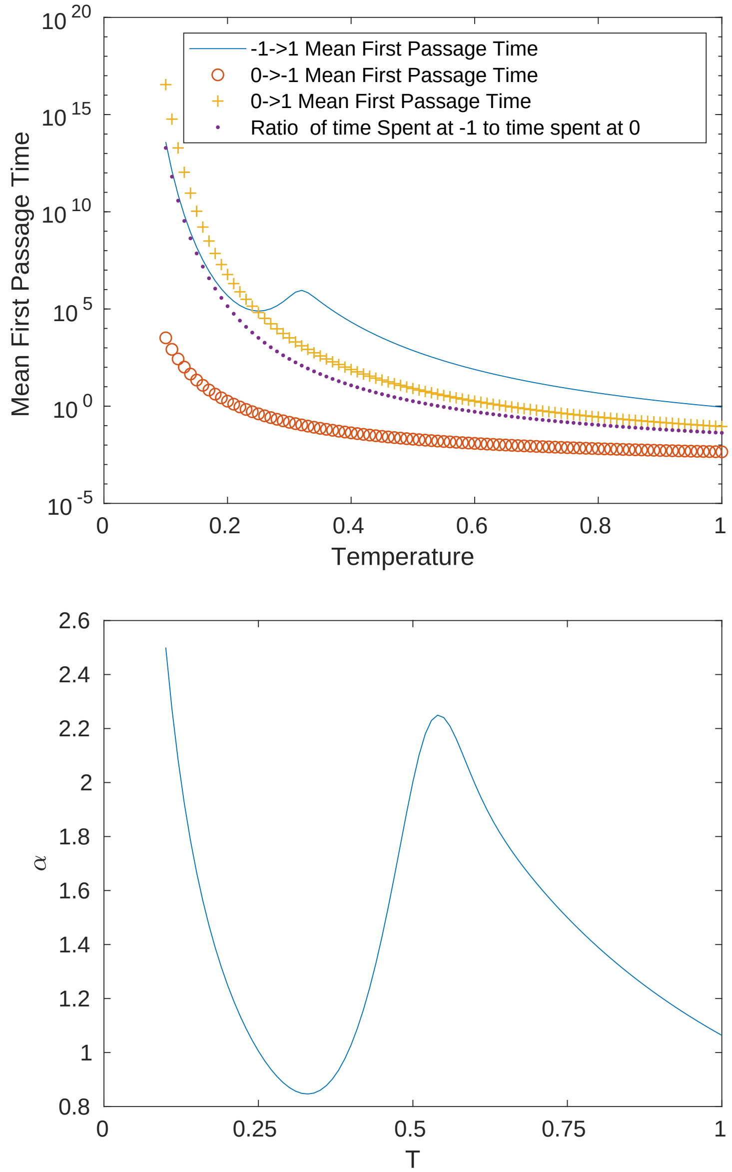

FIGURE 4.8: Toy model results. The top figure shows that the total first passage time is non-monotonic, even though all of the transitions are individually activational. Bottom plots α, the bias sensitivity, as a function of temperature, showing that the bias senstivity is also non-monotonic.

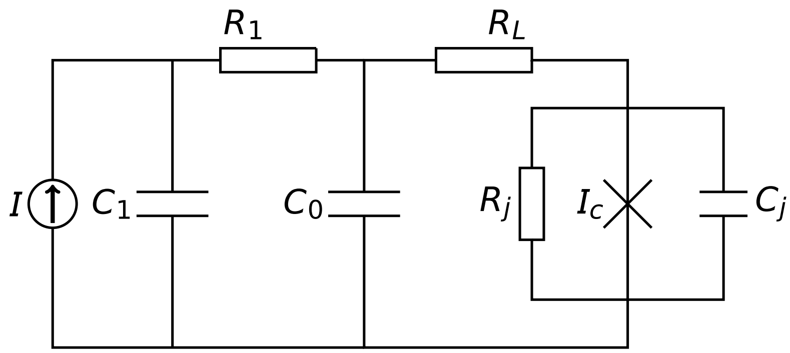

FIGURE 4.9: Fully extended RCSJ model which is simulated. Simulations were performed with physically reasonable values. In particular, we used $R_1 = 1500\Omega$,$R_1 = 50\Omega$, $R_j = 300\Omega$, $C_1 = 1\text{nF}$,$C_0 = 1\text{pF}$,$C_j = 0\text{nF}$

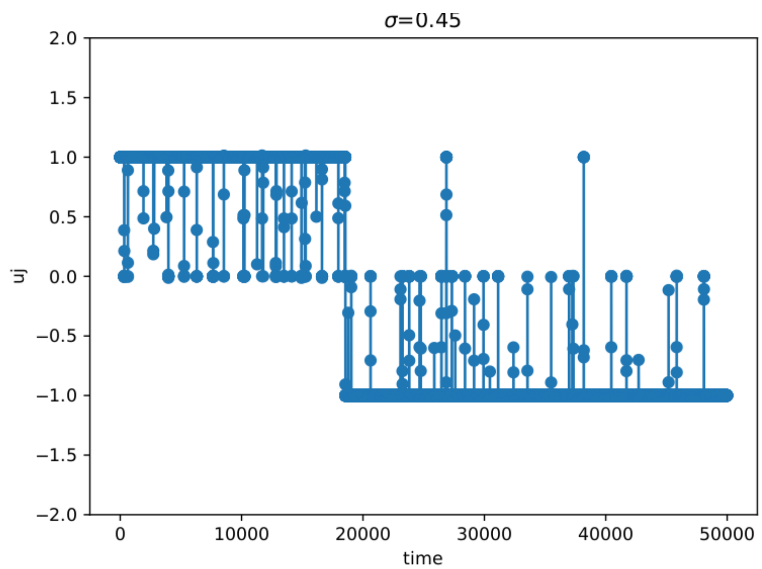

FIGURE 4.10: A segment of the voltage as a function of time for the full simulation, showing strong similarity to the non-Markovian behavior of 4.5b.

creases, we reach a regime where $\Gamma_{-1} \geqslant 1/t_0$. Even though the switching rate from $n = -1$ to $n = 0$ is still activational and thus increasing with temperature, the probability to make the jump from $n = 0$ to $n = 1$ is starting to decrease in temperature, giving rise to nonmonotonic first passage times.

Additionally, we perform full numerical simulations for an RCSJ model connected to two external filters, as shown in Figure 4.9. The equations corresponding to this

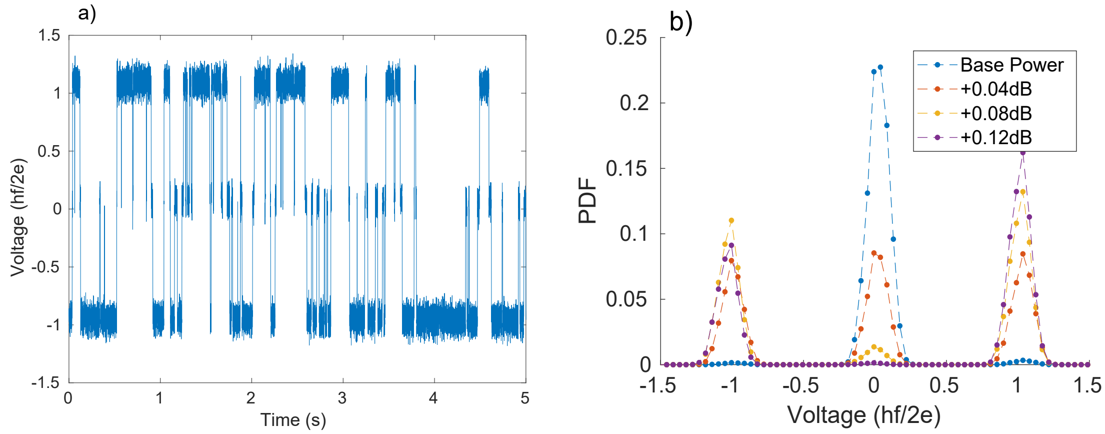

FIGURE 4.11: Markovian tristable behavior. a) corresponds to a single 5s time trace, while b) corresponds to the probability of measured voltages over a small range of power.

model are

$$
\begin{aligned}
I &= I_{bias} + I_{RF}\sin\omega t + I_N(t) \\
&= C_1\frac{dV_2}{dt} + C_0\frac{dV_1}{dt} + I_C\sin\phi + \frac{\hbar}{2eR_j}\frac{d\phi}{dt} + \frac{\hbar C_j}{2e}\frac{d^2\phi}{dt^2} \\
V_1 &= \frac{\hbar}{2e}\frac{d\phi}{dt} + R_L\left(I_C\sin\phi + \frac{\hbar}{2eR_j}\frac{d\phi}{dt} + \frac{\hbar C_j}{2e}\frac{d^2\phi}{dt^2}\right) \\
V_2 &= \frac{\hbar}{2e}\frac{d\phi}{dt} + (R_L + R_1)\left(I_C\sin\phi + \frac{\hbar}{2eR_j}\frac{d\phi}{dt} + \frac{\hbar C_j}{2e}\frac{d^2\phi}{dt^2}\right) + R_1C_0\frac{dV_1}{dt}
\end{aligned}
\tag{4.2}
$$

Well the separation of time scales make it challenging to observe the nonmonotonic dependence of the first passage time, it is possible to observe highly correlated non-Markovian switching, which we believe is the central ingredient in the non-monotonic dependence of the first passage time. Such highly correlated switching can be observed in Figure 4.9

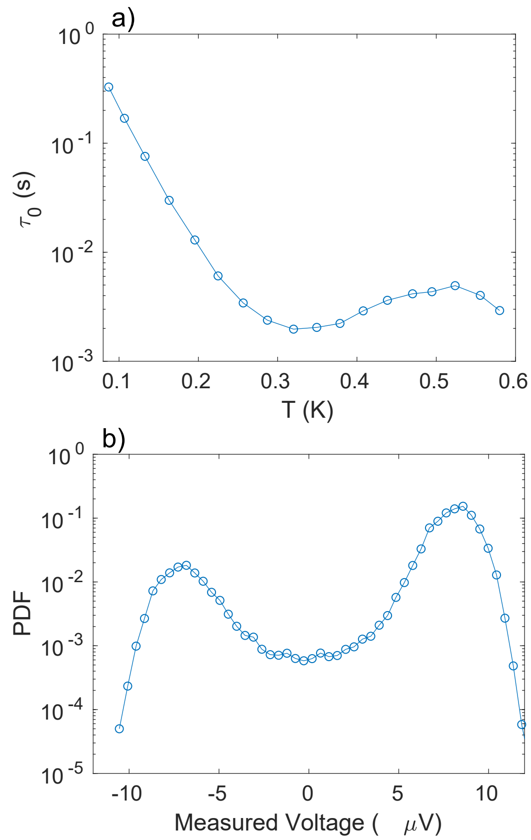

FIGURE 4.12: Data measured for a wide temperature range at 3.1 dBm applied power. a) shows a small downturn in the lifetime past 0.5K. b) depicts the histogram of measured voltages for the highest tempature datapoint, showing still fairly cleanly bimodal data, noting the log scale.

4.6 Further Effects and Considerations

For our system, the quasipotential wells are a function of the drive frequency[37]. One interesting consequence of this which we observe is that by applying a 6.42 GHz drive frequency to our first device, we measure Markovian tristable behavior at base temperature. As was mentioned in an earlier section, we observe no direct jumps between $n = +1$ and $n = -1$, but only jumps through $n = 0$. However, for a series of jumps $n_{k-1} \rightarrow n_k = 0 \rightarrow n_{k+1}$ we observe no correlation between n_{k-1} and n_{k+1}. A portion of this data is plotted in Figure 4.11.

A natural question which has not been addressed yet is what happens in the high temperature limit. As can be seen in Figure 4.4b, eventually the observed data is no longer bimodal. In general, long before this point it becomes challenging to analyze, due to the fact that a significant part of the data lies between the bimodal peaks. However, for one specific range of parameters, it was possible to observe that the data was bistablity for a wide enough temperature range to observe a high temperature downturn in the lifetime, which is shown in Figure 4.12.

One important question which remains open is the conceptual importance of the $n = 0$ state in explaining the non-monotonic $\tau_0(T)$. Numerical simulations of the full differential equation typically show no direct transitions between the $+1$ and -1 states; instead the system transitions by passing through $n = 0$. Experimentally, whenever the 0 state is visible within our time resolution, the system tends to switch between -1 and $+1$ via that state, as is discussed in the next section. Therefore, the triple well potential is both expected in our system and makes it easier to account for the nonmonotonicity of $\tau_0(T)$. However, the possibility remains that the memory effects could cause non-monotonic temperature behavior in a double well even without the metastable $n = 0$ state.

4.7 Conclusions and Future Work

To summarize, we have studied switching in an AC driven Josephson junction, which demonstrates surprisingly complex dynamical behavior. We focus on the "zero-crossing steps", in which at zero bias the zero voltage state is not stable, and the system spontaneously develops a quantized voltage of $\pm V = +\hbar\omega/2e$. The switching time between these states vary from msec to ksec. We found unexpected non-monotonic temperature dependence of the switching time, which reaches a minimum value at an intermediate temperature which is a function of the RF drive. We attribute this behavior effects of the measurement system, which allows for the circuit to have signifcant memory. These effect are combined with the complex structure of the phase space, in particular with the presence of a metastable zero-voltage state.

The type of samples as studied here provide a flexible and highly tunable platform to probe the unexplored aspects of a quantum driven-dissipative dynamics. The nature of the most probable escape path, both in the Markovian and non-Markovian limits, is still an open question for this system. While we believe that the electron temperature in our system is too high for the phase particle to behave quantum mechanically [52], it may be possible to engineer a device with higher heat capacity and thermal conductivity to the bath which undergoes such a dynamical bistability in the macroscopic quantum tunneling regime [82], opening doors to many interesting experiments on driven-dissipative quantum dynamics.

5

Theory 2: Quantum Hall and Noise

5.1 Quantum Hall

5.1.1 Basics of the Quantum Hall Effect

The classical Hall effect is a well established and canonical piece of physics. We begin with a conducting sheet of material, with a voltage applied such that current flows through the sheet. When a perpendicular magnetic field is applied, the Lorentz force $\vec{F} = q\vec{V} \times \vec{B}$ acts on the charge carriers, causing charge to build up on one side of the sheet and a voltage to develop perpendicular to the direction of the current.

Even within this classical framework, it is easy to see that the Hall effect can show strange behavior in the high field, clean sample limit. The cyclotron radius of a particle in in a perpindicular magnetic field is $r = \frac{mv}{qB}$. For electrons of mass m_e, Fermi velocity 1e6 m/s and subject to a magnetic field of 10 T, the cyclotron radius is only $\approx$ 50 nm. In a realistic sized device, the electrons in the bulk of the material are now localized, and current is carried only by chiral skipping orbits along the edge of the device. This classical picture (Figure 5.1) does capture the basic idea of the quantum Hall effect, but more details require the quantum version. I have adapted

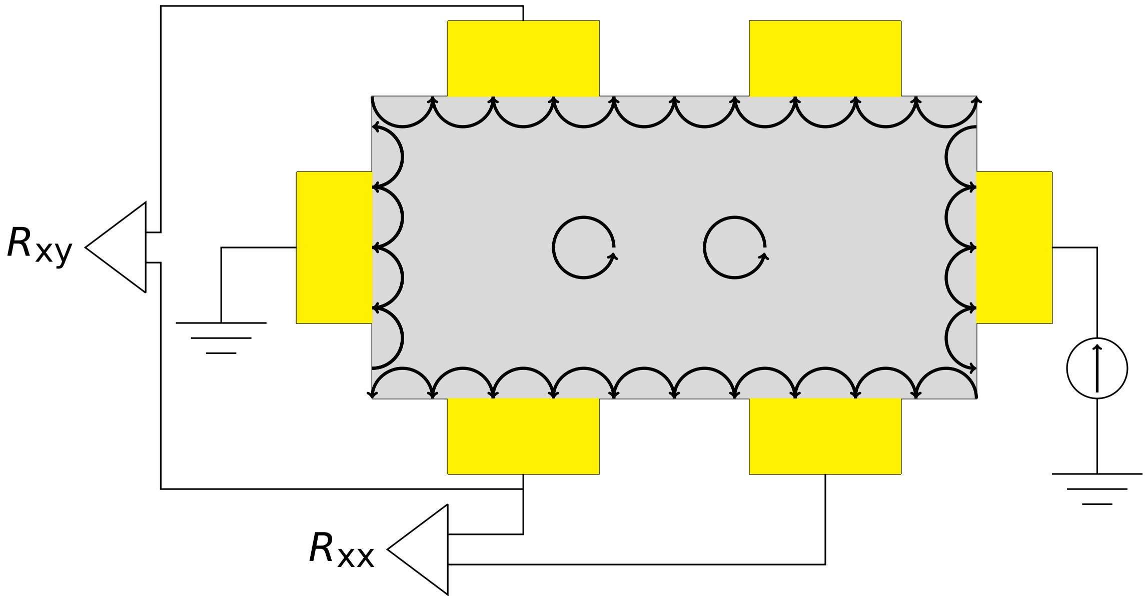

FIGURE 5.1: The classical hall effect, taken to an extreme limit. Only skipping orbits at the edge can transport charge between contacts, while the bulk is insulating. This is surprisingly consistent with a more rigorous formulation of the quantum Hall effect, although the quantized conductance and dissipationless transport at the edge are spectacular results which are not obvious from this picture.

the following from Tong[83].

We begin with the classic problem of Landau levels. If we want to consider our 2D conductor subject to a perpindicular magnetic field, the vector potential must be incorporated into the momentum of our Hamiltonian. For a magnetic field $\vec{B} = B\hat{z}$ it is easiest to proceed with the Landau gauge $\vec{A} = xB\hat{y}$. We now have the Hamiltonian

$$H = \frac{1}{2m}|\vec{p} - e\vec{A}| = \frac{1}{2m}|(p_y - exB)^2 + p_x^2| \tag{5.1}$$

which can be reparameterized in terms of the cyclotron frequency ω_c as

$$H = \frac{p_x^2}{2m} + \frac{1}{2}m\omega_c^2(x - \frac{\hbar k_y}{m\omega_c})^2 \tag{5.2}$$

where $\hbar k_y$ is the eigenvalue of p_y (we are able to parameterize this way as $[H, \hat{p}_y] = 0$).

This is just the Hamiltonian for a harmonic oscillator with a shift in x. Thus electrons are forced into states with energy $E_n = \hbar\omega_c(n+1/2)$. These states naturally have significant degeneracy because the energy is the same for different values of k_y. The sample dimensions cause k_y to be quantized in units of $\frac{2\pi}{L_y}$. Because the center of the oscillator must also lie within the sample we require $0 < \frac{\hbar k_y}{m\omega_c} < L_x$. As a result, the degeneracy of each Landau level is

$$\mathcal{N} = (L_x/l_b^2)/(2\pi/L_y) = \frac{L_x L_y}{2\pi l_b^2} = \frac{eBA}{2\pi\hbar} \tag{5.3}$$

where A is the area of the sample, and we have made use of a convenient length scale $l_b = \sqrt{\frac{\hbar}{eB}}$.

Having found the Landau levels and their degeneracy, we now turn to what happens on the edges of a real sample. If our 2DEG is rectangular, we can very naively describe the device as having a potential $V(x) = 0$ away from the edges and raising steeply at the boundaries. Assuming that this steep raise is smooth on the atomic scale, we can Taylor expand, keep just the first term and approximate $V(x) = \frac{\partial V}{\partial x}$ (or $V(x) = \frac{-\partial V}{\partial x}$ on the opposite edge).

For a single filled Landau level we can find that the current carried by the states is

$$I_y = -e\int \frac{dk}{2\pi} v_y(k) = \frac{e}{2\pi l_b^2}\int dx \frac{1}{eB}\frac{\partial V}{\partial x} = \frac{e^2}{h} V_H \tag{5.4}$$

where V_H is the Hall voltage. We have thus derived the quantized conductance of a single filled Landau level, and found that indeed this quantized conductance only arises from the edge current. It is easy to see that as more Landau levels are filled each contributes a quantum of conductance.

We have glossed over an interesting point. We have only derived quantized conductance for filled Landau levels, that is $\mathcal{N}$ is an integer. This enforces $B = \frac{h}{\mathcal{N}eA}$, otherwise there are partially filled Landau levels and no quantized conductance. But this clearly disagrees with experimental results which do observe quantized conduc-

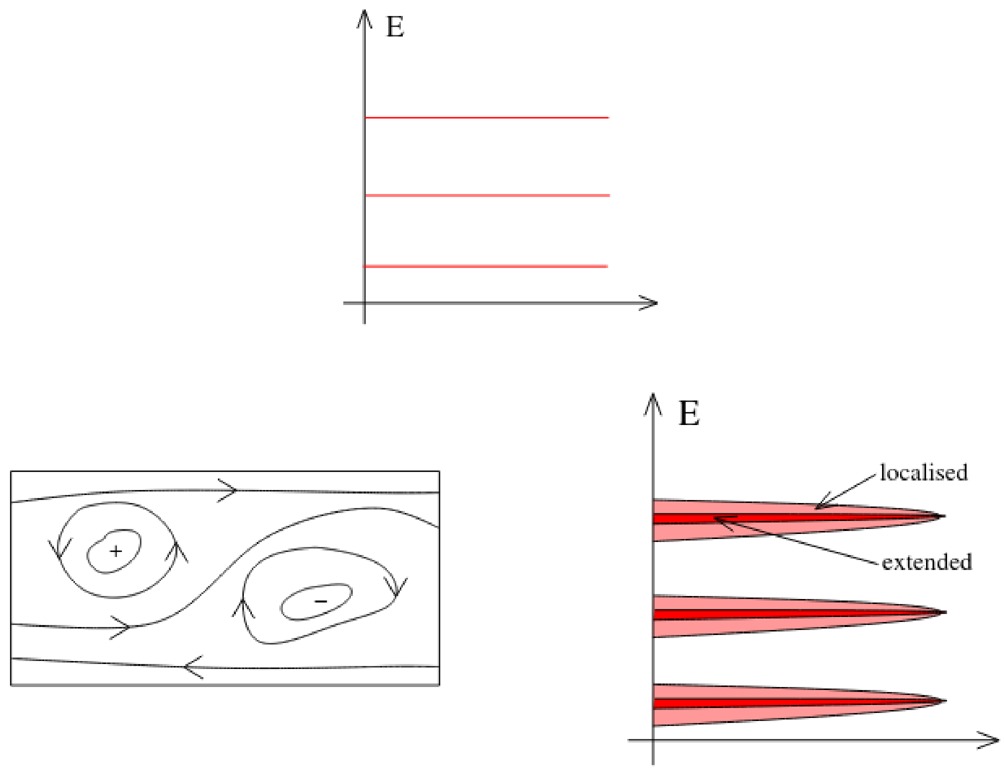

FIGURE 5.2: Top: Landau levels in the simplest form, perfectly degenerate with a large density of states. Bottom Left: the effect of disorder on the quantum Hall effect, where charged impurities create local equipotential lines, localizing charge. Bottom right: Landau levels are broadened by the disorder. Fortunately, the localized states are the most spread out, which leads to a range of doping for which conductance is quantized. Adapted from[83].

tance plateaus, so there must be a subtle point which can give rise to observable conductance plateaus.

Incredibly, disorder is to the rescue. While it is important that the strength of disorder is small relative to the Landau gap in order to observe the quantum Hall effect, disorder plays an important role in broadening the Landau levels and localizing a large number of states, particularly those at the edge of the broadened Landau level. Filling these states has no effect on the conductance, giving rise to the observed conductance quantization. Both the disorderless and finite disorder

Landau levels as well as a schematic figure of the effect of disorder on the edge states, is depicted in Figure 5.2.

5.1.2 The Quantum Hall Effect in Graphene

While we have discussed the generic features of the quantum Hall effect, graphene enjoys a number of unique quantum Hall features[84]. These particularly arise out of the valley degeneracy of graphene and the Dirac equation which governs electron behavior in graphene.

This time, we will derive Landau levels while paying attention to the microscopics of our device. For simplicity, we consider just the K valley. Further, this time we will use the Landau gauge $\vec{A} = -By\hat{x}$. Since our system has translational symmetry along the $\hat{x}$ direction, our solution will correspondingly form plane waves along the $\hat{x}$ direction, simplifying our derivation. For electrons in the K valley, the Hamiltonian is

$$H_k = \hbar v_f \begin{bmatrix} 0 & -\partial_x - i\partial_y \\ -\partial_x + i\partial_y & 0 \end{bmatrix} \tag{5.5}$$

where the spinor is for the two separate sublattices of graphene. Once again incorporating the vector potential into the momentum, and splitting the wavefunction in each sublattice into a planewave $\hat{x}$ component and an as of yet unsolved $\hat{y}$ component we find

$$\begin{aligned} H_k\Psi = \hbar v_f \begin{bmatrix} 0 & -\partial_x - i\partial_y - \frac{e}{h}yB \\ -\partial_x + i\partial_y - \frac{e}{h}yB & 0 \end{bmatrix} e^{iq_x x} \begin{bmatrix} A(y) \\ B(y) \end{bmatrix} \\ = Ee^{iq_x x} \begin{bmatrix} A(y) \\ B(y) \end{bmatrix} \end{aligned} \tag{5.6}$$

Evaluating yields two coupled equations which can be straightforwardly decoupled

$$\begin{cases} \left(q_x - \frac{y}{l_c^2} - \partial_y\right) B(y) = \frac{E}{\hbar v_F} A(y) \\ \left(q_x - \frac{y}{l_c^2} + \partial_y\right) A(y) = \frac{E}{\hbar v_F} B(y) \end{cases} \rightarrow \begin{bmatrix} \partial_y^2 + \frac{1}{l_c^4}\left(y - q_x l_c^2\right) \\ \partial_y^2 + \frac{1}{l_c^4}\left(y - q_x l_c^2\right) \end{bmatrix} \begin{matrix} A(y) = \left(\frac{E^2}{\hbar v_F} - \frac{1}{l_c^2}\right) A(y), \\ B(y) = \left(\frac{E^2}{\hbar v_F} + \frac{1}{l_c^2}\right) B(y) \end{matrix} \tag{5.7}$$

These new equations are once again harmonic oscillator equations, which we can solve to find

$E_A = \pm\sqrt{2e\hbar c^2 B\left(n_A + 1\right)}$ for $n_A = 0, 1, 2, \ldots$

$E_B = \pm\sqrt{2e\hbar c^2 B n_B}$ for $n_B = 0, 1, 2, \ldots$

Solving for the K' valley gives the same results, although the sublattices have the forms of their solution swapped. There are several interesting features to note. Most obviously, instead of finding $E \propto n$ we find $E \propto \sqrt{n}$. This is sometimes referred to as the relativistic quantum Hall effect, as it follows out of the linear dispersion of electrons in graphene[85].

Generically, the Landau levels in graphene are 4 fold degenerate, due to the spin and valley degeneracies. However, unlike in GaAs, graphene has Landau levels for $n = 0$. This valley is still 4 fold degnerate, but it pinned at E=0 and contains 2 electron levels and 2 hole levels, giving rise to the observed filling factors in graphene $\nu = 2, 6, 10, \ldots$ More profoundly, we can attribute this half filled Landau level to a Berry phase of π[86].

Higher quality devices can also exhibit symmetry breaking of the Landau level degeneracies, as long as the disorder broadening is small compared to the Zeeman gap and valley degeneracy energy breaking scale arising from electron-electron and electron-phonon interaction[87]. The quantum Hall effect is extremely rich, and there are many very interesting facets, such as the fractional quantum Hall effect and quantum Hall ferromagnets[88], which lie outside the scope of this dissertation.

5.2 Chiral Andreev Edge States

We have considered two ingredients that would be very interesting to combine: superconductivity, in particular Andreev reflection, and the quantum Hall effect. It is fairly easy to imagine that a chiral state could be Andreev reflected by a superconducting contact.

Combining these ingredients has only recently become experimentally possible. While GaAs quantum Hall samples have been available for decades, the difficulty of forming transparent contact to the 2DEG presents a serious obstacle. Further, the large magnetic fields required for the quantum Hall effect require a very high critical field superconductor. The combination of the developments of relatively high T_C sputtered alloys such as Molybdenum Rhenium and Niobium Titanium Nitride, as well as high quality hexagonal Boron Nitride encapsulated graphene[89] and Indium Arsenide 2DEGs[90] which make high quality contacts have opened great possibilities in this direction[91].

While the works cited above present different coupling mechanisms, here we are interested in a system where a quantum Hall edge bounces along a grounded superconducting contact. To elucidate what happens here, we consider a simple toy model. Suppose a zero energy electron is incident on the superconducting contact. When it enters the proximitized region, we can represent it as a linear combination of the two zero energy electron-hole modes

$$\begin{aligned} |\psi_1\rangle &= \alpha|e\rangle + \beta|h\rangle \\ |\psi_2\rangle &= \beta^*|e\rangle - \alpha^*|h\rangle \end{aligned} \tag{5.8}$$

As these two modes propagate along the interface, they will each acquire a different phase. Thus, at the end of the interface, we will have the state

$$
\begin{aligned}
|\phi\rangle &= \alpha^* e^{ik_1 L} |\psi_1\rangle + \beta e^{ik_2 L} |\psi_2\rangle \\
&= \left(|\alpha|^2 e^{ik_1 L} + |\beta|^2 e^{ik_2 L}\right) |e\rangle + \left(e^{ik_1 L} - e^{ik_2 L}\right) \alpha^* \beta |h\rangle
\end{aligned} \tag{5.9}
$$

where k_1, k_2 are the wavevectors of the two modes and L is the propagation length. Some inspection shows that the charge of $|\phi\rangle$ is

$$
q = e\left(P_e - P_h\right) = e\left(1 - 2P_h\right) = e\left(1 - 8|\alpha|^2|\beta|^2 \sin^2(\delta k L/2)\right) \tag{5.10}
$$

which thus oscillates with δk even for $|\alpha|^2 = |\beta|^2 = \frac{1}{2}$ This effect was recently was recently observed by Zhao et al[10] (Figure 5.3) and will be more fully detailed in Lingfei Zhao's dissertation. By working with an Landauer-Büttiker formalism, it can be seen that this conversion can be measured in the downstream voltage downstream of the grounded superconducting contact.

5.3 Noise in Mesoscopic Devices

While noise is generally undesirable when performing scientific measurements, the electrical fluctuations of a circuit can provide a great deal of information about the fundamental physics of the electron and energy transport of mesoscale devices.

5.3.1 Intuitive Approaches to Noise

Thermal Noise

The thermal noise, or Johnson-Nyquist noise, of a resistor is an equilibrium noise often associated with the Brownian motion of electrons in a resistive element. It is also a canonical example of the more general fluctuation dissipation theorem. This result can also be derived from the diffusive motion of electrons[92] (although the result is more generic) or by solving a Langevin equation for an RC circuit[93], but these derivations are omitted because they provide minimal insight without fully developing the formalism.

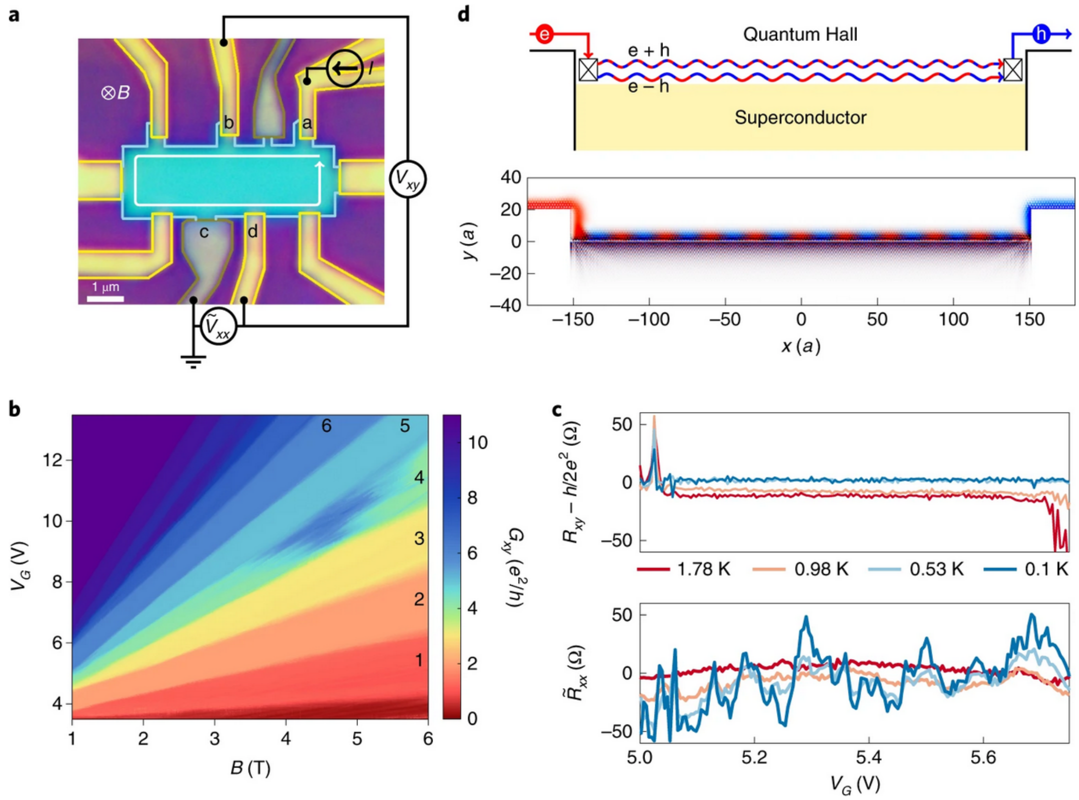

FIGURE 5.3: Chiral Andreev edge states. Top left shows a hall bar, with mostly normal contacts and two superconducting contacts, one of which is grounded. Top right shows schematically the electron being converted into $e \pm h$ modes, which acquire different phases, as well as a tight binding simulation indicating the electron and hole densities along a contact. The bottom pannels show that R_{xy} remains well quantized while the downstream voltage oscilates irregularly, giving both positive and negative values. Adapted from[10]

The central result is that a resistance R generates voltage fluctuations $\langle V^2 \rangle = 4k_B TR\Delta f$ where Δf is the bandwidth. This holds for both macroscopic and mesoscopic devices. This is particular valuable in cryogenic systems as a primary thermometer, because at temperatures below 1 K the electron and lattice temperatures can become substantially decoupled, decreasing the accuracy of conventional thermometry[94].

Classical Shot Noise

Classical shot noise was first considered in the context of vacuum tubes. We consider a vacuum tube which flows an average current $\langle I \rangle$. As electrons are discrete, we consider the simplest model where there is a uniform probability per unit time that an electron is emitted[95]. The distribution of average current measured at a time t should be Poisson distributed. This can be seen from the intuitive fact that

$$P_N(t+dt) = P_{N-1}(t)\frac{dt}{\tau} + P_N(t)\left(1 - \frac{dt}{\tau}\right) \tag{5.11}$$

where τ is the mean time between tunneling events. We can now see

$$\frac{d}{d(t/\tau)}\Pi_N = \Pi_{N-1} \tag{5.12}$$

where $\Pi_N \equiv P_N \exp(t/\tau)$. The solution by induction is clearly

$$\Pi_N = (t/\tau)^N \Pi_0/N! \rightarrow P_N(t) = \frac{\langle N \rangle^N}{N!} e^{-\langle N \rangle} \tag{5.13}$$

which is a Poisson distribution. We can now find that the mean square fluctuation of the current is

$$2e^2(\langle N^2 \rangle - \langle N \rangle^2)/t = 2e(\frac{e\langle N \rangle}{t}) = 2e\langle I \rangle \tag{5.14}$$

owing to the statistical property that the variance of a Poisson distribution is equal to its expectation. This form, with noise proportional to $2eI$ is quite generic, and it can apply equally well to a vacuum tube and a mesoscopic system (assuming Coulomb interaction is not critical). The closest analogy to the vacuum tube shot noise in mesoscopics is a tunnel junction, which gives incident electrons a low probability of tunneling across a barrier. One thing which we can immediately note is that the factor of e in the vacuum tube formula arises because this is the charge of the charge carrier in that system. But condensed matter systems can have charge carriers with different charges q, such as Cooper pairs[96] and the quasiparticles in the fractional quantum Hall regime[6, 7]. By making devices that exhibit shot noise in these systems, we can directly measure the quasiparticle charge, which is already an incredible result.

But this is not the only thing that shot noise probes. Lets consider a quantum point contact, which is a tunable beam splitter. At very low transmission probability, we expect very similar behavior to the tunnel junction. However, the adjustable transmission of a QPC allows us to hit interesting regimes, such as 50% transmission. Generically, systems which exhibit shot noise proportional to current, so we can characterize them by a Fano factor $F = \frac{S}{2qI}$.

Another major consideration is the use of cross-correlation techniques. Up until this point, we have only been considering voltage or current fluctuations as measured in a single contact. However, some times we may be interested in measuring the cross correlation $\langle I_1 I_2 \rangle$ where the subscripts refer to different contacts. For example, if QPC is positioned such that particles are either transmitted to contact 1 or reflected to contact 2, than $\langle I_1 I_2 \rangle$ can directly probe the Fermi or Bose statistics of the quasi-particles. For Fermions we will find $\langle I_1 I_2 \rangle < 0$ which is a consequence of the Pauli exclusion principle, while bosons will show $\langle I_1 I_2 \rangle > 0$. These effects are sometimes referred to as anti-bunching and bunching, respectively[95].

Other types of Fundamental Noise

The other commonly mentioned type of fundamental noise is $1/f$ noise or flicker noise[97]. This is a low frequency noise often associated with ensembles of various bistabilities like charge defects, which are stochastically jumping between occupied and unoccupied[98], although other more sophisticated models of $1/f$ noise exist and it remains an active area of study. These measurements can provide information

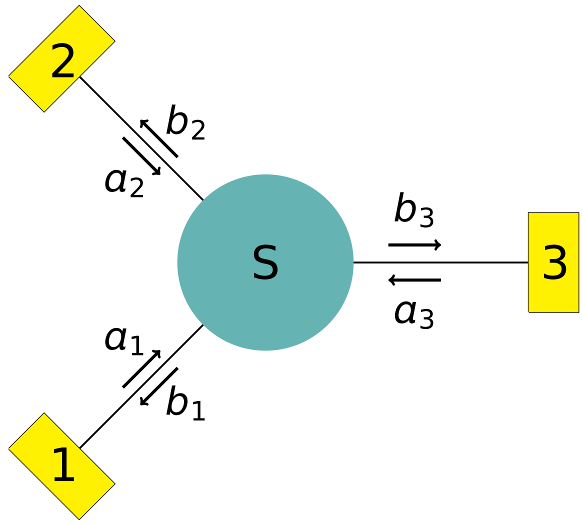

FIGURE 5.4: The scattering perspective of mesoscopic devices. Contacts numbered 1-3 send input modes a towards a central scattering region, which then emits output modes to the same contact. More complicated devices can generally be described by combining multiple scattering regions

about these flickering defects, but generally require a very different measurement setup to observe.

More recently, there has been interest in Delta-T noise [99] or thermal shot noise[100]. We can understand this as follows: shot noise is ultimately proportional to $(f_1 - f_2)^2$ where f_i refers to the distribution function in lead i. While shot noise arises from tunneling driven by a voltage bias giving $(f_1 - f_2)^2 > 0$, it is also possible to thermally bias one side of the scatterer. The higher temperature side has more electrons at high energies due to the Fermi distribution, which can now tunnel across the scatterer.

5.3.2 Formal Approaches to Noise in Mesoscopics

While our intuitive picture of noise is very helpful, in a complicated device geometry it can be challenging to answer the question of how source of noise in our sample couple to different contacts. Fortunately, there are a few powerful formalisms for answering this question, and they all generally become quite simple in quantum Hall devices. This section primarily follows Buttiker[101] although other formalisms can yield the same results[102].

Generically, a mesoscale device can be thought of as a scattering region which couples input and output modes of different contacts. Let us define the input modes as $\hat{a}_{\alpha m}$ for the mode m in contact α and similarly $\hat{b}_{\beta n}$ for output mode n in contact β. This allows us to describe the device (or perhaps a region of the device) with the matrix equation

$$\widehat{\mathbf{b}}_{\alpha} = \sum_{\beta} \mathbf{s}_{\alpha\beta} \hat{\mathbf{a}}_{\beta} \tag{5.15}$$

where we have suppressed that individual mode indices.

We can now write a fairly intuitive equation for the total current in a contact

$$\widehat{I}_a(t) = \tfrac{e}{h} \textstyle\sum_m \int dE dE' \left[\hat{a}^{\dagger}_{\alpha m}(E) \hat{a}_{\alpha m}\left(E'\right) - \hat{b}^{\dagger}_{\alpha m}(E) \hat{b}_{\alpha m}\left(E'\right) \right] \times \exp\left[i \left(E - E'\right) t/\hbar \right] \tag{5.16}$$

We first note that by setting $E' = E$ we find the DC component of the current, which is simply proportional to the difference between the occupation of the input and output channels, summed over the modes. AC components of this noise arise from creation and annihilation operators at different energies. This portion of the expression is not quite exact but it is somewhat intuitive that generating photons of the desired frequency require the corresponding energy differential. The integral over dE can then be viewed as an inverse Fourier transform.

This equation can be condensed somewhat by noting that the input and output modes are related so that we can write

$$\hat{I}_{\alpha}(t) = \frac{e}{h} \int dE dE' \sum_{\beta\gamma} \hat{\mathbf{a}}^{\dagger}_{\beta}(E) \mathbf{A}_{\beta\gamma}\left(\alpha, E, E'\right) \hat{\mathbf{a}}_{\gamma}\left(E'\right) \quad \times \exp\left[i \left(E - E'\right) t/\hbar \right] \tag{5.17}$$

where

$$\mathbf{A}_{\beta\gamma}(\alpha, E, E+\hbar\omega) = 1_\alpha \delta_{\alpha\beta}\delta_{\alpha\gamma} - \mathbf{s}^\dagger_{\alpha\beta}(E)\mathbf{s}_{\alpha\gamma}(E+\hbar\omega) \tag{5.18}$$

The first term of $\mathbf{A}_{\beta\gamma}(\alpha, E, E+\hbar\omega)$ still describes the occupancy of the input modes, and the second describes the occupancy of the output modes, but now in terms of the input modes of the other contacts. One quick verification of our results can be arrived at by making sure that this gives the correct DC current. By averaging over time (setting $E' = E$) and noting that terms with $\hat{a}^\dagger_\beta(E)\hat{a}_\gamma(E)$ will average to zero for $\beta \neq \gamma$, we arrive at we arrive at

$$\begin{aligned} \left\langle \hat{I}_\alpha \right\rangle &= \frac{e}{h}\sum_{\beta m}\int dE A_{\beta\beta mm}(\alpha) f_\beta(E) \\ &= \frac{e}{h}\sum_{\beta}\int dE \,\mathrm{Tr}\left[\mathbf{A}_{\beta\beta}(\alpha)\right] f_\beta(E) \end{aligned} \tag{5.19}$$

where we have made use of the fact that the number operator is the Fermi function for a given contact. This is consistent with the Büttiker formula given that

$$\mathrm{Tr}\left[\mathbf{A}_{\alpha\alpha}(\alpha)\right] = \mathrm{Tr}\left(\mathbf{1}_\alpha - \mathbf{s}^\dagger_{\alpha\alpha}\mathbf{s}_{\alpha\alpha}\right) \equiv \boldsymbol{M}_\alpha - \boldsymbol{R}_{\alpha\alpha}, \tag{5.20}$$

and

$$\mathrm{Tr}\left[\mathbf{A}_{\beta\beta}(\alpha)\right] = \mathrm{Tr}\left(-\mathbf{s}^\dagger_{\alpha\beta}\mathbf{s}_{\alpha\beta}\right) \equiv -\boldsymbol{T}_{\beta\alpha}, \tag{5.21}$$

for $\beta \neq \alpha$.

If we are interested in the noise, we should solve for $\left\langle \hat{I}_\alpha \hat{I}_\beta \right\rangle$ This is generically a cross correlation type noise, but we can find auto correlated noise by letting $\alpha = \beta$. The generic starting equation we will have is

$$\left\langle \Delta\hat{I}_\alpha(\omega)\Delta\hat{I}_\beta\left(\omega'\right)\right\rangle = \frac{e^2}{\hbar^2}\int dEdE' \sum_{\gamma\delta\varepsilon\xi}$$
$$\left\langle \hat{\mathbf{a}}_\gamma^\dagger(E)\mathbf{A}_{\gamma\delta}(\alpha,E,E+\hbar\omega)\hat{\mathbf{a}}_\delta(E+\hbar\omega)\hat{\mathbf{a}}_\varepsilon^\dagger\left(E'\right)\mathbf{A}_{\varepsilon\xi}\left(\beta,E',E'+\hbar\omega'\right)\hat{\mathbf{a}}_\zeta\left(E'+\hbar\omega'\right)\right\rangle \tag{5.22}$$

While finite frequency noise is extremely rich and interesting, we are once again interested in the low frequency limit. There is a complication to the above equation, which is that we also want to consider the effect of exchanging our current operators. In general, $\langle \Delta I_\alpha \Delta I_\beta\rangle_\omega \neq \langle \Delta I_\beta \Delta I_\alpha\rangle_\omega$ but instead $\langle \Delta I_\alpha \Delta I_\beta\rangle_\omega = \langle \Delta I_\beta \Delta I_\alpha\rangle_{-\omega}$. While this does mean that the exchanged term is equal in the zero frequency limit, at finite frequency this is an important point because noise setups can be thought of as simultaenously measuring both the positive and negative frequency. If we take these two orderings and average them, the effect is to get a factor $\delta(\omega+\omega')$ In the zero frequency limit, we ultimately obtain

$$\begin{gathered}\langle \Delta I_\alpha \Delta I_\beta\rangle = \Delta v \frac{e^2}{h}\sum_{\gamma\delta}\int dE\, \mathrm{Tr}\left[\mathbf{A}_{\gamma\delta}(\alpha,E,E)\mathbf{A}_{\delta\gamma}(\beta,E,E)\right] \\ \times\left\{f_\gamma(E)\left[1\mp f_\delta(E)\right] + f_\delta(E)\left[1\mp f_\gamma(E)\right]\right\}\end{gathered} \tag{5.23}$$

for bandwidth Δv. Here, the trace is taken over the space of pairs of modes in a given contact γ in the device. Note that the top sign refers to a Fermi distribution, while the bottom sign refers to a Bose distribution. While it is very formal, this is a very nice result because we can solve for the temperature and bias response of the noise in any device given only the scattering matrix which characterizes the device.

We can immediately apply this formula to a two terminal conductor in order to derive thermal noise and the shot noise of a QPC. For thermal noise, we begin by noting the identity $\sum_{\gamma\delta}\mathrm{Tr}\left(\mathbf{s}_{\alpha\gamma}^\dagger\mathbf{s}_{\alpha\delta}\mathbf{s}_{\beta\delta}^\dagger\mathbf{s}_{\beta\gamma}\right) = \delta_{\alpha\beta}\,\mathrm{Tr}\left(1_\alpha\right)$ If we consider $\alpha=\beta$, then $\sum_{\gamma\delta}\mathrm{Tr}\left[\mathbf{A}_{\gamma\delta}(\alpha,E,E)\mathbf{A}_{\delta\gamma}(\alpha,E,E)\right] = \left(1_\alpha - \mathbf{s}_{\alpha\gamma}^\dagger\mathbf{s}_{\alpha\delta}\right)\left(1_\alpha - \mathbf{s}_{\alpha\delta}^\dagger\mathbf{s}_{\alpha\gamma}\right) = 2(1_\alpha - \mathbf{s}_{\alpha\alpha}^\dagger\mathbf{s}_{\alpha\alpha})$

Using this and $f(1\mp f) = -kT(\frac{df}{dE})$ we find

$$\left\langle (I_\alpha)^2 \right\rangle = 4\Delta v kT \left(e^2/h\right) \int dE(-df/dE) \left[M_\alpha - R_{\alpha\alpha}\right] = 4\Delta v kTG \tag{5.24}$$

which is indeed the standard Johnson-Nyquist noise formula.

To move beyond equilibrium noise, we note that a two terminal conductor has the particular advantage that $\langle \Delta I_1 \Delta I_1 \rangle = \langle \Delta I_2 \Delta I_2 \rangle = -\langle \Delta I_1 \Delta I_2 \rangle$ owing to current conservation. For the zero temperature, finite voltage case, we find

$$\left\langle (\Delta I)^2 \right\rangle = 2\Delta v \left(e^2/h\right) \int dE \left(f_1 - f_2\right)^2 \mathrm{Tr}\left(\mathbf{s}_{11}^\dagger \mathbf{s}_{11} \mathbf{s}_{21}^\dagger \mathbf{s}_{21}\right) \tag{5.25}$$

First we note that $\int dE(f_1 - f_2)^2 = |eV|$. Secondly, if we realize s_{11} is a reflection amplitude and s_{21} is a transmission amplitude, in the basis of Eigenchannels we arrive at we arrive at

$$\left\langle (\Delta I)^2 \right\rangle = 2\left(e^2/h\right) \Delta v |eV| \sum_n T_n \left(1 - T_n\right) \tag{5.26}$$

where the sum is over all channels. This is our classic shot noise. We can find the standard tunneling limit by approximating $(1 - T_n) \approx 1$ and noting that the current flowing will be $e^2/hV \sum_n T_n$, yielding $F = 1$. But we now have a significantly more general formula, where it is possible to determine F just by knowing the transmission of all channels.

Combining thermal and shot noise we can straightforwardly arrive at a generic two terminal conductor formula

$$\left\langle (\Delta I)^2 \right\rangle = 2\Delta v \left(e^2/h\right) \int dE \sum_n \left[T_n f_1 \left(1 \mp f_1\right) + T_n f_2 \left(1 \mp f_2\right) \pm R_n T_n \left(f_1 - f_2\right)^2\right] \tag{5.27}$$

If we consider the case of a Fermion system, it is possible to express this as

$$\left\langle (\Delta I)^2 \right\rangle = 2\Delta v \left(e^2/h\right) \times \sum_n \left[2k_B T T_n^2 + R_n T_n eV \coth\left(eV/2k_B T\right)\right] \tag{5.28}$$

In order to physically understand this formulation, note that $eV = 0 \rightarrow eV\coth(ev/2k_BT) = 2k_BT$ so that the whole term in the sum simplifies to $2k_BT$, the expected thermal noise. In the limit of high voltage bias, we arrive that something proportional to VR_nT_n, which is our standard shot noise form.

From an experimental perspective, there is something extremely valuable about this equation. As we increase the voltage bias, the change in the noise is proportional only to $\coth(eV/2k_BT)$. This means that if we have a tunnel junction of known resistance we can easily measure the electron temperature of our system. What is particularly valuable here is that the system is “self-calibrating” in the sense that background noise of the amplifiers and gain uncertainty do not contribute to uncertainty of the temperature measurement. This also makes such a measurement particularly convenient for calibrating the gain and input voltage noise of an amplifier. This type of measurement is described at the end of chapter 6.

6

MHz Cryogenic Noise Measurement Setup

6.1 A Brief History of Mesoscopic Noise Experiments

As previously mentioned, noise is a very powerful tool and technique for studying nanoscale devices. While there were attempts to measure fundamental noise signatures in mesoscopic devices in the 1980s and early 1990s[103, 104], it wasn't until the late 1990s that fundamental noise was first very successfully measured with breakthrough experiments measuring fractionally charged particles in fractional quantum Hall states. The setup used by the Weizmann group has largely become the template for the modern cryogenic MHz noise setup, there have been several variations and improvements over the years. In this section I will discuss various design decisions and the performance of the system.

6.2 The Cryogenic Amplifier

In order to probe physics at very low energy scales, we require a measurement setup with the lowest background signal possible. The Dicke radiometry formula tells us that the uncertainty of a noise temperature measurement δT is

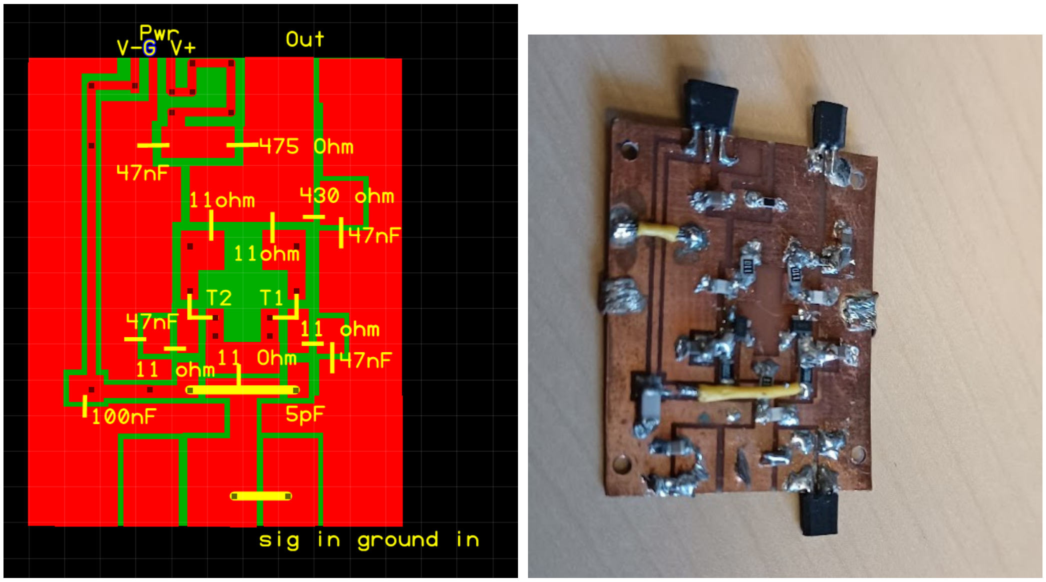

FIGURE 6.1: Amplifier schematic (left) and prototype board (right)

$$\delta T = \frac{T + T_N}{\sqrt{\tau \Delta f}}$$

where T is the amplitude of the noise being measured, T_N is the noise temperature of the system, τ is the measurement time and Δf is the measurement bandwidth[105]. Note that while all noises here are expressed in terms of a temperature, we can replace with something proportional to V^2 if desired. There is a positive note – we see that we can hit arbitrary precision by measuring for a longer period of time. However, consider a concrete example: suppose we have a room temperature amplifier with $2\frac{\text{nV}}{\sqrt{\text{hz}}}$ input noise and 5 kHz bandwidth, as well as a cryogenic amplifier with input noise $0.3\frac{\text{nV}}{\sqrt{\text{hz}}}$ and 30 kHz bandwidth. If we are trying to measure a small signal $T << T_N$, then we have to measure for 266 times longer to achieve the same precision with the room temperature setup as the cryogenic setup.

While RF electronics excel at both low background signal levels and large bandwidths, the large impedance of nanoscale devices with resistances on the order of R_Q makes it challenge to RF match them. To avoid such matching, we work with a

MHz cryogenic amplifier. This allows us to improve both on the background signal, because the low temperature reduces the fundamental noise of our amplifier, and to achieve higher bandwidth, by putting the amplifier closer to the sample and reducing the capacitance between the sample and amplifier. Unfortunately, many transistors are prone to "freezing out" and becoming nonfunctional at low temperatures. Fortunately, high electron mobility transistors (HEMTs) are still functional at $\approx$1 Kelvin scale temperatures and can thus be used as the basis for the cryogenic amplifier. Systems of this type are routinely able to hit input noise levels of $\approx 0.3\frac{nV}{\sqrt{Hz}}$ It is worth noting that while it is possible to hit comparable input noise levels at room temperatures with bipolar junction transistors, such systems have very low input impedance which is undesirable when measuring samples with resistances on the scale of R_Q.

Throughout my PhD we primarily used the no longer produced ATF-38143 transistor. This was more readily available than and is minimally different from the more commonly used ATF-34143.

For the amplifier topology, we use two parallelized HEMTs in a common source configuration. The advantage of this topology is simply to reduce the input noise by $\sqrt{2}$ while keeping things simple. It is also possible to use other topologies, such as a single HEMT common source, a cascode arrangement or a current amplifying configuration. Ultimately there should be minimal difference between configurations when using fairly small (kOhm or lower) resistors in the amplifier design, since these components contribute minimal thermal noise at 3 K and all of the noise should originate from the HEMT itself.

The schematic of the cryogenic amplifier, as well as the physical implementation of a test circuit, is shown in Figure 6.1. In designing any amplifier, we begin by first choosing a DC operating point (a combination of V_{GS} and V_{DS} has to be chosen. As will be seen in the subsequent section, the gate is DC grounded. In order to avoid having to pass separate source and drain biasing lines to the transistor in order to independently tune V_{DS}, V_{GS}, we rely on "self biasing" where, by attaching a resistor to the source of the amplifier, we allow V_S to be raised by $I_{DS}R_S$. Thus any combination of V_{DS} and V_{GS} can be reached by appropriate choices of R_S, R_D and applied voltage.

For a given V_{GS}, the optimal V_{DS} in our system is the minimal voltage that saturates the transistors, as higher voltage will not increase the gain of the system but will increase the heatload of the amplifier. The optimal V_{GS} is a trade off: a higher V_{GS} may lead to higher gain and, hopefully, lower input noise, but will also increase the heat load, and, to a certain degree, the nonlinearity of the amplifier. Normally, the ATF-38143 operates at room temperature with I_{DS} on the order of 100 mA, but this would generate far too much heat load, so V_{GS} is a substantial negative value to achieve saturation at for mA scale I_{DS}

Once all of the DC components have been chosen, we can choose components to optimize the AC performance. This can be done by placing any AC resistors in series with a large capacitor to prevent it from altering the DC performance. Gain is maximized by AC shunting the source resistor. The only downside of this process is that it will lead to small variations in the gain of the amplifier as a function of frequency, due to the fact that the impedance of the shunt is varying with frequency. To minimize this effect, we placed 11 Ohm resistors in series with these capacitors, although this does have the effect of slightly reducing gain.

While gain is maximized by having a larger R_D, an issue that must be considered is that the output resistance of the amplifier in combination with the capacitance of the output line, may filter the measured signal. To avoid this issue, we reduce the AC output impedance of the amplifier to approximately 200 Ohm.

Other components are chosen to reduce the odds of generation, or to filter the DC biasing line.

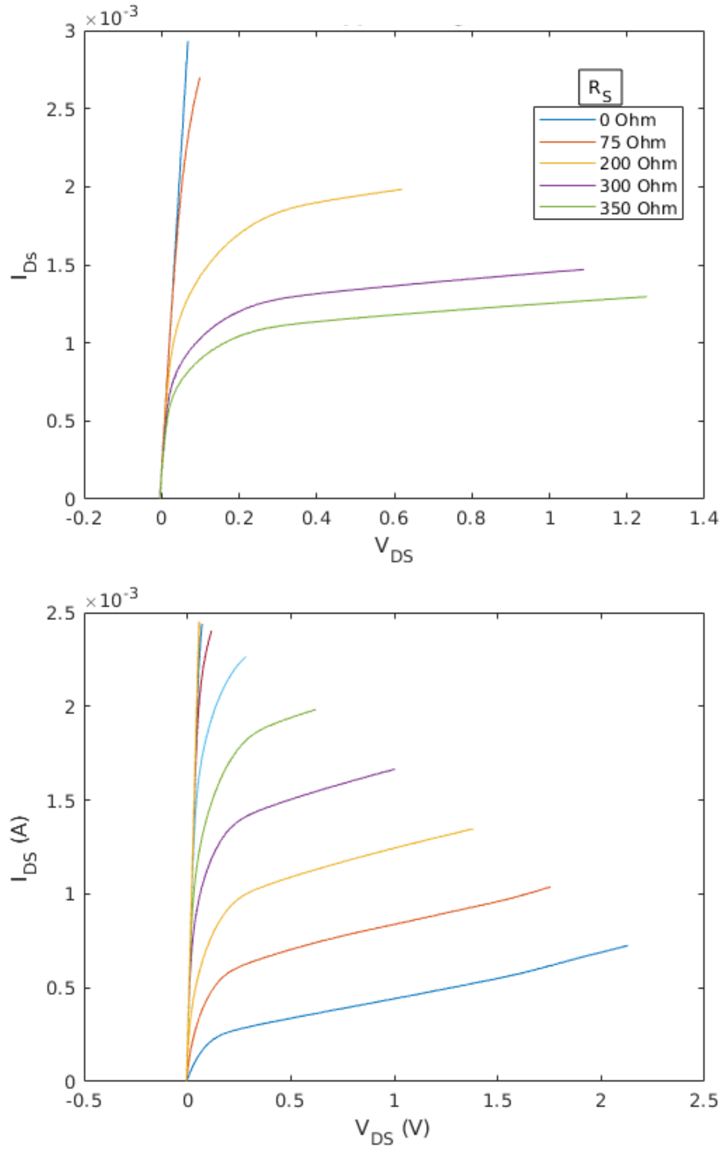

FIGURE 6.2: Cryogenic IV curves of the ATF 38143. Like most HEMTs, the low temperature IV curves are significantly different from the room temperature curves, showing reduced current for a given V_{DS}. The top figure show the effect of self biasing, with 0 V applied to the gate. While the amplifier is normally unsaturated, by adding a source resistor we can cause the amplifier to saturate for a small enough current to avoid overheating the fridge. Around 200 ohms is optimal, because too much more leads to a significant reduction in gain. The bottom figure shows the gate voltage dependence of the IV curves for 200 Ohms R_s. This gives further tunability, but in practice we keep the gate DC grounded.

6.3 Resonators

HEMTs unfortunately suffer from significant $\frac{1}{f}$ noise, up to frequencies in our system of ≈ 300 kHz, which makes it desirable to operate at frequencies $\approx$ 1MHz. This presents another issue: for samples with resistance $R \approx R_Q$, the capacitance between the amplifier and the sample must be less than 6 pF to minimize self filtering. However, this is an essentially impossibly small amount of capacitance.

This obstacle can be overcome by adding an inductor to ground between the sample and the amplifier. The effect of this is to shift the center frequency to $\frac{1}{2\pi\sqrt{LC}}$, while preserving, for an ideal inductor, the bandwidth $\frac{1}{2\pi RC}$

In practice, producing a nearly ideal inductor was surprisingly challenging. We were initially working with commercial components from coilcraft, which were ceramic core copper wire inductors. However, these had significant losses which can be quantitatively characterized by saying that the inductor acted more like an inductor in parallel with a 25 kOhm resistor at 4 K when it was shunted by enough capacitance to form a resonator at 1 kOhm.

The effect of this resistance has two effects. The parallel combination of this resistance and the sample resistance reduces the signal amplitude to but increases the bandwidth. In the net this should be a moderate loss of total signal, but in practice it is typically hard to increase the bandwidth too much due to spurious background noise peaks. We also made the additional mistake of placing the inductor on the 3K plate initially, which leads to an additional signal of the thermal noise of 25 kOHm at 3 K, which is a significant 2 $\frac{nV}{\sqrt{Hz}}$ before accounting for the equivalent resistance.

When attempting to wind our own inductors, our first designs were based on conventional Nb-Zr and Nb-Ti wire. However, we found that the losses did not seem to be substantially better, which we attributed to the Cu or Cu-Ni coating on the outside of the wires. This is a resistive metal coated on the wires because the

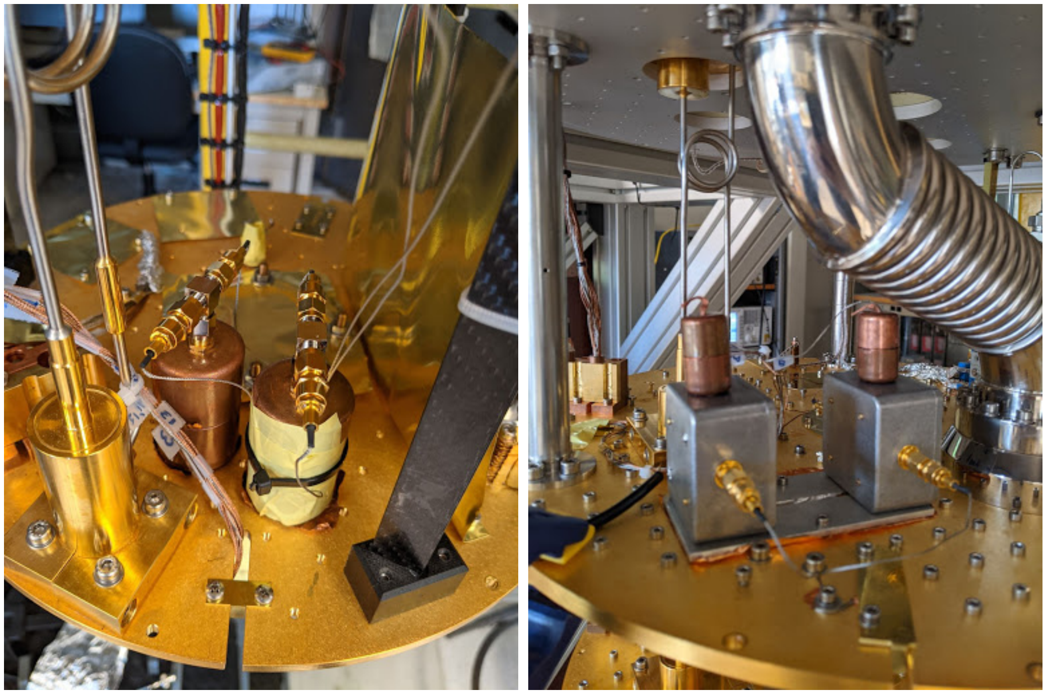

FIGURE 6.3: Left: Resonators mounted on the mixing chamber plate. Each copper egg has a coil wound around PVC inside, held in place with a 3D printed part. The top of each egg has a single SMA, with one end of the coil connected to the signal pin, and one to the ground. An SMA tee is then connected on top, so that the amplifier and sample can be connected. Right: cryogenic amplifiers, mounted in die cast aluminum boxes. The top of each die cast box has an additional copper pill box to shield the power input lines. Amplifiers are aligned on an aluminum mounting plate and a piece of copper foil is used to interface the aluminum plate to the 3 K plate of the fridge, due to fears of degradation of the 3K plate interface.

superconducting material is usually difficult to solder. However, at MHz frequencies it seems possible that the skin effect pushes all of the AC current to the surface of the wire and thus induces substantial losses. We note that other groups can often skirt this issue by working at frequencies around 700 kHz, which helps to reduce these losses (details are discussed at the end of this section).

While a truly optimal inductor is likely to involve superconducting wire without a resistive coating, in practice it was easier to work with high quality copper wire. A few trends about making low loss inductors (which can be observed in certain applied engineering texts) were observed

- Layered windings tend to significantly increase the loss, as currents between adjacent layers repel and reduce the effective current carrying area. If layering is essential, spacers can be used, although we ultimately used a single layer coil.

- Having a larger inductance is generically better, because of the formula $R_{parallel} = \omega^2 L^2 / R_{series}$, so even thought R_{series} increases with wire length, the effective inductance will increase faster.

- Likewise, thicker coils have higher inductance per unit length of wire. It is worth noting that the solenoid formula becomes inaccurate for coil length and width of the same order and the so called "helical coil" formula must be used instead. Very wide coils will also eventually suffer from larger radiative losses, although there was no evidence to suggest we ever reached this limit.

- It is important to shield the inductor well, since it is very easy for ambient noise to couple to the coil. However, as the coil gets close to the walls of the shielding, losses can increase significantly.

6.4 Wiring

This system requires somewhat precise wiring, in order to minimize losses while ensuring that all plates are thermally isolated.

The wire from the HEMT input to the inductor is superconducting Nb-Ti with a Cu-Ni shield, which is carefully thermalized at each stage. This same type of wire then extends down to the input SMP of the puck. Superconducting wire is used to connect the puck to the blocking capacitors, to minimize any risk of the amplifier wires heating the sample.

Wiring from the HEMT amplifier to the room temperature SMA uses a shielded twisted pair in order to minimize output capacitance of the amplifier.

6.5 Room Temperature Amplification and Readout

After being passed to a room temperature SMA, the signal is fed to an NF SA-421F5 amplifier. This amplifier has $0.5\frac{nV}{\sqrt{Hz}}$ input noise and 46dB gain. This is then capacitively coupled (in order to break the DC ground loop) to an Agilent N9000A spectrum analyzer.

The spectrum analyzer can be operated in a few different ways in order to measure the noise. The simplest is to measure channel noise power centered on the Lorentzian of the tank circuit with a minimal span and a video bandwidth of the desired measurement width. This produces a single number corresponding to the noise amplitude. Occasionally, there would be periodic bursts of noise, which we typically attributed to digital electronics in the system. One way to avoid these is to measure a large number of short time scale points (for instance, recording 50x100 ms measurements to measure for 5 s) so that outliers can be removed. It is often possible to remove such bursts by adjusting the grounding of the fridge.

Alternatively, it is possible to use the spectrum analyzer to FFT the signal. This can make it easier to remove noise spikes, and has the additional benefit that measuring the resonance insures that there is no change in the device resistance (or if there is one, that it can be corrected for). However, it is programatically more challenging and requires spending some amount of time measuring a band with low signal to noise ratio.

Lastly, it is possible to work exclusively with a fast digitizer. This is a natural way to do cross correlation measurements, although it is also possible to use an analog multiplier. When digitizing, it is essential to use a PXIe setup or PCIe card, in order to have the necessary bandwidth to transfer signal as quickly as needed to the computer.

6.6 Grounding Issues and External Noise

Without careful grounding and control of local electromagnetics, typically one measures a very noisy background spectrum, characterized by both ugly peaks and a very high level of white noise, even if the amplifier and measurement lines appear to be well shielded.

For the Oxford dilution fridge wired with our cryoamps, one of the primary sources of background noise is the various heaters of the Oxford thermometry system. These noise can be significantly removed by disconnecting these heaters from the fridge, and using an external voltage source to apply heat if necessary. This noise was further improved by taking the thermemotry scanner and removing it from the Oxford gas handling system and mounting it close to the frame of the fridge, similar to how it is recommended to be done in the Lakeshore 372 Resistance Bridge manual.

As initially setup, the Oxford Triton was grounded through the magnet power supply, with the metallic frame which supports the refrigerator floating. However, the optimal setup for our MHz noise setup involved grounding the fridge to the shielded room, and the frame separately to a metallic pipe on the other side of the room.

It is also worth noting that the amplifier showed approximately 20% increased background noise when the magnetic power supply is connected to the magnet. This noise can be removed by setting the magnet in persistant current mode.

6.7 Calibrations

Calibrations were primarily performed with an aluminum shadow evaporation tunnel junction fabricated by Zubair Iftikhar. The junction is around 98 kOhm at base temperature. Because the junction is not chiral like a quantum Hall sample, it is

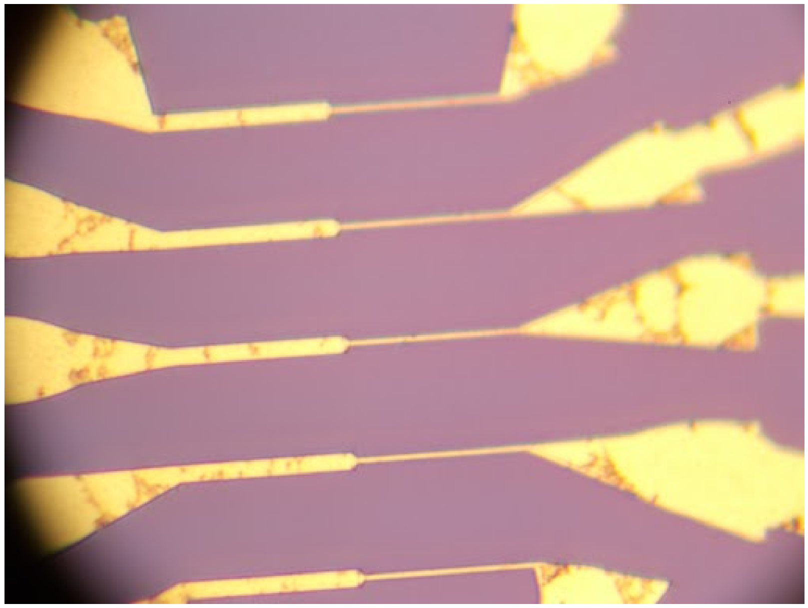

Figure 6.4: Optical image of the aluminum tunnel junctions studied. The small overlapping region is the junction formed by shadow evaporation

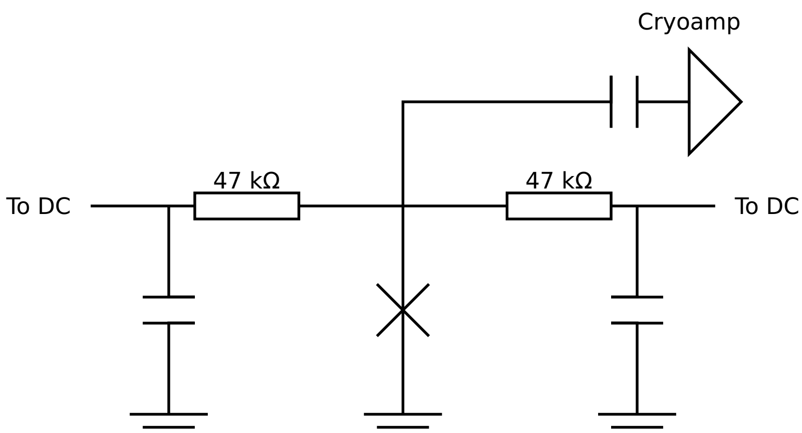

Figure 6.5: Measurement circuit for the tunnel junction noise. Isolating resistors are used to disconnect the sample from the capacitance of the measurement lines, so as to avoid changing the resonant frequency of the measurement circuit

important to use resistors to isolate the junction from the capacitance of the DC biasing lines. 200 mT was applied to insure that the aluminum in the junction was not superconducting.

The value of the tunnel junction is that we can safely assume it has a Fano factor of $F = 1$, and then fit the equation derived at the end of the last chapter. We found a fridge base temperature of around 27 mK and an amplifier performance of around $0.3\frac{\mathrm{nV}}{\sqrt{\mathrm{hz}}}$ input noise and a voltage gain of around 4.5.

The primary obstacle for the accuracy of our calibration is a certain non-linearity of the IV curve of the tunnel junction, which we attribute to the dissipative environment formed by the long thin leads. More accurate calibrations can naturally be accomplished by using thicker leads, to avoid this effect[106].

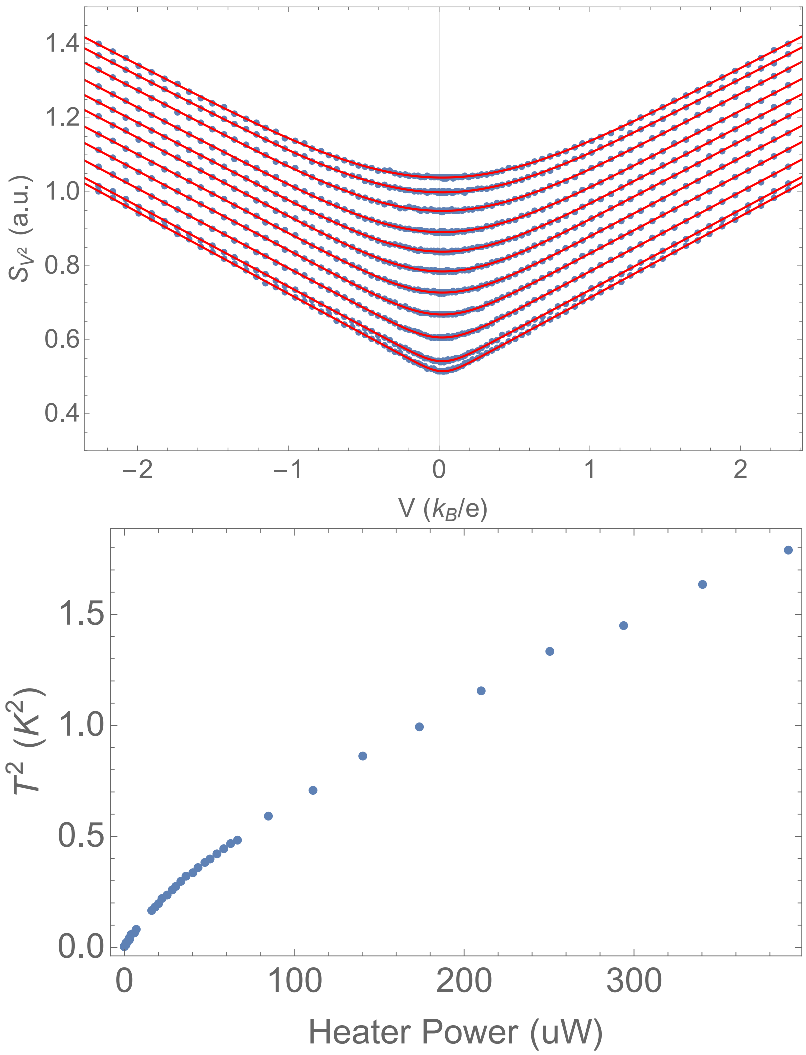

FIGURE 6.6: Data from the tunnel junction calibration. Top: shot noise vs sample voltage for several different temperatures. Blue points are data, red lines are fundamental fits. Bottom: fitted temperature vs applied temperature on the sample heater, showing a clean power law dependence (this particular power law seemed to stem from poor thermalization on this particular cooldown).

7

Noise of Chiral Andreev Edge States

7.1 Introduction

Coupling superconductivity and the quantum Hall effect has been a long standing goal in the field of quamtum transport. Such coupling is a natural route to non-Abelian anyons which could form the basis for topological quantum computation. While inducing superconductivity in a semiconductor device at the magnetic fields required for the quantum Hall effect is challenging, recent research has shown considerable experimental progress in this regard.

One such experiment of particular relevance for this work is the recent observation of the interference of chiral Andreev edge state[10]. Here, when a current flows along a quantum Hall edge towards a grounded superconducting contact, it is possible to observe both a postive and negative nonlocal voltage downstream of the grounded contact. Such a signal indicates that at least some of the incoming signal is Andreev reflected.

One outstanding question with this experiment is about the signal amplitude. In an ideal device, the nonlocal resistance should reach $\pm\nu G_Q$, where ν is the filling

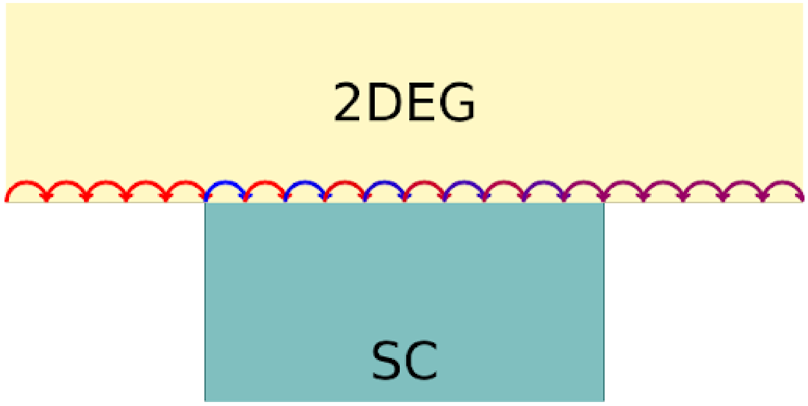

FIGURE 7.1: A schematic of the way in which dephasing could lead to reduced signal. Here, we are using red and blue cyclotron orbits to refer to electron and hole particles, respectively. However, as particles propogate along the interface, fluctuations of the electron hole character along this trajectory may lead to a nearly equal mix of electrons and holes being emitted by the contact

factor and G_Q is the conductance quantum. However, in experiment, it is typically only possible to reach $1 - 10\%$ of this value. Two viable explanations are as follows: 1) the output signal is made of a roughly equally mixed electron-hole hybridized state, and that it is quite challenging to realize a significant imbalance of carriers. In this interpretation, a 10% signal could be completely holes with all other particles being lost into the contact, while the prior interpretation would argue that this signal should arise from 45% electrons and 55% holes (this is plotted schematically in Figure 7.1). Or 2) the vorticies in the superconductor lead to particle loss, significantly reducing the signal. There is substantial evidence that rearrangements of vortices significantly impact the observed signal, both theoretically and in experiment, where repeatable stochastic jumps in the signal are attributed to vortices. This is shown schematically in Figure 7.2.

One possible way to probe this question is through the use of noise measurements. Measurements of the noise should give a signal proportional to var(q) where q is the charge of the Andreev edge state carriers. As a result, case (1) should give substantial noise, while case (2) should result in significantly reduced noise.

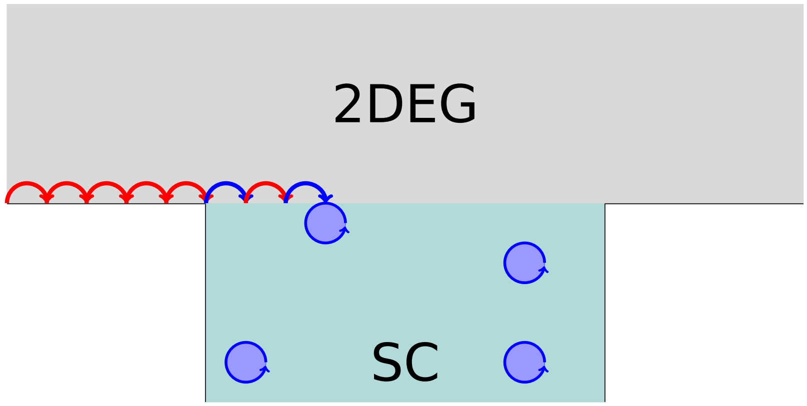

FIGURE 7.2: A schematic of the effect of vorticies on chiral Andreev edge states. A quantum Hall edge incident on a local superconducting contact may go through Andreev reflection, but if the contact has vorticies, these local normal regions may absorb the particle.

7.2 Prior Work

Recently, Sahu et al[107] measured the noise of a graphene Josephson junction in the quantum Hall regime. The authors observed enhanced noise, particularly at low magnetic field, which they attribute to CAESs. At the lowest biases and magnetic fields, they find $F \approx 0.5$ (Figure 7.3). This is consistent with a toy model that assumes the edge states are neutral, thus the probability of Andreev reflection is given by $P_{AR} = \sin^2(\phi/2)$ where $\phi = (k_1 - k_2)L$ is the difference of phase between the two $e \pm h$ edge states acquired over the length of the device. Assuming that phase is well randomized by the edge disorder, averaging over ϕ ultimately leads to the $F = 0.5$ result.

These results are interesting, and consistent with the simple model, but they elicit some questions. The authors assume a given superconducting contact emits an equal mixture of electrons and holes in the quantum Hall regime. This would naturally explain the lack of CAES signals shown in many devices, but it is unclear if this is generally true, as mentioned in the prior section. If this is the case, what makes the devices of Ref [10] special is not that they have signal at all, but the fact

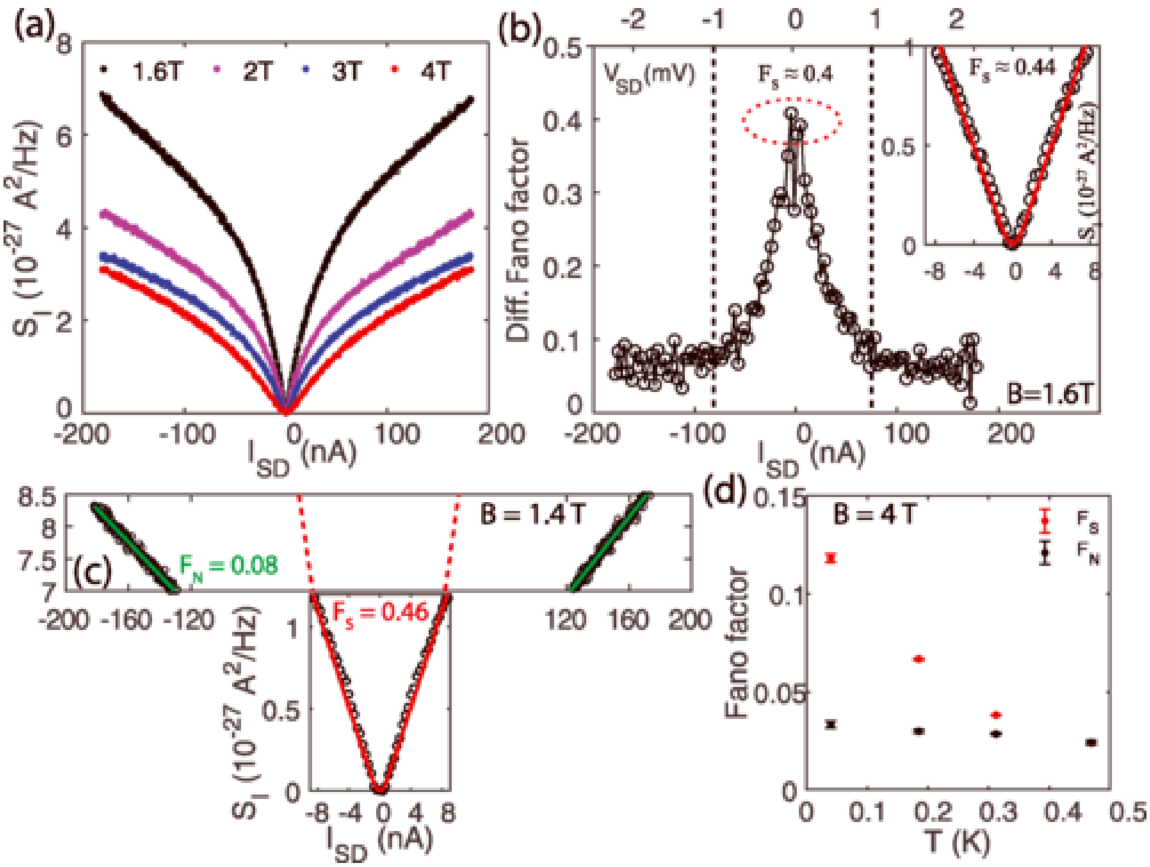

FIGURE 7.3: The primary results of [107], adapted from the paper. a) depicts the noise measured as a function of bias current for several different magnetic fields. While the Fano factor is quite large for low bias (c) it becomes reduced at higher bias, consistent with biasing outside of the induced superconducting gap. The high low bias Fano factor also gradually decreases with magnetic field and temperature, consistent with [10]

that they can imbalance the electron and hole ratio.

Another aspect to consider is that ideally superconductors are ideal thermal insulators. Recent work has measured the quantized thermal conductance of the quantum Hall effect by biasing current towards a floating island[5]. Our measurements below show that the noise vs bias curves of these two experiments are nearly identical. At low temperature, the thermal noise should be linearly proportional to the applied bias current, but at higher bias currents the edge state may overheat, causing increased thermal conductivity through phonons and thus a reduced Fano factor.

At higher magnetic fields, the vortex density should increase, leading to increased thermal conductivity of the SC contact and thus a reduced noise signal.

The primary obstacle with this explanation is that generally superconducting thin films appear to be less thermally isolating than they are expected to be[108], and that the vorticies should probably lead to a high enough thermal conductivity of the contact[109, 110] that the thermal noise measured should be small. Still, it appears challenging to detangle these two effects experimentally.

7.3 Comparing Superconducting and Normal Contacts

Ultimately, we present data on two devices in this chapter, the first of which is discussed in this section. This device is shown schematically in Figure 7.4. One contact is connected to a cryoamp so that we can measure the noise at this terminal. On either side of this contact there is a cold grounded contact, one of which is superconducting and one of which is a standard Cr/Au normal contact. On the other side of the grounded contacts is a contact for biasing DC current. This allows us to bias DC current and measure the downstream noise of either a superconducting contact or a normal contact depending on the direction of the magnetic field.

In Figure 7.5, we present a map of the measured noise downstream of the superconducting contact as a function of the applied DC bias current and the magnetic field perpendicular to the sample. The gate voltage is such that the filling factor is $\nu = 2$ throughout the entire map. Our results are fairly consistent with those observed by Sahu et al. At the lowest magnetic fields and bias currents, it is possible to observe a relatively large noise signal, consistant with a Fano factor F > 0.1. As we increase bias, the Fano factor continuously declines until the noise levels off at nearly a plateau. As the magnetic field is increased, both the low bias Fano factor and the level of the noise plateau at high bias begin to decrease. Around 5 T, we observe that the curve more or less saturates, and shows minimal change going up

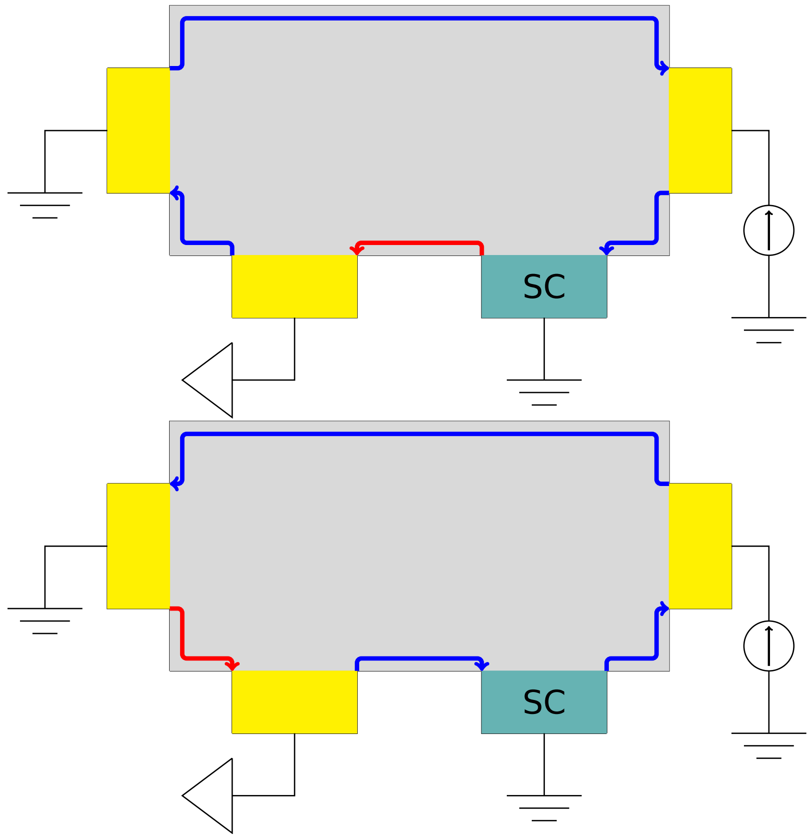

FIGURE 7.4: The sample schematic used for Section 7.3. The top figure shows the primary configuration, with current flowing towards the grounded superconducting contact, so that any emitted noise can be measured by the downstream cryoamp. Here, blue edges are essentially noiseless edges (containing only the thermal noise of the base temperature contacts), while the red edge contains the additional downstream noise. The bottom shows the alternate configuration which can be achieved by reversing the magnetic field direction. By doing so, we are able to measure the noise downstream of a normal contact as a control.

to 10T.

Figure 7.5 also shows the same measurement with the direction of the applied magnetic field reversed, such that we are measuring downstream of the normal contact. Surprisingly, we find a pattern that is qualitatively fairly similar, with large Fano factors for low bias, saturation at high bias, and a steady decrease in both signals as the magnetic field is increased. At the lowest field we find Fano factors of this normal contact as large as $F \approx 0.25$ on a quantum Hall plateau. While previous results have found that contacts can sometimes show some residual shot noise in the quantum Hall regime, such a large Fano factor is quite surprising to measure while observing a quantized resistance, and presumably inconsistent with a purely shot noise source.

While these contacts do not exhibit completely identical behavior, we believe that these signals are similar enough to consider that they have a common origin. An interesting variation on the thermal noise scenario proposed in section 7.2 is that neither superconducting nor normal contacts manage to properly thermalize the edge state. The conditions of the chiral Andreev edge state force us to work at relatively low fields and with fairly short contacts. It is possible that this combination of short contacts and low magnetic field, and thus large magnetic length, result in an the edge state is not completely thermalized by the contact, but instead is emitted from the contact at an elevated temperature.

Downstream from the superconductor, this process is more complicated, owing to the thermal effects of vorticies described previously. Thus we expect that the thermal conductivity of the superconducting contact should be lower, thus leading to higher temperature and therefore higher noise.

In either case, the specifics of the thermal noise dependence may be complicated. For either the normal or superconducting contact, as bias increases, the contact interface could heat up, leading to increased thermal conductivity and thus sublinear noise as a function of bias. We believe this explains the bending shape, although quantitatively this will depend on the size of the contacts and the distance from the measuring contact.

7.4 Measurements in a Device with Large CAES Signal

The second device we studied is schematically very similar, although with four superconducting contacts. This device is studied due to the large amplitude of its nonlocal

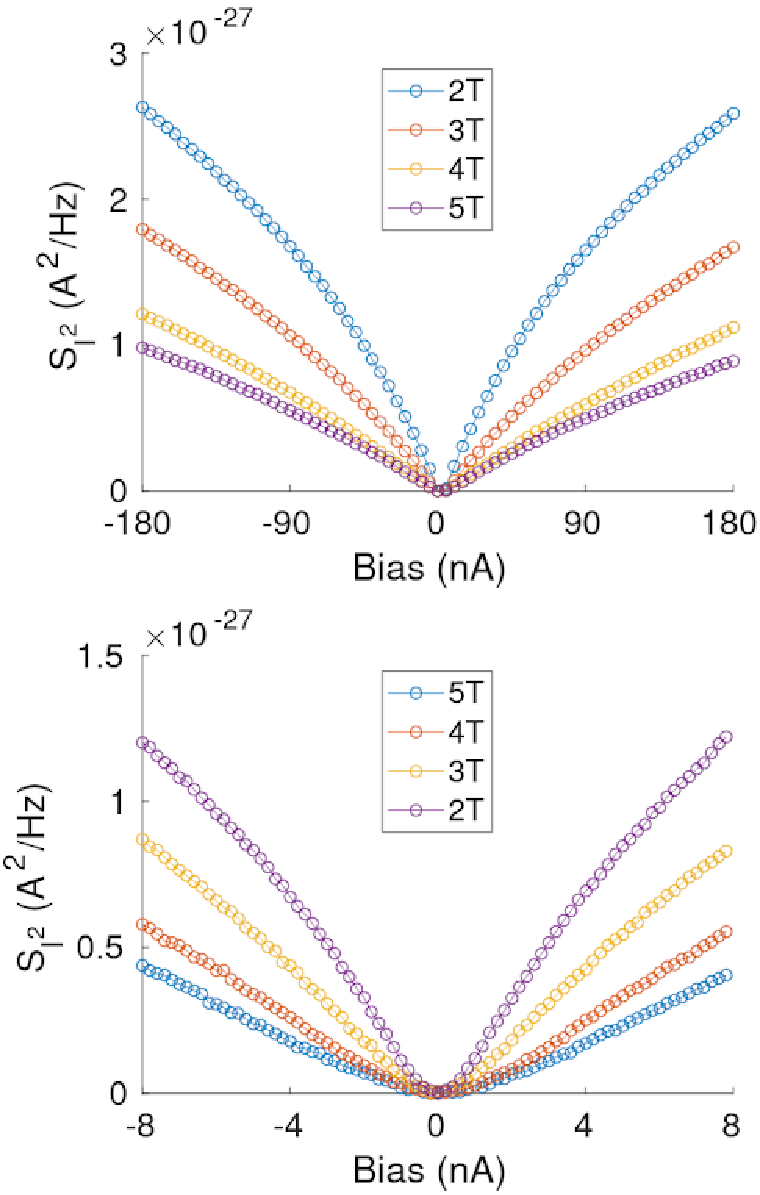

FIGURE 7.5: Output current noise S_{I^2} as a function of DC bias current and magnetic field downstream of a normal contact (top) and a superconducting contact (bottom). While there is a quantitative difference between curves, qualitatively they remain fairly similar

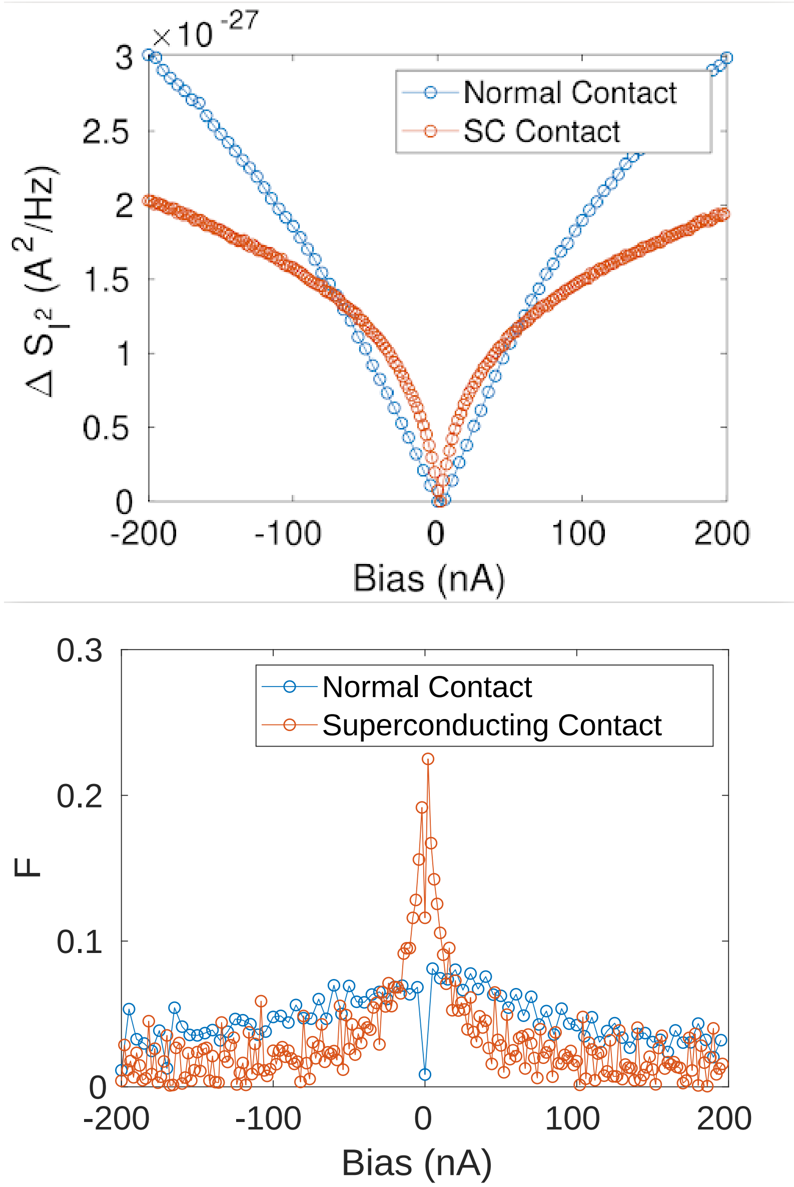

FIGURE 7.6: A single magnetic field cut comparison of the two contacts at 2T. While the noise is significantly higher at low bias for the superconducting contact, the scale of the two signals remains reasonably comparable. Bottom: Differntiated curves for the two contacts. The supeconducting contacts result of $F \approx 0.2$ at 2 T is quite comparable to the result of Sahu et al. at 2 T.

signal for one contact, on the order of 10% of the quantized resistance on the $\nu = 2$ plateau.

One way in which we can attempt to measure the shot noise of the chiral Andreev edge state decoupled from this thermal noise is to measure the observed noise at finite bias as a function of the gate voltage at a constant filling factor. When measuring the DC signal, we can sweep V_G, modifying the electron density and causing the nonlocal resistance to oscillate. If this change in signal arises due to a change in the electron to hole ratio, rather than because of a change in particle loss, we believe the measured noise should also oscillate, although out of phase with the nonlocal signal, because an equal mixture of electrons and holes should result in zero nonlocal resistance but larger noise than streams of only electrons or only holes.

We emphasize having a large tunability here as the noise should be proportional to the var$(\frac{q}{e})$. Thus, even our sample with DC signal on the order of 10% of $2G_Q$ may only exhibit Fano factor variations of 0.1. Since the AC coupled cryogenic amplifier is not compatible with DC nonlocal measurements, the sample is rebonded and recooled between the two measurements. The observed results are plotted in Figure 7.7. The entire figure is measured with 9 nA of applied bias, which should be enough to cleanly measure variations in F, while potentially avoiding saturation of the noise at higher bias. Qualitatively, the results are fairly consistent with our expectations. At 3 T, we see minimal variation in the Fano factor across the entire range of the plateau. For the lowest three magnetic fields however, we do see some oscillations that seem to be statistically significant. However, the observed oscillations are still very small. They correspond only to variations of the Fano factor on the order of 0.005, more than an order of magnitude smaller than one would naively expect.

Furthermore, it is possible that even these small oscillations we observe arise due to alternative mechanisms. Possibly, by tuning the electron density and thus the trajectory of the quantum Hall edge along the contact, we slightly change the extent to which this edge can thermalize to the contact, and this variation in signal is actually variation of the thermal noise rather than the shot noise. Alternatively, slight imperfections in contract transparency even in the quantum Hall regime have been connected to small Fano factors.

Regardless of the exact origin of this small signal, we believe there is some mechanism by which the shot noise of the chiral Andreev edge state is suppressed.

7.5 Conclusion

In summary, we have measured the noise downstream of superconducting and normal contacts in the quantum Hall regime. While we require measurements on additional devices in order to confirm these results, we believe that in graphene devices at low magnetic field (typically below 4 T, in reasonable device geometries) the quantum Hall edges may fail to completely thermalize with a grounded contact, which may be an important consideration for a range of quantum Hall devices. Beyond that, we believe that the shot noise of chiral Andreev edge states are significantly suppressed. This may be due to “equilibration”, or inelastic scattering processes, which have been shown to give a suppression of noise which scales exponentially with interface length[111].

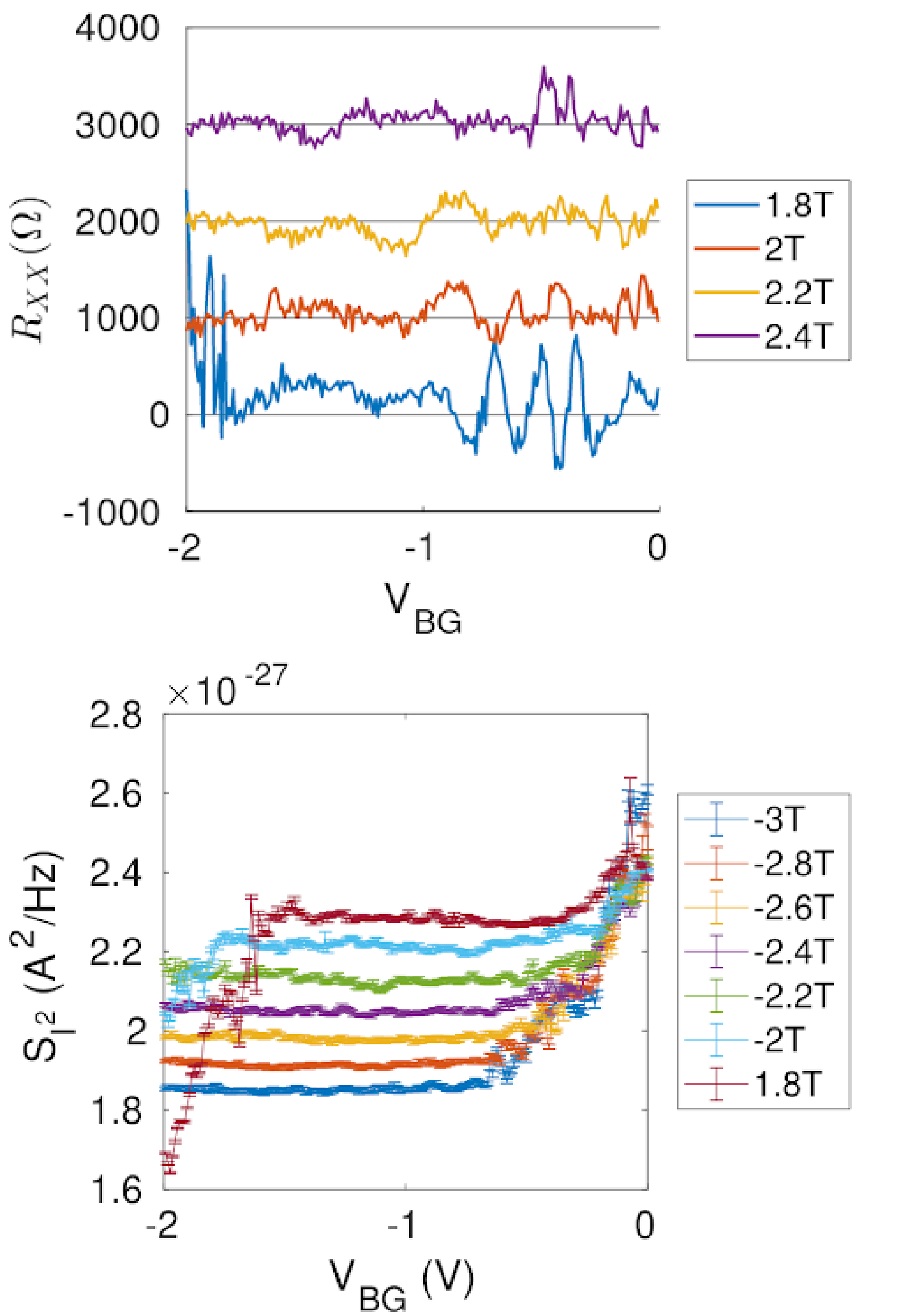

FIGURE 7.7: Measurements of the second device. Top: resistance fluctuations of the large signal contact as a function of magnetic field. Curves are manually offset, but at 1.6 T we observe approximately 1 kΩ fluctuations correspond to roughly 8% electron to hole conversion. Bottom: Noise measured on the same device in a separate cool-down with a bias of 9 nA. Here we observe small fluctuations in the noise, which ultimately correspond to fluctuations in the Fano factor of ≈ 0.01, which are thus more consistent with case (1) discussed at the beginning.

8
Conclusion

AC measurements of quantum materials are a varied and promising approach which is certain to produce significant results in the coming years. While the end of each experimental chapter presented some simple ideas for next steps, this section focuses on other projects that can be readily realized using these and similar techniques.

One of the most immediately promising next steps for graphene noise measurements is attempting to measure the thermal conductivity of the quantum Hall ferromagnetic states, in particular $\nu = 0$. While the $\nu = 0$ quantum Hall state can take a number of different forms depending on the particular energy scales[112], the canted antiferromagnetic state should host magnons (spin based goldstone modes). Such magnons have recently been shown to be gapless[113], and should mediate heat even in the absence of standard electronic thermal conduction, leading to significant violation of the Wiedeman-Franz law[114].

We currently have a design for this sample with a few viable variations. The essential design is a hall bar with the middle section having a local topgate and floating metallic islands on either side of the device. When the floating metallic island has two grounded contacts downstream of it, a Landauer-Buttikker calculation shows that it acquires a voltage $I\nu G_q/2$. Combined with the quantized thermal conductance of the quantum Hall edge states, this gives it an easily determinable temperature[5].

By setting the topgated region to $\nu = 0$ and the other regions to an integer state, we can use heat one floating island to thermally bias one side of the $\nu = 0$ region. It should then be possible to measure the temperature of the edge state flowing out of the other metallic contact.

The two variations depend on whether the floating islands are coupled to the $\nu = 0$ region directly (by having the gated region overlap with the islands) or indirectly, with integer Hall loops mediating the interaction. Presumably the former leads to stronger thermal coupling, but is more challenging to fabricate, as care must be taken to avoid shorting the floating islands and the gate.

Observing a violation of the Wiedemann-Franz law would be an exciting result for this system, and the possibility of tuning into a different $\nu = 0$ state which lacks enhanced thermal conductivity, such as the ferromagnetic state, which has previously only been observed by nonlocal transport. Similar work can also be initiated with a quantum spin liquid candidate material, such as $RuCL_3$. These materials are electrically insulating but has been shown to exhibit quantized thermal conductance as well as thermal conductivity oscillations in bulk materials[115, 116] but it may be possible to obtain higher quality results in a clean flake.

Another direction is the development of a higher frequency (GHz) noise measurement setup. This work is currently being pursued in our lab by Zubair Iftikhar. As was alluded to in Chapter 5, the results here are fundamentally different. One particularly simple result is that if $eV, kT < \hbar\omega$ than the noise at frequency ω is significantly suppressed. This has been observed in a low transparency quantum point contact[117]. But finite frequency noise can be significantly more complicated, such as exhibiting photon antibunching when a QPC is tuned such that $\hbar\omega \approx eV$[118]. Such finite frequency noise typically relies on RF matched electronics and commer-

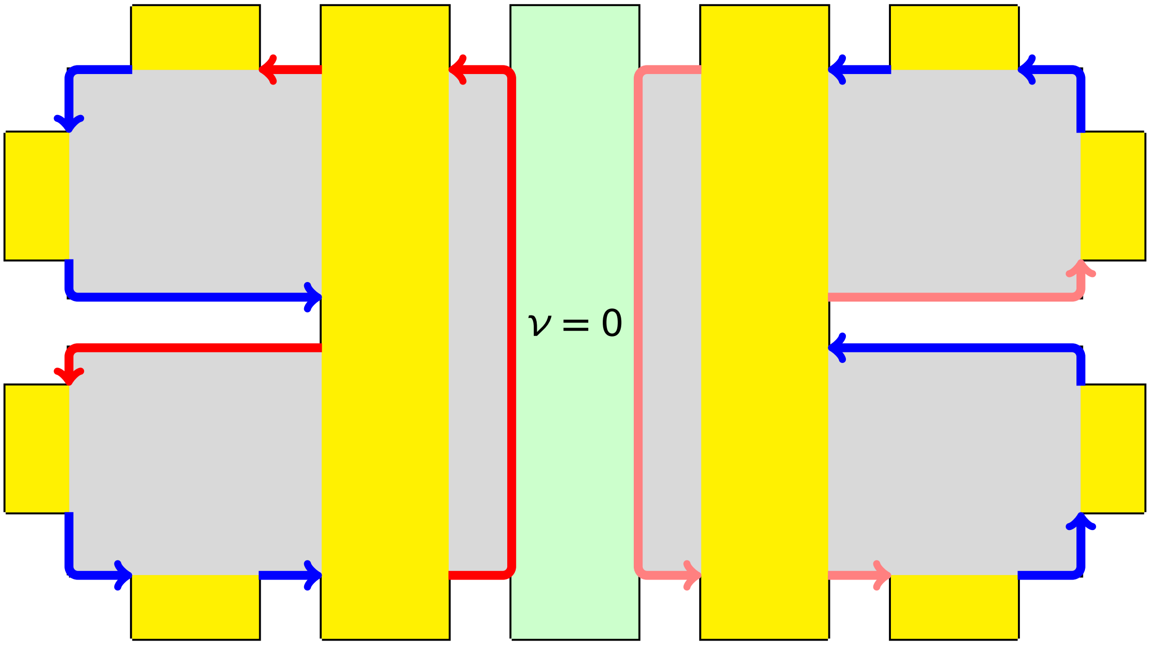

FIGURE 8.1: A sample design for measuring the thermal conductivity of $\nu = 0$ By applying a bias voltage V from the left side of the sample, a voltage $\frac{V}{2}$ is dropped on the floating island. Hot edges then flow out of this island, along the $\nu = 0$ edge induced by a local topgate. Any heat propagation through the $\nu = 0$ is then absorbed by the right side floating contact, which can "partition" the noise and convert the thermal signal into electrical fluctuations.

cially available cryogenic amplifiers.

There are several additional exciting directions, such as the integration of materials and circuit QED techniques, which show great promise[9].

Appendices

Appendix A

Electronics

A.1 High Frequency Probe Wiring for Shapiro steps

RF irradiation measurements were performed in a Leiden Cryogenics probe with 2 semi-rigid brass coaxes reaching down to the mixing chamber anchor and which provide minimal attenuation below 26GHz. A Rhode and Schwarz SMP-02 Generator was used which showed no easily observable harmonics or distortation when tested with a spectrum analyzer. Attenuation was provided by stainless steel cryogenic attenuators from XMA (part number: 4880-5523-xx-CRYO, where xx represents attenuation in dB). Our default setup involved a 20 dB attenuator at the 3K plate anchor and a 20 dB attenuator at the mixing chamber anchor, which was chosen to roughly match the change in temperature and therefore blackbody radiation.

The copper can containing the sample holder is separated from the anchor by approximately 40cm. To cover this distance, we initially used a homemade SMA microcoax which was cut on one side and threaded through a hole in the can, up into the fork where it connected to a pin nested in a block of teflon held next to the chip carrier. The microcoax was chosen for low loss, although it still provided significant frequency dependent attenuation and typically limited our frequency range to below 10 GHz.

Setups of this type generally do not provide any knowledge of the power at the sample, due to unknown attenuation of the lines and antenna coupling to the sample.

Appendix B

Sample Processing

For 2D heterostructure assembly, it is worth noting that over the course of the year it may be required to recalibrate the fabrication procedure, presumably due to fluctuations in the ambient humidity and temperature, but also possibly due to things such as variations in the silicon wafers or polymers used for assembly. What is presented below is a reasonable starting point and generally pretty close to the common procedure, but typically small tweaks to temperatures and lengths of time may be required.

B.1 Stamping

B.1.1 Exfoliation

The goal of exfoliation is to produce large, clean, uniform flakes of a material for assembly in a 2D heterostructure. A small piece of a crystal of the desired material is taken and placed on tape, before being repeatedly ripped apart and transferred onto a substrate to later be assembled into a heterostructure by stamping. This procedure generally involves a few trade offs – exfoliating onto a more adhesive substrate will tend to produce larger usable flakes, but will make picking up such flakes for later stamping harder. The recipe must also be tailored to the materials that are being worked with, as some materials, like graphene and hBN, are easier to exfoliate than others (TMDs, such as NbSe2, generally seem to be harder).

Exfoliation of Graphene and hBN

The recipe used for exfoliation of Graphene and hBN largely follows from ref[119]

1. Clean several (typically 4-6) 5mm by 5mm 280nm SiO2/ Si chips, by lightly sonnicating in DCM for 10 minutes and then plasma ashing for 10 minutes, to improve surface adhesion.

2. While placing substrates on hotplate around 100°C, pull out an ≈6 inch piece of single sided scotch tape and fold the ends a half inch inwards, to form handles. Working over clean chemwipes, place a small amount of material on the tape, and repeatedly sandwich inward and slowly pull apart. When working with graphene, we believe that it is important to avoid overlapping regions of graphene when performing this motion, although evidence for the importance of this is only empirical. When working with hBN, the goal is simply to create a uniform layer of material.

3. Place hot chips SiO2 side down on the tape and then flip tape and chips onto a glass slide. Press tape down on to substrate and push out any bubbles on the chips.

4. Place the glass slide on a 100°C hot plate for 2 minutes, pushing down on the chip every 15 to 30 seconds. After 2 minutes, remove from hot plate and allow to cool down for several minutes, occasionally pushing down on the backside of the chips

5. Once the chip has cooled, very slowly pull the tape off the chips. Chips with hBN can be baked in the tube furnace at 500°C for 3+ hours to remove tape residues. Chips can now be searched to optically find clean flakes

Exfoliation of NbSe2

The above recipe was found to not provide much success with NbSe2. Instead, a recipe was adapted from a post by Jakub Jadwiszczak on research gate

1. Clean chips by sonicating in DCM for 10 minutes. Do not heat chip or plasma ash

2. Exfoliate NbSe2 like before. NbSe2 tends to form thicker layers and must be pulled apart many times in order to create thin flakes

3. Place SiO2 chips on tape and glass slide as before. Rather than heating, use a harder rubber object (typically a Pasteur pipet bulb on the back of a dental tool) and tap and rub on the back of the SiO2 chips for 10 minutes.

4. Extremely slowly pull the tape off the chips (aim for 5-10 minutes per 5 by 5 mm SiO2 chip) Wash chips in DCM to remove residues before quickly searching or transferring flakes to the desecater.

B.1.2 PET Stamping

Conventional PC/ PPC stamping is based on a thin film of a sticky polymer draped over a thicker polymer (typically PDMS) to create a stamp with with which to pickup individual exfoliated flakes. Such stamps are typically not particularly sticky and are time consuming to make. In contrast, one can make use a single layer of the polymer PET to have the same effect. Such stamps are significantly stickier, capable of picking up things with a very high success rate. The stamp is notably much stiffer, which has a few drawbacks associated. The standard procedure is as follows and is particularly indebted to Viviane Costa, upon whose recipe it is based and who provided an incredible amount of assistance

1. Create the stamp. The stamp will be a simple sandwich of glass slide, double sided tape and a square of PET 2-5 cm in side length. The most important details are that the edges are sharp (perpendicular to the square faces rather than sloping) and that the PET is pressed firmly into the double sided tape. If one has precut squares of PET from the machine shop these can be used directly. Otherwise, a razor blade must be used to create sharp edges – in this case, use scissors to cut a PET square that is 5 cm by 5 cm from the PET sheet so that it can be further cut down with a razor. Remove the protective plastic from one side of the PET square by holding the square with one pair of tweezers and delicately attacking the edge near the corner with another pair of sharp metal tweezers. Flip the square over and place the uncovered side down on a piece of double sided tape on a glass slide. The top side should still have protective plastic. Use another glass slide to press down hard on the PET, securing it to the double sided tape. Use the sharp metal tweezers to remove the top protective plastic. If the edges are not already sharp, use a razor blade to sharpen them. The stamp can be inspected under a microscope to see how the edges look.

2. Once the stamp has been made, it must be laminated by taking a clean SiO2 chip and placing it on the stamping station at 60°C. Make the stamp as level as possible with chip. Bring the stamp into contact with the chip. Thermal expansion should allow for a significant fraction of the stamp to make contact with the chip. If this is not the case, slightly increase the heat to aid in thermal expansion and then reduce the temp back down. Some small deformities in the

tape may arise which obscure vision of regions under the stamp – this is normal and all that is required is that one avoids using such regions of the stamp.

3. Flakes are picked up at 60°C, making contact for less the one minute, typically in some part of the corner a fair distance from the edges. The adhesion is very high and typically the stamp will pick up everything it makes contact with. This can be used to ones advantage to make stacks even when the Van der Waals forces don't allow for direct pick up. For instance, while picking up NbSe2 with only contact with hBN proved impossible, direct contact of half of the flake with PET allows for easy pickup.

4. After all flakes of interest have been picked up, bring the stamp and stack into contact with a silicon chip with a grid (plasma ashed for 10 minutes). Don't press too hard, or the stamp will make a mess when it melts. Increase the heat to 130° C and wait for 10 minutes. Very slowly pull the stamp away from the chip, melting the PET. To clean, boil the chip in DCM for several minutes, then an hour at 70° C on the hot plate, then possibly overnight in DCM.

Bibliography

[1] David Vanderbilt. *Berry Phases in Electronic Structure Theory*. Cambridge University Press, Cambridge, England, October 2018.

[2] Markus Konig, Steffen Wiedmann, Christoph Brune, Andreas Roth, Hartmut Buhmann, Laurens W. Molenkamp, Xiao-Liang Qi, and Shou-Cheng Zhang. Quantum spin hall insulator state in HgTe quantum wells. *Science*, 318(5851):766–770, November 2007.

[3] Cui-Zu Chang, Jinsong Zhang, Xiao Feng, Jie Shen, Zuocheng Zhang, Minghua Guo, Kang Li, Yunbo Ou, Pang Wei, Li-Li Wang, Zhong-Qing Ji, Yang Feng, Shuaihua Ji, Xi Chen, Jinfeng Jia, Xi Dai, Zhong Fang, Shou-Cheng Zhang, Ke He, Yayu Wang, Li Lu, Xu-Cun Ma, and Qi-Kun Xue. Experimental observation of the quantum anomalous hall effect in a magnetic topological insulator. *Science*, 340(6129):167–170, April 2013.

[4] Yujun Deng, Yijun Yu, Meng Zhu Shi, Zhongxun Guo, Zihan Xu, Jing Wang, Xian Hui Chen, and Yuanbo Zhang. Quantum anomalous hall effect in intrinsic magnetic topological insulator MnBi 2 te 4. *Science*, 367(6480):895–900, February 2020.

[5] S. Jezouin, F. D. Parmentier, A. Anthore, U. Gennser, A. Cavanna, Y. Jin, and F. Pierre. Quantum limit of heat flow across a single electronic channel. *Science*, 342(6158):601–604, November 2013.

[6] R de Picciotto, M Reznikov, M Heiblum, V Umansky, G Bunin, and D Mahalu. Direct observation of a fractional charge. *Physica B: Condensed Matter*, 249-251:395–400, June 1998.

[7] L. Saminadayar, D. C. Glattli, Y. Jin, and B. Etienne. Observation of the e/3 fractionally charged laughlin quasiparticle. *Physical Review Letters*, 79(13):2526–2529, September 1997.

[8] H. Bartolomei, M. Kumar, R. Bisognin, A. Marguerite, J.-M. Berroir, E. Bocquillon, B. Plaçais, A. Cavanna, Q. Dong, U. Gennser, Y. Jin, and G. Fève. Fractional statistics in anyon collisions. *Science*, 368(6487):173–177, April 2020.

[9] M. Hays, V. Fatemi, D. Bouman, J. Cerrillo, S. Diamond, K. Serniak, T. Connolly, P. Krogstrup, J. Nygård, A. Levy Yeyati, A. Geresdi, and M. H. Devoret. Coherent manipulation of an andreev spin qubit. *Science*, 373(6553):430–433, July 2021.

[10] Lingfei Zhao, Ethan G. Arnault, Alexey Bondarev, Andrew Seredinski, Trevyn F. Q. Larson, Anne W. Draelos, Hengming Li, Kenji Watanabe, Takashi Taniguchi, François Amet, Harold U. Baranger, and Gleb Finkelstein. Interference of chiral andreev edge states. *Nature Physics*, 16(8):862–867, May 2020.

[11] Leon N. Cooper. Bound electron pairs in a degenerate fermi gas. *Phys. Rev.*, 104:1189–1190, Nov 1956.

[12] Jörg Schmalian. Failed Theories Of Superconductivity. *Modern Physics Letters B*, 24(27):2679–2691, October 2010.

[13] F. Bloch. *Zeitschift für Physik*, 52(555), 1928.

[14] L. D. Landau. *Physikalische Zeitschrift der Sowjetunion*, 4(43), 1933.

[15] D. Bohm. *Physical Review*, 75(502), 1949.

[16] Karen Michaeli, Andrew C. Potter, and Patrick A. Lee. Superconducting and ferromagnetic phases in srtio$_3$/laalo$_3$ oxide interface structures: Possibility of finite momentum pairing. *Phys. Rev. Lett.*, 108:117003, Mar 2012.

[17] E. P Wigner. *Physical Review*, 46(1002), 1934.

[18] Michael Tinkham. *Introduction to Superconductivity: v. 1*. Dover Books on Physics. Dover Publications, Mineola, NY, 2 edition, June 2004.

[19] Michael Tinkham. *Introduction to Superconductivity*. Dover, Mineola, New York, 2nd edition, 1996.

[20] P G de Gennes. *Superconductivity of metals and alloys*. Advanced book classics. Westview Press, Philadelphia, PA, March 1999.

[21] N.B. Kopnin. Introduction to the theory of superconductivity, September 2009.

[22] C. Chamon, R. Jackiw, Y. Nishida, S.-Y. Pi, and L. Santos. Quantizing majorana fermions in a superconductor. *Physical Review B*, 81(22), June 2010.

[23] Chetan Nayak, Steven H. Simon, Ady Stern, Michael Freedman, and Sankar Das Sarma. Non-abelian anyons and topological quantum computation. *Reviews of Modern Physics*, 80(3):1083–1159, September 2008.

[24] A. J. Leggett. Majorana fermions in condensed-matter physics. *International Journal of Modern Physics B*, 30(19):1630012, July 2016.

[25] Richard P Feynman and etc. *Lectures on Physics*. Pearson, Upper Saddle River, NJ, January 1963.

[26] C.A. Hamilton, C.J. Burroughs, and S.P. Benz. Josephson voltage standard-a review. *IEEE Transactions on Applied Superconductivity*, 7(2):3756–3761, 1997.

[27] Denis Vasyukov, Yonathan Anahory, Lior Embon, Dorri Halbertal, Jo Cuppens, Lior Neeman, Amit Finkler, Yehonathan Segev, Yuri Myasoedov, Michael L. Rappaport, Martin E. Huber, and Eli Zeldov. A scanning superconducting quantum interference device with single electron spin sensitivity. *Nature Nanotechnology*, 8(9):639–644, September 2013.

[28] P. Krantz, M. Kjaergaard, F. Yan, T. P. Orlando, S. Gustavsson, and W. D. Oliver. A quantum engineers guide to superconducting qubits. *Applied Physics Reviews*, 6(2):021318, June 2019.

[29] A F Andreev. Thermal conductivity of the intermediate state of superconductors. *Zh. Eksperim. i Teor. Fiz.*, Vol: 46, 5 1964.

[30] M. Titov and C. W. J. Beenakker. Josephson effect in ballistic graphene. *Phys. Rev. B*, 74:041401, Jul 2006.

[31] Liang Fu and C. L. Kane. Josephson current and noise at a superconductor/quantum-spin-hall-insulator/superconductor junction. *Phys. Rev. B*, 79:161408, Apr 2009.

[32] J. A. Sauls. Andreev bound states and their signatures. *Philosophical Transactions of the Royal Society A: Mathematical, Physical and Engineering Sciences*, 376(2125):20180140, June 2018.

[33] L. Angers, F. Chiodi, G. Montambaux, M. Ferrier, S. Guéron, H. Bouchiat, and J. C. Cuevas. Proximity dc squids in the long-junction limit. *Phys. Rev. B*, 77:165408, Apr 2008.

[34] H. Courtois, M. Meschke, J. T. Peltonen, and J. P. Pekola. Origin of hysteresis in a proximity josephson junction. *Phys. Rev. Lett.*, 101:067002, Aug 2008.

[35] B. D. Josephson. Coupled superconductors. *Reviews of Modern Physics*, 36(1):216–220, January 1964.

[36] Sidney Shapiro. Josephson currents in superconducting tunneling: The effect of microwaves and other observations. *Physical Review Letters*, 11(2):80–82, July 1963.

[37] R L Kautz. Noise, chaos, and the Josephson voltage standard. *Reports on Progress in Physics*, 59(8):935–992, August 1996.

[38] Clark A Hamilton. Josephson voltage standards. *Review of Scientific Instruments*, 71(3611):3611–3623, 2000.

[39] H.-J. Kwon, V. M. Yakovenko, and K. Sengupta. Fractional ac Josephson effect in unconventional superconductors. *Low Temperature Physics*, 30(7):613–619, July 2004.

[40] Liang Fu and C. L. Kane. Josephson current and noise at a superconductor/quantum-spin-Hall-insulator/superconductor junction. *Physical Review B*, 79(16):161408, April 2009.

[41] Leonid P. Rokhinson, Xinyu Liu, and Jacek K. Furdyna. The fractional a.c. Josephson effect in a semiconductor–superconductor nanowire as a signature of Majorana particles. *Nature Physics*, 8(11):795–799, November 2012.

[42] J. Wiedenmann, E. Bocquillon, R. S. Deacon, S. Hartinger, O. Herrmann, T. M. Klapwijk, L. Maier, C. Ames, C. Brüne, C. Gould, A. Oiwa, K. Ishibashi, S. Tarucha, H. Buhmann, and L. W. Molenkamp. 4π-periodic Josephson supercurrent in HgTe-based topological Josephson junctions. *Nature Communications*, 7(1):1–7, April 2016.

[43] Erwann Bocquillon, Russell S. Deacon, Jonas Wiedenmann, Philipp Leubner, Teunis M. Klapwijk, Christoph Brüne, Koji Ishibashi, Hartmut Buhmann, and Laurens W. Molenkamp. Gapless Andreev bound states in the quantum spin Hall insulator HgTe. *Nature Nanotechnology*, 12(2):137–143, February 2017.

[44] Chuan Li, Jorrit C. de Boer, Bob de Ronde, Shyama V. Ramankutty, Erik van Heumen, Yingkai Huang, Anne de Visser, Alexander A. Golubov, Mark S. Golden, and Alexander Brinkman. 4π-periodic Andreev bound states in a Dirac semimetal. *Nature Materials*, 17(10):875–880, October 2018.

[45] Kévin Le Calvez, Louis Veyrat, Frédéric Gay, Philippe Plaindoux, Clemens B. Winkelmann, Hervé Courtois, and Benjamin Sacépé. Joule overheating poisons the fractional ac Josephson effect in topological Josephson junctions. *Communications Physics*, 2(1):1–9, December 2019.

[46] Hubert B. Heersche, Pablo Jarillo-Herrero, Jeroen B. Oostinga, Lieven M. K. Vandersypen, and Alberto F. Morpurgo. Bipolar supercurrent in graphene. *Nature*, 446(7131):56–59, March 2007.

[47] Katsuyoshi Komatsu, Chuan Li, S. Autier-Laurent, H. Bouchiat, and S. Guéron. Superconducting proximity effect in long superconductor/graphene/superconductor junctions: From specular Andreev reflection at

zero field to the quantum Hall regime. *Physical Review B*, 86(11):115412, September 2012.

[48] Gil-Ho Lee, Sol Kim, Seung-Hoon Jhi, and Hu-Jong Lee. Ultimately short ballistic vertical graphene Josephson junctions. *Nature Communications*, 6(1):6181, May 2015.

[49] S. S. Kalantre, F. Yu, M. T. Wei, K. Watanabe, T. Taniguchi, M. Hernandez-Rivera, F. Amet, and J. R. Williams. Anomalous phase dynamics of driven graphene josephson junctions. *Physical Review Research*, 2:023093, April 2020.

[50] P Joyez and D Vion. The Josephson Effect in Nanoscale Tunnel Junctions. *Journal of Superconductivity*, 12:757–766, December 1999.

[51] V. E. Calado, S. Goswami, G. Nanda, M. Diez, A. R. Akhmerov, K. Watanabe, T. Taniguchi, T. M. Klapwijk, and L. M. K. Vandersypen. Ballistic Josephson junctions in edge-contacted graphene. *Nature Nanotechnology*, 10(9):761–764, September 2015.

[52] A. De Cecco, K. Le Calvez, B. Sacépé, C. B. Winkelmann, and H. Courtois. Interplay between electron overheating and ac Josephson effect. *Physical Review B*, 93(18):180505, May 2016.

[53] T. F. Q. Larson, L. Zhao, E. G. Arnault, M. T. Wei, A. Seredinski, H. Li, K. Watanabe, T. Taniguchi, F. Amet, and G. Finkelstein. Zero-bias crossings and peculiar Shapiro maps in graphene Josephson junctions. *arXiv:2003.08369 [cond-mat, physics:nlin]*, March 2020.

[54] L. Angers, F. Chiodi, G. Montambaux, M. Ferrier, S. Guéron, H. Bouchiat, and J. C. Cuevas. Proximity dc squids in the long-junction limit. *Physical Review B*, 77(16):165408, April 2008.

[55] H. Courtois, M. Meschke, J. T. Peltonen, and J. P. Pekola. Origin of Hysteresis in a Proximity Josephson Junction. *Physical Review Letters*, 101(6):067002, August 2008.

[56] P. Russer. Influence of microwave radiation on current-voltage characteristic of superconducting weak links. *Journal of Applied Physics*, 43(4):2008–2010, April 1972.

[57] Pablo Jarillo-Herrero, Jorden A. van Dam, and Leo P. Kouwenhoven. Quantum supercurrent transistors in carbon nanotubes. *Nature*, 439(7079):953–956, February 2006.

[58] R. E. Thorne, W. G. Lyons, J. W. Lyding, J. R. Tucker, and John Bardeen. Charge-density-wave transport in quasi-one-dimensional conductors. II. ac-dc interference phenomena. *Physical Review B*, 35(12):6360–6372, April 1987.

[59] Yong-Joo Doh, Jinhee Kim, Kyu-Tae Kim, and Hu-Jong Lee. Microwave-induced constant voltage steps in surface junctions of Bi2Sr2CaCu2O8 single crystals. *Physical Review B*, 61(6):R3834–R3837.

[60] Myung-Ho Bae, R. C. Dinsmore III, M. Sahu, Hu-Jong Lee, and A. Bezryadin. Zero-crossing shapiro steps in high-T_c superconducting microstructures tailored by a focused ion beam. *Physical Review B*, 77(14):144501, April 2008.

[61] P. W. Anderson and A. H. Dayem. Radio-frequency effects in superconducting thin film bridges. *Physical Review Letters*, 13(6):195–197, August 1964.

[62] C. D. English, D. R. Hamilton, C. Chialvo, I. C. Moraru, N. Mason, and D. J. Van Harlingen. Observation of nonsinusoidal current-phase relation in graphene Josephson junctions. *Physical Review B*, 94(11):115435, September 2016.

[63] G. Nanda, J. L. Aguilera-Servin, P. Rakyta, A. Kormányos, R. Kleiner, D. Koelle, K. Watanabe, T. Taniguchi, L. M. K. Vandersypen, and S. Goswami. Current-phase relation of ballistic graphene josephson junctions. *Nano Letters*, 17(6):3396–3401, June 2017.

[64] Jian Feng Kong, Leonid Levitov, Dorri Halbertal, and Eli Zeldov. Resonant electron-lattice cooling in graphene. *Physical Review B*, 97(24), June 2018.

[65] Anne W. Draelos, Ming-Tso Wei, Andrew Seredinski, Hengming Li, Yash Mehta, Kenji Watanabe, Takashi Taniguchi, Ivan V. Borzenets, François Amet, and Gleb Finkelstein. Supercurrent flow in multiterminal graphene josephson junctions. *Nano Letters*, 19(2):1039–1043, February 2019.

[66] E. Strambini, S. D'Ambrosio, F. Vischi, F. S. Bergeret, Yu V. Nazarov, and F. Giazotto. The ω-SQUIPT: Phase-engineering of Josephson topological materials. *Nature Nanotechnology*, 11(12):1055–1059, December 2016.

[67] Ivar Martin, Gil Refael, and Bertrand Halperin. Topological Frequency Conversion in Strongly Driven Quantum Systems. *Physical Review X*, 7(4):041008, October 2017.

[68] Lucila Peralta Gavensky, Gonzalo Usaj, D. Feinberg, and C. A. Balseiro. Berry curvature tomography and realization of topological Haldane model in driven three-terminal Josephson junctions. *Physical Review B*, 97(22):220505, June 2018.

[69] Raffael L. Klees, Gianluca Rastelli, Juan Carlos Cuevas, and Wolfgang Belzig. Microwave spectroscopy reveals the quantum geometric tensor of topological Josephson matter. *Physical Review Letters*, 124:197002, May 2020.

[70] Fenner Harper, Rahul Roy, Mark S. Rudner, and S.L. Sondhi. Topology and broken symmetry in Floquet systems. *Annual Review of Condensed Matter Physics*, 11(1):345–368, March 2020.

[71] Peter Hänggi and Fabio Marchesoni. Artificial brownian motors: Controlling transport on the nanoscale. *Rev. Mod. Phys.*, 81:387–442, Mar 2009.

[72] Jukka P. Pekola. Towards quantum thermodynamics in electronic circuits. *Nature Physics*, 11(2):118–123, February 2015.

[73] J. V. Koski, V. F. Maisi, J. P. Pekola, and D. V. Averin. Experimental realization of a Szilard engine with a single electron. *Proceedings of the National Academy of Sciences*, 111(38):13786–13789, September 2014.

[74] Timo Wagner, Peter Talkner, Johannes C. Bayer, Eddy P. Rugeramigabo, Peter Hänggi, and Rolf J. Haug. Quantum stochastic resonance in an a.c.-driven single-electron quantum dot. *Nature Physics*, 15(4):330–334, April 2019.

[75] Clark A Hamilton. Josephson voltage standards. *Review of Scientific Instruments*, 71(3611), 2000.

[76] H. B. Chan and C. Stambaugh. Activation barrier scaling and crossover for noise-induced switching in micromechanical parametric oscillators. *Phys. Rev. Lett.*, 99:060601, Aug 2007.

[77] F. Ricci, R. A. Rica, M. Spasenović, J. Gieseler, L. Rondin, L. Novotny, and R. Quidant. Optically levitated nanoparticle as a model system for stochastic bistable dynamics. *Nature Communications*, 8(1):15141, May 2017.

[78] S. Singh, J. T. Peltonen, I. M. Khaymovich, J. V. Koski, C. Flindt, and J. P. Pekola. Distribution of current fluctuations in a bistable conductor. *Physical Review B*, 94(24):241407, December 2016.

[79] Jakub Spiechowicz and Jerzy Łuczka. Diffusion anomalies in ac-driven brownian ratchets. *Phys. Rev. E*, 91:062104, Jun 2015.

[80] J Spiechowicz, P Talkner, P Hänggi, and J Łuczka. Non-monotonic temperature dependence of chaos-assisted diffusion in driven periodic systems. *New Journal of Physics*, 18(12):123029, dec 2016.

[81] Bernardo Spagnolo, Nikolay Agudov, and Alexander Dubkov. Noise enhanced stability. *Acta Physica Polonica B*, 35, 06 2004.

[82] J. Clarke, A. N. Cleland, M. H. Devoret, D. Esteve, and J. M. Martinis. Quantum mechanics of a macroscopic variable: The phase difference of a josephson junction. *Science*, 239(4843):992–997, February 1988.

[83] David Tong. Lectures on the quantum Hall effect, 2016.

[84] Edward McCann and Mikito Koshino. The electronic properties of bilayer graphene. *Reports on Progress in Physics*, 76(5):056503, April 2013.

[85] Mikhail I. Katsnelson. Graphene: carbon in two dimensions. *Materials Today*, 10(1):20–27, 2007.

[86] V. P. Gusynin and S. G. Sharapov. Unconventional integer quantum Hall effect in graphene. *Phys. Rev. Lett.*, 95:146801, Sep 2005.

[87] A. F. Young, C. R. Dean, L. Wang, H. Ren, P. Cadden-Zimansky, K. Watanabe, T. Taniguchi, J. Hone, K. L. Shepard, and P. Kim. Spin and valley quantum hall ferromagnetism in graphene. *Nature Physics*, 8(7):550–556, May 2012.

[88] Mark Goerbig. Quantum Hall effects, Oct 2009.

[89] L. Wang, I. Meric, P. Y. Huang, Q. Gao, Y. Gao, H. Tran, T. Taniguchi, K. Watanabe, L. M. Campos, D. A. Muller, J. Guo, P. Kim, J. Hone, K. L. Shepard, and C. R. Dean. One-dimensional electrical contact to a two-dimensional material. *Science*, 342(6158):614–617, November 2013.

[90] A. C. C. Drachmann, H. J. Suominen, M. Kjaergaard, B. Shojaei, C. J. Palmstrøm, C. M. Marcus, and F. Nichele. Proximity effect transfer from NbTi into a semiconductor heterostructure via epitaxial aluminum. *Nano Letters*, 17(2):1200–1203, January 2017.

[91] Gil-Ho Lee, Ko-Fan Huang, Dmitri K. Efetov, Di S. Wei, Sean Hart, Takashi Taniguchi, Kenji Watanabe, Amir Yacoby, and Philip Kim. Inducing superconducting correlation in quantum hall edge states. *Nature Physics*, 13(7):693–698, April 2017.

[92] D K C MacDonald. *Noise and Fluctuations*. Dover Books on Physics. Dover Publications, Mineola, NY, June 2006.

[93] Fred MacKintosh. Lecture notes on linear response theory, 2011.

[94] Frank Pobell. *Matter and methods at low temperatures*. Springer, Berlin, Germany, 2 edition, August 1996.

[95] Thierry Martin. Noise in mesoscopic physics, 2005.

[96] X. Jehl, M. Sanquer, R. Calemczuk, and D. Mailly. Detection of doubled shot noise in short normal-metal/ superconductor junctions. *Nature*, 405(6782):50–53, May 2000.

[97] Yoseph Imry. *Introduction to Mesoscopic Physics*. Mesoscopic Physics and Nanotechnology. Oxford University Press, New York, NY, September 1996.

[98] A. McWroter. 1/f noise and germanium surface properties. *Sem.Surf.Phys*, 1957.

[99] Ofir Shein Lumbroso, Lena Simine, Abraham Nitzan, Dvira Segal, and Oren Tal. Electronic noise due to temperature differences in atomic-scale junctions. *Nature*, 562(7726):240–244, October 2018.

[100] E. Sivre, H. Duprez, A. Anthore, A. Aassime, F. D. Parmentier, A. Cavanna, A. Ouerghi, U. Gennser, and F. Pierre. Electronic heat flow and thermal shot noise in quantum circuits. *Nature Communications*, 10(1), December 2019.

[101] M. Büttiker. Scattering theory of current and intensity noise correlations in conductors and wave guides. *Physical Review B*, 46(19):12485–12507, November 1992.

[102] Th. Martin and R. Landauer. Wave-packet approach to noise in multichannel mesoscopic systems. *Phys. Rev. B*, 45:1742–1755, Jan 1992.

[103] Yuan P. Li, D. C. Tsui, J. J. Heremans, J. A. Simmons, and G. W. Weimann. Low-frequency noise in transport through quantum point contacts. *Applied Physics Letters*, 57(8):774–776, August 1990.

[104] S. Washburn, R. J. Haug, K. Y. Lee, and J. M. Hong. Noise from backscattered electrons in the integer and fractional quantized hall effects. *Phys. Rev. B*, 44:3875–3879, Aug 1991.

[105] R. H. Dicke. The measurement of thermal radiation at microwave frequencies. *Review of Scientific Instruments*, 17(7):268–275, July 1946.

[106] M. H. Devoret, D. Esteve, H. Grabert, G.-L. Ingold, H. Pothier, and C. Urbina. Effect of the electromagnetic environment on the coulomb blockade in ultrasmall tunnel junctions. *Phys. Rev. Lett.*, 64:1824–1827, Apr 1990.

[107] Manas Ranjan Sahu, Arup Kumar Paul, Jagannath Sutradhar, K. Watanabe, T. Taniguchi, Vibhor Singh, Subroto Mukerjee, Sumilan Banerjee, and Anindya Das. Quantized conductance with nonzero shot noise as a signature of Andreev edge state. *Phys. Rev. B*, 104:L081404, Aug 2021.

[108] A. V. Feshchenko, O.-P. Saira, J. T. Peltonen, and J. P. Pekola. Thermal conductance of nb thin films at sub-kelvin temperatures. *Scientific Reports*, 7(1), February 2017.

[109] Kazumi Maki. Thermal conductivity of pure type-ii superconductors in high magnetic fields. *Phys. Rev.*, 158:397–399, Jun 1967.

[110] Sergei Sergeenkov and Marcel Ausloos. Thermal conductivity of type-ii superconductors in the mixed state: Electron-vortex scattering. *Phys. Rev. B*, 52:3614–3618, Aug 1995.

[111] N. Kumada, F. D. Parmentier, H. Hibino, D. C. Glattli, and P. Roulleau. Shot noise generated by graphene p–n junctions in the quantum Hall effect regime. *Nature Communications*, 6(1), September 2015.

[112] Maxim Kharitonov. Phase diagram for the $\nu = 0$ quantum Hall state in monolayer graphene. *Phys. Rev. B*, 85:155439, Apr 2012.

[113] Hailong Fu, Ke Huang, Kenji Watanabe, Takashi Taniguchi, and Jun Zhu. Gapless spin wave transport through a quantum canted antiferromagnet. *Phys. Rev. X*, 11:021012, Apr 2021.

[114] Falko Pientka, Jonah Waissman, Philip Kim, and Bertrand I. Halperin. Thermal transport signatures of broken-symmetry phases in graphene. *Phys. Rev. Lett.*, 119:027601, Jul 2017.

[115] T. Yokoi, S. Ma, Y. Kasahara, S. Kasahara, T. Shibauchi, N. Kurita, H. Tanaka, J. Nasu, Y. Motome, C. Hickey, S. Trebst, and Y. Matsuda. Half-integer quantized anomalous thermal Hall effect in the Kitaev material candidate α-RuCl 3. *Science*, 373(6554):568–572, July 2021.

[116] Peter Czajka, Tong Gao, Max Hirschberger, Paula Lampen-Kelley, Arnab Banerjee, Jiaqiang Yan, David G. Mandrus, Stephen E. Nagler, and N. P. Ong. Oscillations of the thermal conductivity in the spin-liquid state of α-RuCl3. *Nature Physics*, 17(8):915–919, May 2021.

[117] E. Zakka-Bajjani, J. Ségala, F. Portier, P. Roche, D. C. Glattli, A. Cavanna, and Y. Jin. Experimental test of the high-frequency quantum shot noise theory in a quantum point contact. *Phys. Rev. Lett.*, 99:236803, Dec 2007.

[118] C. W. J. Beenakker and H. Schomerus. Antibunched photons emitted by a quantum point contact out of equilibrium. *Physical Review Letters*, 93(9), August 2004.

[119] Yuan Huang, Eli Sutter, Norman N. Shi, Jiabao Zheng, Tianzhong Yang, Dirk Englund, Hong-Jun Gao, and Peter Sutter. Reliable exfoliation of large-area high-quality flakes of graphene and other two-dimensional materials. *ACS Nano*, 9(11):10612–10620, September 2015.

Biography

Trevyn Fergus Quillan Larson was born in Durham, North Carolina on May 3, 1994. He grew up in Pittsboro, North Carolina, and attended the University of North Carolina, graduating in 2016 with bachelors degrees in physics and math. He went on to pursue his PhD at Duke University, working in the lab of Professor Gleb Finkelstein.